

DISSERTATION

TARGETING NEUROINFLAMMATION FOR DISEASE MODIFICATION IN MODELS
OF PARKINSONISM

Submitted by

Sean L. Hammond

Graduate Degree Program in Cell and Molecular Biology

In partial fulfillment of the requirements

For the degree of Doctor of Philosophy

Colorado State University

Fort Collins, Colorado

Spring 2018

Doctoral Committee:

Advisor: Ronald Tjalkens

Marie Legare
Gerrit Bouma
Deborah Garrity

Copyright by Sean L. Hammond 2018

All Rights Reserved

ABSTRACT

TARGETING NEUROINFLAMMATION FOR DISEASE MODIFICATION IN MODELS OF PARKINSONISM

Chronic inflammation of the central nervous system (CNS) is a large contributing factor to neurodegeneration. Neuroinflammation is mediated by cellular communication between microglia, astrocytes, neurons and invading leukocytes from the periphery in response to neuronal injury. The second most common neurodegenerative disorder, Parkinson's disease (PD), is characterized by progressive loss of dopaminergic (DA) neurons from the substantia nigra (SN) and sustained neuroinflammatory activation of glial cells in the vicinity of these neurons. One master regulator of glial cell activation is transcription factor, NF- κ B. NF- κ B is ubiquitously expressed throughout the CNS and when activated, positively regulates neuroinflammatory genes in glia and induces prosurvival/synaptic plasticity genes in neurons. Therefore, targeting cell-specific NF- κ B is critical for a desirable outcome when intervening with PD pathology. In the present studies, we utilized several experimental strategies to target neuroinflammation in multiple animal models of parkinsonism. The first utilized an astrocyte-specific NF- κ B knock-out (KO) mouse model. We showed that KO animals were protected from neurotoxin-induced PD pathology and associated behavior, thus supporting the importance of astrocyte- NF- κ B activation in parkinsonism. The second experimental strategy utilized small molecular compound, C-DIM12, which has agonistic properties with

orphan nuclear receptor Nurr1 (NR4A2). Nurr1 activation indirectly suppresses NF- κ B regulated gene expression in glial cells and also positively regulates genes associated with the production/release of DA in neurons. Through counter-regulation of NF- κ B by Nurr1 activation with orally delivered C-DIM12, a neuroprotective effect was conveyed to the SN in a similar experimental mouse model of PD. Lastly, an alternative approach to modulating neuroinflammation utilized adeno-associated viruses (AAVs) to target specific cells of the CNS for transgene expression. Data revealed multiple AAV serotypes differed in transduction capacity and by comparison, an optimal serotype was identified for astrocyte targeting. Using AAV technology, transgene Nurr1 was overexpressed in astrocytes *in vitro* and *in vivo*. The preliminary results with AAV-Nurr1 display a protective effect against neurotoxicity and a promising direction for future studies. In conclusion, these studies investigate the role of neuroinflammation in relation to DA neuronal injury and provide disease modification strategies by cell-specifically targeting NF- κ B and Nurr1 signaling pathways.

TABLE OF CONTENTS

ABSTRACT	ii
CHAPTER 1	
LITERATURE REVIEW	1
1.1 PARKINSON'S DISEASE	1
1.1.1 GENETIC	2
1.1.2 ENVIRONMENTAL	3
1.1.3 AGING	5
1.2 NEUROINFLAMMATION IN PARKINSON' DISEASE	6
1.2.1 MICROGLIA	6
1.2.2 ASTROCYTES	7
1.2.3 NEURONS	9
1.3 CANDIDATE GENES FOR DISEASE MODIFICATION	10
1.3.1 NF- κ B SIGNALING	10
1.3.2 NURR1 SIGNALING	12
1.4 EXPERIMENTAL STRATEGIES FOR GENE TARGETING	13
1.4.1 TRANSGENIC MOUSE MODELS	13
1.4.2 PRE-CLINICAL PHARMACOLOGY	15
1.4.3 VIRAL-MEDIATED GENE THERAPEUTICS	16
CHAPTER 2	
JUVENILE EXPOSURE TO MANGANESE INCREASES NEUROLOGICAL DYSFUNCTION DURING AGING AND IS MEDIATED BY AN ASTROCYTE-SPECIFIC NF- κ B DEPENDENT MECHANISM	19
2.1 INTRODUCTION	19

2.2 MATERIALS AND METHODS	22
2.3 RESULTS	27
2.4 DISCUSSION AND CONCLUSIONS.....	34
2.5 FIGURES	40
 CHAPTER 3	
A NOVEL SYNTHETIC ACTIVATOR OF NURR1 INDUCES DOPAMINERGIC GENE EXPRESSION AND PROTECTS AGAINST 6-HYDROXYDOPAMINE NEUROTOXICITY IN VITRO	48
3.1 INTRODUCTION	48
3.2 MATERIALS AND METHODS	49
3.3 RESULTS	51
3.4 DISCUSSION AND CONCLUSIONS	54
3.4 FIGURES.....	58
 CHAPTER 4	
THE NURR1 LIGAND, 1,1-BIS(3'-INDOLYL)-1-(<i>P</i> -CHLOROPHENYL)METHANE, MODULATES GLIAL REACTIVITY AND IS NEUROPROTECTIVE IN MPTP-INDUCED PARKINSONISM.....	61
4.1 INTRODUCTION	61
4.2 MATERIALS AND METHODS	64
4.3 RESULTS	72
4.4 DISCUSSION AND CONCLUSIONS	80
4.5 FIGURES	87
 CHAPTER 5	
CELLULAR SELECTIVITY OF AAV SEROTYPES FOR GENE DELIVERY IN NEURONS AND ASTROCYTES BY NEONATAL INTRACEREBROVENTRICULAR INJECTION.....	95
5.1 INTRODUCTION.....	95
5.2 MATERIALS AND METHODS.....	98

5.3 RESULTS.....	104
5.4 DISCUSSION	110
5.5 FUTURE DIRECTIONS AND PRELIMINARY DATA	117
5.6 FIGURES	120
CHAPTER 6	
DISCUSSION AND FINAL CONCLUSIONS	129
6.1 FIGURES	132
REFERENCES.....	135

CHAPTER 1

LITERATURE REVIEW

1.1 PARKINSON'S DISEASE

In 1817, Dr. James Parkinson documented the first report of a malady described as 'paralysis agitans' in his monograph entitled: *An Essay on the Shaking Palsy*. The study patients were male, between the ages of 55-72 years old, and each suffering from an analogous manifestation of motor impairment that was easily noticeable while walking down the streets of London. Over time, the malady seemed to progressively worsen and cause a shaking palsy or an uncontrollable resting tremor, which made the disorder distinguishable from other diseases (Parkinson 1817). This disease is now commonly recognized as Parkinson's disease (PD).

Two centuries after the Dr. Parkinson's discovery, the direct etiology of the disease is still unknown. However, research suggests that PD development/progression is heavily affected by genetic predisposition, environmental stimuli and ultimate effects of senescence. Each of these factors cause PD neuropathology in animals and human subjects (Shastry, 2001; Hirsch *et al.*, 2012). The pathology is commonly characterized as progressive degeneration of dopamine (DA) neurons residing in the ventral midbrain area or substantia nigra *pars compacta* (SNpc) and the dorsolateral striatum (ST). Damage to DA neurons cause an imbalance of thalamic-cortical output, resulting in movement symptoms such as bradykinesia, loss of balance and resting tremors. Non-motor symptoms known as depression/anxiety, loss of smell and GI tract issues also

highlight the complexities of PD diagnoses. However, investigating the underlying effects of genetic mutations, neurotoxic exposure, and age could uncover new treatments for PD.

1.1.1 GENETIC

The risk for PD development due to familial history is only 10%, as majority of cases are sporadic (C Klein and Westenberger, 2012). Thus far, a library of eight rare gene mutations are associated with familial PD. These genes have nomenclature PARK1-PARK8, although this classification can be misleading to the true function and effect of the normal gene. Therefore, specific gene names and function of a select few will be described for brevity.

The most common coding variant to cause familial form of PD is mutations of leucine-rich kinase 2 (LRRK2; PARK8). LRRK2 phosphorylation is associated with crucial pathways for neuronal health such as, apoptosis, autophagy and mitochondrial function (A Price *et al.*, 2018). Additionally, recent studies associate LRRK2 mutations with Crohn's disease, which could link enteric nervous system pathology to PD (Hui *et al.*, 2018). Another autosomal-dominant mutation is alpha-synuclein (SNCA; PARK1). Normal SNCA function mediates vesicular protein transport from the endoplasmic reticulum to the Golgi in neurons (AA Cooper *et al.*, 2006). However, SNCA protein is prone to aggregate in the form of fibrils and oligomers which produce neurotoxic intracellular protein inclusions known as Lewy bodies (Zhou *et al.*, 2008). Progressive seeding and spread of Lewy bodies (LB) throughout the CNS is a hallmark of PD pathology (Braak *et al.*, 2004). Mutated form of DJ-1(PARK-7) is an autosomal-recessive mutation associated with early-onset of PD. Basal levels of normal DJ-1 provides anti-

oxidant function by regulating the expression of detoxifying enzyme glutathione (GSH). Interestingly, DJ-1 overexpression can remove toxic alpha-synuclein aggregates from distressed neurons (Zhou *et al.*, 2011). These described genes are just a few examples of how loss of the normal function through hereditary effects can predispose an individual to developing PD later in life. Yet, focusing on only one of these genes for monotherapy is perhaps a wrong direction due to the low percentage of PD patients whom possess these mutations.

1.1.2 ENVIRONMENT

Since the majority of PD patients suffer from sporadic form, environmental exposure is suggested to be a primary cause. The discovery of exposures that increase the risk or produce neurotoxicity have generated enormous breakthroughs in understanding the progression of neurodegeneration. Effects of neurotoxic pesticides, heavy metals, traumatic brain injury (TBI), viral and bacterial infection on DA neurons have been heavily investigated, since these cues can be easily controlled and tested in a laboratory setting.

A valuable PD research tool for approximately thirty-five years is 1-methyl-4-phenyl-1,2,3,6-tetrahydropyridine (MPTP). Dr. William Langston discovered MPTP by treating patients whom intravenously injected the chemical mistaken for synthetic heroin and quickly developed severe forms of parkinsonism (Langston *et al.*, 1983). The metabolite of MPTP, MPP⁺, causes specific degeneration of DA neurons within the SNpc by inhibition of mitochondrial electron transfer at the NADH dehydrogenase-ubiquinone junction (complex I) (Ramsay *et al.*, 1991). Due to the consistency of DA neuronal loss and induction of PD neuropathology, MPTP is a staple model in mice and non-human

primates for pre-clinical drug testing. Other complex I mitochondrial inhibitors used in animal models are pesticides paraquat and rotenone. These chemicals can cause SNCA formation of fibrils, a precursor to LBs, in rodents (Manning-Bog *et al.*, 2002; Sherer *et al.*, 2003) (Uversky *et al.*, 2001).

Studies also identify exposures from various heavy metals, such as copper, iron and manganese (Mn) predispose individuals to acquire PD. Metal ions are necessary for multiple cellular functions and enzymatic processes, however in high levels of exposure, metals are neurotoxic. Elevated levels of copper and iron are associated with multiple neurological disorders (Lan *et al.*, 2016). Specifically, in PD, increased levels of iron are found in degenerating DA neurons of the SNpc (Zhu *et al.*, 2007). Manganese toxicity is also evident in occupational work settings, such as welding or mining (Racette *et al.*, 2017). Severe cases of Mn exposure result in the PD-like disorder, manganism, which manifests neurological symptoms such as dystonia, bradykinesia, rigidity, and depression. Interestingly, manganese crosses the blood brain barrier (BBB) by iron transporter, transferrin, where it accumulates in non-neuronal cells, known as astrocytes (Peres *et al.*, 2016). The specific role of astrocytes in PD and mediating Mn toxicity will be discussed later in the dissertation.

The brain is considered an “immune-privileged” organ due to formation of the BBB, consisting of tight junctions between astrocytes and endothelial cells, which creates a selective passage for peripheral cells to the CNS. However, ongoing research suggests a sophisticated innate immune system persists within the brain, causing neuroinflammation. Neuroinflammation is mediated between the resident immune cells, microglia, astrocytes, neurons and invading leukocytes from the periphery in response to

infectious pathogens. Interestingly, gram-negative bacteria molecules have been found in post-mortem brain tissue from Alzheimer's patients (AD) (Zhan *et al.*, 2016). Endotoxin lipopolysaccharide (LPS) derived from gram-negative bacteria is mainly recognized by toll-like receptor 4 (TLR 4) which is expressed on the surface of glial cells and can induce a cascade of neurotoxic glial activation and neuronal death (Glass *et al.*, 2010). Viral infection is also a potential concern which increases susceptibility to develop PD, as studies show peripheral H1N1 influenza virus infection synergizes neurodegenerative effects of MPTP and increases microglia activation in mice (Sadasivan *et al.*, 2017). Additionally, acute trauma, or TBI acquired by at risk activities such as heavy contact sports is an environmental risk factor for developing PD. Initially, TBI causes mechanical damage of parenchymal cells and blood vessels following a secondary injury resulting in a buildup of oxidative stress and chronic neuroinflammation that damages neurons over time (Impellizzeri *et al.*, 2016; Mettang *et al.*, 2017).

1.1.3 AGING

Since the average age of PD diagnosis is over the age of 60 years old, cellular aging is another primary factor. Studies show over time, mitochondria lose the capacity for necessary adenosine triphosphate (ATP) production which causes large, energy-dependent DA neurons to die. DA neurons are highly energy dependent upon oxidative phosphorylation for ATP production, rather than glycolysis, increasing the demand for functional healthy mitochondria (Surmeier *et al.*, 2017). Additionally, the sheer size of DA neuron arborizations and travel from SNpc to the striatum (ST), require supplemental mitochondrial bioenergetics that only deteriorate with age (Pacelli *et al.*, 2015). Mitochondrial dysfunction also overproduce radical oxidative species (ROS) present in

the microenvironment (Patel, 2016). ROS and reactive nitrogen species (RNS) increase to levels beyond anti-oxidant repair, as result of aging (Dong *et al.*, 2014). DA neurons are especially vulnerable to intracellular oxidative stress due to the formation of DA-quinones during the synthesis of DA. The buildup of DA-quinones is hypothesized to cause downstream signaling to reactive glial cells which further accelerates neurodegeneration (Kuhn *et al.*, 2006).

1.2 NEUROINFLAMMATION IN PARKINSON'S DISEASE

The topic of neuroinflammation has caused speculation over if it could be a preceding cause to DA neuronal death or merely a result of brain injury. However, depending on the context, more recent evidence points to the former, as we further understand the cell specific roles that mediate neuroinflammation. This section will explore the immune functions of microglia, astrocytes, and neurons in relation to PD pathogenesis.

1.2.1 MICROGLIA

Microglia are the resident immune cell of the brain that constantly scan the CNS for invading pathogens. Upon encountering a recognized pathogen, microglia change from a ramified, resting morphology, to an amoeboid shape for phagocytosis of invaders, also known as microglia activation (Glass *et al.*, 2010). Additionally, activated microglia provide neurotropic properties, as phagocytic function is necessary for pruning synapses of neurons for healthy neurotransmission (Schartz, Wyatt-Johnson, LR Price, Colin, and Brewster, 2018b). Therefore, microglia activation could be beneficial or detrimental to the host. Microglia derive from myeloid lineage, which polarize into two unique macrophage subtypes that determine the level of neuroinflammatory response present in the

microenvironment. M1 is a neurotoxic subtype, which express a neuroinflammatory profile of cytokines, chemokines, and ROS. M1 microglia release factors such as, tumor necrosis factor α (TNF α) interleukins, and chemokine ligands (CCL 2 and 3) that communicate with surrounding astrocytes and neurons leading to neurotoxicity (Hirsch and SP Hunot, 2009). M2 is a subtype associated with neurotropism, tissue repair and as previously mentioned, synaptic pruning (Kirkley *et al.*, 2017; Scharz, Wyatt-Johnson, LR Price, Colin, and Brewster, 2018a). Evidence suggests microglia also communicate with peripheral infiltrating T-cells at site of lesion. Major histocompatibility complex (MHC) class II molecules, identified on microglia from MPTP treated mice, have been shown to present endocytosed antigens to CD4⁺ T-cells (Kurkowska-Jastrzebska *et al.*, 1999). Since activated microglia exist as a heterogeneous population, usage of the term “activation” is diverse in context to the ultimate outcome. However, for the purpose of the dissertation, the term will suggest neurotoxic M1 microglia are investigated.

1.2.2 ASTROCYTES

Astrocytes are the most abundant cell type in the mammalian CNS, constituting approximately 30% of all cells. Astrocyte metabolism production of energy and amino acids is crucial for normal neuronal function. Neurons do not produce pyruvate carboxylase, so are dependent on astrocytes for the production of glutamate (Glu) (Sidoryk-Wegrzynowicz and Aschner, 2013). Astrocyte-derived Glu is crucial for neuronal homeostasis and neurotransmitter production for neural signaling. Additionally, neurons rely on astrocytes for normal concentrations of intracellular GSH. GSH activity detoxifies a large number of protein-thiols and ROS to protect the neuron from oxidative damage (Dringen *et al.*, 1999).

Astrocytes also have immune function. As the first line of defense from foreign invaders, astrocytic endfeet (glia limitans) create the BBB, excluding peripheral cells that produce cytokines and ROS (Liddelw and Ben A Barres, 2017). Also, like microglia, astrocytes respond to a multitude of different CNS insults. Astrocytes proliferate to the site of lesioning, noticeable by increased numbers of glial fibrillary acidic protein (GFAP⁺) cells, forming a “glial scar” (Wanner *et al.*, 2013; Hammond 2018). GFAP is the most common marker for measuring gliosis, however, recent transcriptomic analysis revealed new markers for identifying reactive astrocyte phenotypes (Liddelw *et al.*, 2017). Similar to the classification of microglia, a heterogeneous population of activated astrocytes exists. Liddelw *et al.* identified subtypes A1, neurotoxic, or A2, neuroprotective, phenotypes by single-cell transcriptional profiling. Upon ischemic stroke in mice, astrocytes transformed to a A2 reactive phenotype which repaired and protected neurons from further damage. In contrast, LPS injection in mice induced an A1 reactive phenotype, which exacerbated neurotoxicity. These studies suggest complement protein, C3, is an ideal marker for A1 neurotoxic astrocytes (Liddelw *et al.*, 2017). C3 was originally investigated as an essential immune regulator in the peripheral system, by mediating a signal cascade for the formation of membrane attack complexes on the surface of pathogens (Lian *et al.*, 2016). Interestingly, astrocytes also express C3 in response to Interleukin 1, alpha (IL α), TNF α , and complement component subunit 1 q (C1q) which are released from activated microglia (Liddelw *et al.*, 2017). This classical complement pathway between microglia, astrocytes and neurons may be a new candidate mechanism for controlling neuroinflammation (Schartz *et al.* 2018). Studies also show astrocytes communicate with peripheral infiltrating monocytes through a CCL2-CCR2 signaling

mechanism in response to MPTP lesioning in mice (Parillaud *et al.*, 2017). Together, these findings suggest a crucial astrocyte-driven immune-regulatory system exists in neurodegenerative disease.

1.2.3 NEURONS

Neuroinflammation and immunity is controlled by neurons as well. MHC class I molecules are expressed on the surface of neurons to communicate with invading cytotoxic T-cells upon neurotropic viral infection (Chevalier *et al.*, 2011). Neurons express pattern recognition receptor TLR3, which binds viral double-stranded RNA and relays innate immune responses. Other neuronal cell surface receptors, CCLR and C3aR, mediate chemokine and complement protein signaling, respectively, and dictate whether neurons will be engulfed by glia cells or repair itself in response to injury (Parillaud *et al.*, 2017; Scharz *et al.*, 2018). In MPTP mice models, cell surface DA transporters recognize MPP⁺ ions, which downstream induce intracellular oxidative stress and production of nitric oxide (NO). NO reacts with super oxide (O₂⁻) forming peroxynitrite and has high binding affinity to amino acid tyrosine causing nitro-tyrosine adducts and neuronal dysfunction (Moreno, Streifel, *et al.*, 2009). Neurons can also release NO to the extracellular matrix which exacerbates glia activation, resulting in a cyclic loop of neuronal damage (Glass *et al.*, 2010). However, the direct link between oxidative stress and neuroinflammatory reaction is still not fully understood (McElroy *et al.*, 2017). Consequently, by investigating select genes with cell specific transcriptional roles that mediate neuroinflammation in the CNS we can under cover their functions in microglia, astrocytes and neurons.

1.3 CANDIDATE GENES FOR DISEASE MODIFICATION

To date, prescribed PD drugs only treat the symptoms and do not slow the progressive loss of DA neurons. Dopamine replacement therapy, known as levo-dopa (L-DOPA), improve movement deficits. Yet, a side effect of L-DOPA is dyskinesia, due to an overproduction of DA. Transplantation of fetal DA stem cells into the ST is another viable DA replacement. Transplantation has shown to improve motor symptoms, but only to the same degree as L-DOPA administration (Freed *et al.*, 2011). Since these treatments do not slow the progression of PD and patients still worsen over time, new disease modification therapies are necessary. In the following section, two candidate gene pathways highly expressed in the CNS that halt neurodegeneration in animal models will be discussed in detail.

1.3.1 NF- κ B SIGNALING

NF- κ B transcriptional and posttranslational activity is ubiquitously expressed in multiple cell types. There are five mammalian NF- κ B nuclear subunits that homo- or heterodimerize for transcription: p50, p52, p65 (Rel-A), c-Rel, and Rel B (Kaltschmidt *et al.*, 2006). NF- κ B signaling was initially identified as the link between the transcription of immunoglobulin light chain genes in the response to LPS treatment in B-cells (Baltimore, 2009). Currently, studies show NF- κ B activation is upregulated in PD (Hirsch and SP Hunot, 2009), Huntington's disease (HD) (Hsiao *et al.*, 2013), and AD (Kaltschmidt *et al.*, 1997). NF- κ B is the master transcriptional regulator of multiple proinflammatory amplifiers (e.g IL-1 β , TNF α , interleukin-6; IL-6, C3, C1q) in both astrocytes and microglia (Glass *et al.*, 2010; Liddelow and Ben A Barres, 2017). Inflammatory insult, such as LPS treatment on microglia, induces NF- κ B nuclear subunits p65 and p50 to translocate from the

cytoplasm to the nucleus and bind to upstream promotor regions of proinflammatory genes (De Miranda *et al.*, 2015). Proinflammatory cytokines and chemokines released from microglia activate astrocytes which amplify the inflammatory response further back to microglia between glia-glia crosstalk (Kirkley *et al.*, 2017). Augmentation of released inflammatory mediators are recognized by neurons resulting in induction of apoptosis (Hirsch and SP Hunot, 2009). NF- κ B is also a primary regulator of nitric oxide synthase 2 (NOS2), in both astrocytes and microglia. Upon the induction of NOS2, NO and other ROS mediators, are released from glia cells and taken up by DA neurons inducing nitrosative stress, apoptosis or necrosis (Moreno *et al.*, 2011). Interestingly, recent evidence suggests NF- κ B regulates C3 expression primarily in A1, “neurotoxic” astrocytes (Lian *et al.*, 2016).

Despite negative proinflammatory effects regulated by NF- κ B in glial cells under pathological conditions, NF- κ B activation is necessary for synapse formation, neural plasticity, and expression of pro-survival genes in neurons (Lian *et al.*, 2016; Liddelov and Ben A Barres, 2017). Inhibition of NF- κ B in neurons decreases synaptic plasticity, by lack of CREB phosphorylation, resulting in loss of spatial memory in mice (Kaltschmidt *et al.*, 2006). Furthermore, loss of subunit p50 in neurons results in enhanced susceptibility to hippocampal brain injury (Kassed *et al.*, 2002). Taken together these findings, global inhibition of NF- κ B in the CNS may be beneficial for alleviating neuroinflammation regulated by glia cells, except it may be detrimental by suppression of synaptogenesis and regeneration in neurons during PD progression. Therefore, targeting NF- κ B indirectly through counter regulation could lead to a more cell-specific effect in CNS for disease modification.

1.3.2 NURR1 SIGNALING

Nurr1 is predominantly expressed in the ventral midbrain, down regulated in PD patients, and critical for DA neuronal development/homeostasis. High cellular energy demand makes neurons more susceptible to decreased ATP production by mitochondrial failure, which can result from Nurr1-down regulation (Kadkhodaei et al. 2013). There are no known endogenous ligands for Nurr1, but the nature of its interactions with DNA suggests several modes of dimerization with retinoic acid receptors (RXR) to the consensus nerve growth factor binding recognition element (NBRE) (García-Yagüe et al. 2013; Saijo et al. 2009). The NBRE sequences is recognized in promoter regions of the rate-limiting enzyme for DA production, tyrosine hydroxylase (TH), aromatic amino acid decarboxylase (AADC) and transporter proteins: vesicular monoamine transporter 2 (VMAT2) and transmembrane dopamine transporter (DAT) in neurons (Zetterström *et al.*, 1996; Smits et al. 2003; Sakurada et al. 1999). Recently, our group confirmed that upon Nurr1 activation, a dopaminergic phenotype is up regulated by induction of Nurr1 regulated genes, TH and VMAT2 in neurons. Also, we observed Nurr1 activation provides neuroprotection from 6-hydroxydopamine (6-OHDA)-induced neurotoxicity in DA neuronal cultures (Hammond, 2015). Current experimental models using transgenic mice allow for only Nurr1 (+/-) expression, as Nurr1 null mice lack TH expression and die 24 hours after birth, implicative of Nurr1 significance in DA differentiation (Jiang et al. 2005). These studies demonstrate Nurr1 (+/-) DA neurons in mice are more vulnerable to MPTP (Le et al. 1999).

Nurr1 also provides anti-inflammatory effects in glial cells. Constitutive Nurr1 binds to nuclear subunits of NF- κ B at inflammatory promoter sequences, recruiting co-

repressor proteins and histone deacetylase (HDAC) responsible for suppression of neurotoxic gene expression in both microglia and astrocytes. ROS and NOS produced by glial cells are suggested to be under control of the Nurr1-transrepression pathway (Saijo et al. 2009). This transcriptional transrepression through Nurr1 activation results in counter regulation of NF- κ B through an indirect pathway. Additional studies have shown, upon Nurr1 overexpression, there is a decrease of mitochondrial pro-apoptotic factors, such as Bax proteins (Zhang et al. 2009). Targeting the cell specific functions of Nurr1 activation that indirectly inhibits NF- κ B in glia cells and upregulates dopaminergic gene expression in neurons by pharmacologic or gene therapeutics may be a novel approach in halting the progression of PD.

1.4 EXPERIMENTAL STRATEGIES FOR DISEASE MODIFICATION

1.4.1 TRANSGENIC MOUSE MODELS

Current *in vivo* models for genetic modifications in mice include the introduction of plasmid genes *in utero* or neonatal electroporation, intrauterine viral transduction, germ line modifications with Cre-directed to lox-mediated recombination, and recently, CRSPR-Cas9 genome editing with guide RNAs (De Vry et al. 2010; Hashimoto and Mikoshiba 2003; Zong et al. 2005; Nemudryi et al. 2014). Since a murine genome is approximately 97.5% similar to human, mice are desirable models for studying human disease. By increasing normal WT gene expression, inducing expression of a mutant gene, or decreasing WT gene expression, we can further understand the complexities of neurodegeneration. In PD research, transgenic mice can replicate the pathology by toxic gain of function or loss of neuroprotective function. Two examples of toxic gain of function mouse models are the Y39C and A53T mice. Tyrosine-to-cysteine mutant form of human

SNCA protein (Y39C) displayed abnormal SNCA aggregation and motor deficits similar to PD patients (Zhou *et al.*, 2008). Mutated form of human SNCA, alanine-to-threonine mutant (A53T) in mice also developed LB formation similarly seen in PD patients, which resulted in paralysis and death (Giasson *et al.*, 2002). However, loss of DA neurons was not evident in both of these animal models (Giasson *et al.*, 2002; Zhou *et al.*, 2008). Lack of severe PD-like pathology in the midbrain DA neurons could explain a species difference between human and mouse or conceivably SNCA overexpression is not the only cause of DA neurodegeneration. Loss of neuroprotective function in Nurr1 +/- deficient mice can recapitulate PD neurobehavior, have fewer DA neurons in the SNpc, and are more susceptible to MPTP induced neurotoxicity. Although, these mice do not exhibit pathological hallmark of LB formation (Zetterström *et al.*, 1997). In summary, no mouse model is flawless in recapitulating PD pathology, which limits the progress in therapeutic development.

The above mentioned are mouse models heavily focused on neuronal mechanisms. As discussed earlier, non-neuronal cells mediate PD neurotoxicity as well, which requires investigation of cell-specific genetic modifications in mice. One strategy is the Cre-loxP recombination system. Cre-recombinase is a genome-editing enzyme that was originally identified in bacteriophage and targets small palindromic sequences known as loxP sites (Gorman and Bullock 2000). A gene of interest is flanked by the loxP sites on both the 5' and 3' ends of the gene. loxP expressing mice are crossed with chimeric Cre-expressing mice. Through homologous recombination, Cre excises and deletes the gene of interest by targeting the flanking loxP sites. Specific promoters can be inserted 5' of the Cre gene to drive cell specific gene deletion. Interestingly, an astrocyte-specific,

NF- κ B hyperactivated transgenic mouse model was generated by Lian *et al.* 2015. This group crossed hGFAP-Cre and loxP-I κ B α -loxP mice to specifically knock-out I κ B α in GFAP⁺ astrocytes. I κ B α is the protein necessary for sequestering the nuclear subunits of NF- κ B in the cytoplasm. Thereby loss of I κ B α induces translocation of the nuclear subunits, and constitutive activation of NF- κ B in astrocytes. The hyperactivation of astrocyte specific-NF- κ B exacerbated neurodegeneration and further supports the importance of targeting glial-mediated neuroinflammation in PD research (Lian *et al.*, 2015). In contrast, recently in our work, we generated a knock-out mouse that inactivated NF- κ B in astrocytes and will be further explained in chapter 2.

1.4.2 PRE-CLINICAL PHARMACOLOGY

To halt neurodegeneration, a drug must penetrate to the CNS for site of action. Small lipophilic molecular compounds (<400 Da) can cross the BBB by lipid-mediated diffusion (Pardridge, 2012). Upon BBB penetration, the drug should target a specific cell and pathway in PD pathogenesis. Mechanistic properties are tested pre-clinically in animal models and cellular assays. Therefore, the model must closely mimic PD. For instance, the anti-inflammatory drug, minocycline, delivered promising results in a amyotrophic lateral sclerosis (ALS) transgenic mouse model, but worsened ALS patients in a phase III clinical trials. The mouse model tested was later suggested to poorly recapitulate ALS pathology which caused misleading results (Gordon *et al.*, 2007). Additionally, potential drugs must be deemed clinically safe without severe on or off-target toxicity. On target toxicity occurs when interaction between drug and molecular target creates a toxic effect at the dose necessary for the therapeutic result. Changing the disease target may be necessary since the effect is specific to the target and not of the

drug itself. In contrast, off-target toxicity can occur if the drug causes undesirable effects by interacting with an alternative target or region of tissue (Guengerich, 2011). Therefore, altering the derivative or class of compound may be necessary. Drugs that target innate immune function also must not suppress normal immune response which increases susceptibility to sporadic infections (Glass *et al.*, 2010). The need for specificity in targeting neuroinflammation in PD suggests a cell specific delivery system is necessary for controlled pharmacologic response. Interestingly, we have demonstrated that a novel class of compounds, *p*-substituted-diindoylmethane (C-DIM) analogs, have high brain bioavailability, are considered therapeutically safe in mice and canines and can provide anti-inflammatory effects in mouse models of PD (De Miranda *et al.*, 2013; 2014; Hammond 2018; Safety data *unpublished*). Supporting *in vitro* and *in vivo* data are detailed in chapters 3 and 4, respectively.

1.4.3 VIRAL MEDIATED GENE THERAPEUTICS

Gene therapy targeting neurodegeneration is theoretically self-explainable. A gene of interest is delivered into a specific region of the brain that should provide some therapeutic benefit to the neurons affected by the disease. The first step to consider is which vector to use. Genes can be delivered by adenovirus, lentivirus, adeno-associated virus (AAV), and transfection or electroporation of nucleic acids (NA) alone. Each vector has its advantages and flaws. Adenoviruses package a large cloning capacity and transduce neural cells, but lasting expression and cytotoxicity is a concern. Lentiviruses also transduce neural cells and integrate into the host genome. However, safety concerns persist due to the potential of insertional mutagenesis which causes cancer (Hacein-Bey-Abina *et al.*, 2003). Nucleic acids delivered by transfection or electroporation have

endless cloning capacity, except limited on the delivery efficiency and are diluted by cell division. AAVs transduce neural cells and are non-pathogenic in humans and animals, although restrictive concerns are also DNA dilution due to the lack of chromosomal integration (Manfredsson et al. 2016).

Regardless of the limiting factors, AAVs are the most commonly used vector for gene delivery to the CNS. AAVs are small (20nm), contain a single-stranded DNA genome and are a member of the *Parvoviridae* family within the *Dependovirus* genus (Kotterman and Schaffer, 2014) (Daya and Berns, 2008). Several attempts to treat PD patients with AAVs have been made. Safety/feasibility in clinical phases has shown potential gene therapy with AAV2- Glial Derived Neurotrophic Factor (GDNF/neurturin) (Kirik *et al.*, 2000; Bartus *et al.*, 2013). However, results from a phase 2 randomized trial declared there was no significant therapeutic benefit and 3 patients developed tumors (Marks *et al.*, 2010; Merienne *et al.*, 2013). Another failed attempt tested AAV2- aromatic L-amino acid decarboxylase (AADC) in PD patients, but suggested a new trial was needed to confirm efficacy (Mittermeyer *et al.*, 2012). Current clinical trials have predominately only used neurotropic serotype AAV2, which do not target astrocytes. Drinkut *et al.*, confirmed injection of AAV5-hGFAP(2.2 kb) for astrocyte-specific GDNF overexpression in the mouse provided the same neuroprotective efficacy as neuron-derived GDNF, and suggests more AAV based therapies should be targeted towards astrocytes (Drinkut *et al.*, 2012). A large data set that characterizes specific AAVs which transduce astrocytes will be further explored in chapter 6.

In summary, multiple factors contribute to PD pathogenesis that are not well understood and are even less comprehensible when these factors are considered for

combinatorial effects. Therefore, a study that investigates the role of astrocyte-NF- κ B activation as a result of multiple neurotoxic exposures in mice is investigated in the next chapter.

CHAPTER 2

JUVENILE MANGANESE EXPOSURE EXACERBATES NEURODEGENERATION IN A MPTP “TWO-HIT” ANIMAL MODEL AND IS DEPENDENT ON ASTROCYTE-DERIVED NF- κ B ACTIVATION

2.1 INTRODUCTION

Manganese (Mn) is an essential trace element necessary for multiple enzymatic processes in the central nervous system (CNS) that accumulates in astrocytes during overexposure in adults and children. Transport of Mn into astrocytes occurs predominately through divalent metal transporters such as DMT1, ZIP and SLC39A3, where it is a required co-factor for glutamine synthetase (GS), the key enzyme regulating glutamate-glutamine metabolic shuttling between astrocytes and neurons (Erikson and Aschner, 2003; 2006). Mn is also a critical cofactor for superoxide dismutase (Mn-SOD), which protects neurons from the damaging effects of oxidative stress (Zidenberg-Cherr 1983).

However, abnormally high exposure to Mn is neurotoxic. Epidemiological studies correlate elevated levels of Mn in the brain to cognitive and behavioral impairment, to which children appear to be particularly sensitive (Rugless *et al.*, 2014; Takser 2003; He 1994). In more severe cases, Mn exposures from occupational work settings in adults (e.g. mining, welding), can cause classical ‘manganism’ (RODIER, 1955; Wang *et al.*, 1989; Racette *et al.*, 2017). The neurological sequelae of manganism consist of cognitive and motor deficits similar to Parkinson’s disease (PD), including bradykinesia, dystonia, rigidity and depression (RODIER, 1955; Wang *et al.*, 1989; Mergler and Baldwin, 1997;

Racette *et al.*, 2017). Although, patients with manganism do not display severe nigro-striatal dysfunction or resting tremors and are typically non-responsive to levodopa (L-DOPA) therapy (Guilarte *et al.*, 2006;Peres *et al.*, 2016; Racette *et al.*, 2017). These differences are likely due to distinct patterns of neuropathology compared to idiopathic PD, causing toxicity primarily in more glial rich regions, such as the globus pallidus (Gp), subthalamic nuclei(Sth) and substantia nigra *pars reticulata* (SNpr) (Guilarte *et al.*, 2006; Peres *et al.*, 2016). Whereas PD is characterized by preferential loss of dopamine (DA) neurons in the substantia nigra *pars compacta* (SNpc) and long axonal projections to the striatum (ST). Despite these findings, the mechanism by which Mn exposure accelerates PD pathogenesis, is largely undefined.

We previously demonstrated that Mn-induced neurotoxicity results in profound activation of astrocytes and microglia and expression of a large number of neuroinflammatory genes that potentiate neuronal injury (Moreno *et al.*, 2011; Kirkley *et al.*, 2017). Furthermore, we reported that mice pre-exposed to Mn during juvenile development had higher levels of gliosis and neuronal dysfunction than mice exposed to Mn only as adults (Moreno, Yeomans, *et al.*, 2009). These neurotoxic levels of glial activation and neuroinflammation resulting from Mn exposure are heavily controlled by the transcription factor, nuclear factor kappa B (NF- κ B), a master regulator of innate immune responses in lymphoid and myeloid cells, as well as microglia and astrocytes (Glass *et al.*, 2010; Kirkley *et al.*, 2017). *In vitro*, Mn directly activates microglia, which release cytokines and signaling molecules that chronically activate astrocytes through a NF- κ B-dependent mechanism (Kirkley *et al.*, 2017). NF- κ B can be stimulated by numerous intra- and intercellular stressors, including reactive oxygen species (ROS),

inflammatory cytokines and chemokines, as well as Mn accumulation (Moreno *et al.* 2011). NF- κ B has distinct functions within different cell types of the CNS, including regulation of inflammatory gene expression in glia and induction of pro-survival genes in neurons including IAP's, Bcl2, Bcl-XL and survivin. (Glass *et al.*, 2010).

To determine the role of NF- κ B in regulating the neuroinflammatory effects of Mn, we recently developed a novel transgenic model with astrocyte-specific deletion of the NF- κ B signaling pathway (Kirkley 2018). Mice expressing cre-recombinase under control of the human glial fibrillary acidic protein promoter (hGFAP) were crossed with I kappa B kinase 2 (IKK2)-*loxP* mice. Selective deletion of IKK2 in astrocytes provided almost complete protection against loss of DA neurons caused by the neurotoxin, 1-methyl-4-phenyl-1,2,3,6-tetrahydropyridine (MPTP) (Kirkley 2018). The active metabolite of MPTP, MPP⁺, inhibits mitochondrial complex I and causes severe nigrostriatal dysfunction and behavioral deficits in mice similar to those in PD (Jackson-Lewis and Przedborski, 2007). Lack of NF- κ B function in astrocytes also decreased reactive gliosis by suppressing the expression of NOS2 and TNF α , resulting in prevention of MPTP-induced neuronal apoptosis (Kirkley 2018). However, it is unknown whether exposure to Mn can exacerbate the effects of other dopaminergic neurotoxins such as MPTP by modulating glial reactivity and subsequent inflammatory neuronal injury.

In the present study, we postulated that Mn exposure during development would stimulate NF- κ B-dependent intercellular signaling between microglia and astrocytes, resulting in ongoing neuroinflammation that enhances susceptibility to neurological dysfunction during aging. To test this hypothesis, we used a two-hit neurodegenerative model by administering Mn in drinking water to hGFAP-cre^{+/+}/IKK2^{fl/fl} (KO) or hGFAP-cre⁻

$^{-}/IKK2^{fl/fl}$ (WT) mice during juvenile development, followed by exposure to MPTPp (MPTP + probenecid) four-five months later during adulthood. Neurobehavioral analysis was conducted during the two-week MPTPp dosing regimen to detect locomotor deficits associated with injury to the basal ganglia. Brain tissue from multiple regions was collected for determination of Mn, catecholamines, stereological assessment of neuronal numbers, glial activation and expression of proteins regulating DA function. In addition, we identified high levels of the complement protein, C3, in activated astrocytes that was dramatically reduced in KO mice. We also detected a similar pattern of glial activation and C3 expression in human brain tissue from individuals highly exposed to Mn in an occupational setting. These studies indicate that early exposure to Mn exacerbates glial activation and neuronal loss following challenge with a second dopaminergic neurotoxicant through neuroinflammatory activation of NF- κ B in astrocytes.

2.2 MATERIALS AND METHODS

Animals and treatment regimen

All animals were housed on a 12 hr light/dark cycle in a temperature-controlled room (maintained at 22-24°C) and access to standard chow/water *ad libitum*. Procedures were approved by Colorado State University Institutional Animal Care and Use Committee (IACUC) and were conducted in compliance of National Institute of Health guidelines. hGFAP-cre $^{+/-}$ (Cat#: 004600; Jackson Laboratories) mice were backcrossed on a C57/BLJ6 background for twelve generations before crossbreeding with IKK-loxP $^{+/-}$ (acquired from the Karin lab at UC Davis) mice. Four generations of crossbreeding were conducted to acquire hGFAP-cre $^{+/-}/IKK2^{fl/fl}$ (KO) or hGFAP-cre $^{-}/IKK2^{fl/fl}$ (WT) animals for the study. At day P21, mice were administered MnCl $_2$ (50mg/kg/day; Sigma) by

monitoring water intake and weight gain for thirty days following. After P51, mice were placed back on normal drinking water for a period of three-four months for aging and susceptibility to MPTP-HCl solubilized in saline (0.9% NaCl₂) by subcutaneous injection (s.c.; 20mg/kg; MedchemExpress; Monmouth Junction, NJ) and probenecid by intraperitoneal injection (i.p.; 100mg/kg; Sigma) every other day for one week (4 dosages total), per our previously published protocol (Hammond 2018). Treated mice were aged an additional week before tissue collection.

Behavioral analysis

Two weeks before initial behavioral testing, all mice were acclimated to stress handling by methods closely adapted to previously established protocols (Gouveia and Hurst, 2013; Stuart and Robinson, 2015). Open field testing (OFT) was monitored with Versamax System (Omnitech Electronics, Inc; Columbus Ohio) as previously described by Hammond *et al.* 2018 (Hammond 2018). Gait measurements of stride length, rate and paw intensity were detected by our custom-made in house real-time video gait analysis system. Video recordings of mouse gait were conducted as previously reported (Hammond 2018). All behavioral testing was performed before mice were treated on days 0, 7 and 14 (no treatment) of the MPTPp dosing regimen. All parameter values were subtracted from day 0 for change from baseline measurements.

Tissue processing

For immunohistochemical analysis: mice were anaesthetized under deep isoflourane and transcardially perfused with 0.1M phosphate buffered saline (PBS)-cacodylate/heparin (10 U/ml) and 3% paraformaldehyde/PBS. Following decapitation, whole brains were dissected and stored in 3% paraformaldehyde/PBS overnight at 4°C. The next day,

samples were transferred to a gradient of 15-30% sucrose/PBS prior to cryosectioning and storage in cryoprotectant at -20°C until processed for tissue staining. For neurochemical detection of Mn²⁺ and catecholamines: mice were similarly anaesthetized with isoflourane and then rapidly decapitated. Whole brains were dissected and placed on a 1 mm brain block for separation of ST, SN, hypothalamus (Hyp), and cortex (Cx). Specific brain regions were snap frozen in liquid nitrogen and then stored at -80°C until processed for HPLC and ICP-MS. Trunk blood was also collected from decapitated animals and centrifuged at (1,500 rpm at 4°C /15 minutes) for plasma fractionation and transferred to a fresh tube before storage at -80°C.

Western Blotting

ST tissue used for western blotting was homogenized and lysed in RIPA in presence of protease inhibitors. Protein concentrations were determined by BCA protein assay (ThermoScientific, Pierce Rockford, IL). 23ug/well of protein was separated on 12% SDS-PAGE gel and transferred to PVDF membranes. Blots were incubated with Anti-TH (1:1000; Millipore AB152), anti-VMAT2 (1:750; gift from Dr. Gary Miller's Laboratory, Emory University), anti-DARPP32 (1:1000; Millipore AB10518), anti-pDARPP32-Thr34 (1:1000; Millipore AB9206), anti-DARPP32-Thr75 (1:1000; Millipore AB9208), and anti-Beta Actin (1:2000; Sigma A1978) diluted into 5% milk/tris-buffered saline with tween (0.1%) blocking buffer. Secondary antibodies used were: anti-Rabbit (Cell signaling 7076S) or anti-Mouse (Cell Signaling 7074S) diluted in blocking buffer. Chemiluminescent imaging was conducted with on a BioRad ChemiDoc MP and raw TIFF files were analyzed for mean optical band density with ImageJ analysis software (Schneider *et al.*, 2012).

Immunostaining and automated stereological cell counting for fixed mouse brain tissue

For stereological determination of TH⁺ neurons within the SN: the entire SNpc was serially cryosectioned from the subthalamic nucleus (rostral) to the retrorubal field(caudal) regions. Every sixth free-floating section (8 total) was selected from each animal and immunostained for anti-TH (1:500; Millipore AB152) and anti-Neuronal Nuclei (NeuN; 1:250, Millipore; MAB377) by our previously reported protocol (Hammond et al. 2018) (Miller *et al.*, 2011). SNpc neurons were automatically quantitated from 10x-objective montage images of each immunostained section using a Hamamatsu ORCA-Flash4.0 digital CMOS camera, ProScan III stage controller (Prior, Rockland, MA USA) and CellSens Dimension software (version 1.12, Olympus, Center Valley, PA, USA). For automated relative counts of GFAP⁺, IBA-1⁺, NeuN⁺ cells, two sections/animal were selected from the same anatomical regions of SN and ST. Primary antibodies for glia labeling were anti-GFAP (1:500; DAKO Z0334), anti-IBA1 (1:250; WAKO 016-20001) and anti-TH (Abcam 76442) to demarcate the SNpc and SNr nuclei. Region of interest was highlighted based on Allen Brain Atlas for reference, following application of an adaptive threshold with shape factor and area (m^2) object filters for automatic cell detection. Detected cell number was divided over the area (μm^2) of region. The investigator was blinded from all experimental groups during imaging and cell quantitation.

Immunostaining for post-mortem human brain tissue

Formalin-fixed paraffin embedded (FFPE) human brain sections mounted on glass slides were donated by Dr. Brad Racette at Washington University, St. Louis. All section labeling was coded for an unbiased processing/analysis of all experimental groups.

Immunofluorescence processing was conducted as follows: 1) slides were incubated at 55 °C (15 min), 2) cooled to room temperature (15 min), 3) deparaffinization of sections by 2X-xylene (5 min); 2X-100% ethanol (EtOH); 1X-95% EtOH (5 min); 1X- 70% EtOH (5 min); 1X-TBS containing 2% Triton X (5 min), 4) antigen retrieval by submersion in 75% methanol (10 min) and .01M Na Citrate (20 min), 5) blocked sections in 1% donkey and 1% goat serum (1 hr), 6) primary antibodies: anti-GFAP (1:100; DAKO Z0334), anti-IBA1 (1:50; WAKO) and anti-C3 (1:50; Abcam 11871) were diluted in TBS (2% Triton) for 48 hours at 4°C, 7) sections were washed-4X (10 min), secondary anti-Rabbit alexa flour 555-IBA1, anti-Rabbit alexa flour 488-GFAP and anti-mouse alexa flour 555-C3 were diluted in TBS (2% Triton) at 1:200 (2 hr), 8) tissue sections were washed 2X (5min) and 1X (5min) with (2% Triton) containing DAPI, 9) sections were mounted with medium with glass coverslips and stored at 4°C until imaged.

Image analysis of microglia morphology and reactive astrocytes

For detection of microglia morphology, the same sections immunostained for anti-IBA1/TH as mentioned for automated counting were reimaged on a Zeiss Axiovert 200M inverted fluorescent microscope equipped and a Hamamatsu ORCA-ER-cooled charge coupled device camera using a 10x and 40x air objective with Slidebook imaging software (version 5.0, Intelligent Imaging Innovations, Denver CO). Optical fractionator method employed counting frame size (150 X 150 µm) and frame spacing (for SN; 250 X 250 µm, for ST; 550 X 550 µm). 40x z-stack images of IBA⁺ cells from the SNpc, and Gp were acquired and converted to max projection, following a binary transformation and then rendered to a skeletonized image in ImageJ, as previously described in Morrison and Filosa et al. 2013(Schneider *et al.*, 2012; Morrison and Filosa, 2013). To detect C3⁺ and

S100 β ⁺ co-localizing cells, same optical fractionator method was applied for imaging. Cells were manually quantitated per z-stack images. The investigator was blinded from all experimental groups during cell counting.

High-performance liquid chromatography

Samples of striatum were processed for high performance liquid chromatography (HPLC) coupled with electrochemical detection to quantitate levels of DA, 3, 4-dihydroxyphenylacetic acid (DOPAC), homovanillic acid (HVA), serotonin (5-HT) and metabolite 5-hydroxyindoleacetic acid (5-HIAA). The Neurochemistry Core Laboratory at Vanderbilt University's Center for Molecular Neuroscience Research group (Nashville, TN) processed all tissue samples from each experimental group with coded labeling for unbiased analysis.

Statistical Analysis

All data was presented as mean +/- SEM, unless otherwise noted. Experimental values from each mean were analyzed with a Grubb's ($\alpha=0.05$) test for exclusion of significant outliers. Differences between each experimental group were analyzed by a one-way ANOVA following a Tukey *post hoc* multiple comparisons test. Significance was identified as $^{**}P < 0.01$, $^{*}P < 0.05$, $^{**}P < 0.01$, $^{***}P < 0.001$, $^{****}P < 0.0001$. All statistical analysis was conducted using Prism (version 6.0; Graph Pad Software, San Diego, CA).

2.3 RESULTS

Developmental weights and water consumption over MnCl₂ treatment

At post-natal day (PND) 7 mice were tail clipped for DNA purification and identification of KO and WT progeny per our previously published PCR genotyping protocol (Kirkley et al. 2018). At PND 21, mice were placed on a 30-day MnCl₂

(50mg/kg/per day) drinking water regimen during juvenile development following MPTPp-induced parkinsonism as depicted in **Figure 1A**. Based on statistical analysis of MnCl₂ water consumption, WT consumption increased 2.19 ± 0.44 (mL) and KO consumption increased 2.63 ± 0.78 (mL) from 21-51 PND ($n=4-5$; no significance difference between groups) (**Fig 1B**). For accurate dosing of MnCl₂ and detection in change of body weight, mice were weighed every day for the first week of treatment. From 21-27 PND, KO and WT animals significantly increased in weight by 10.65 ± 0.97 and 10.86 ± 0.83 (g), respectively ($n=8$ /group; **** $P < 0.0001$). No significant difference in body weight was detected between groups treated with MnCl₂ (**Fig 1C**).

Inhibited astrocyte-NF- κ B protects DA neurons from MPTP-induced toxicity in the SNpc, but MnCl₂ does not exacerbate neuronal loss

To assess the severity of lesion present in all six experimental groups, SN tissue was serially cryosectioned and systematically immunolabeled with anti-TH (greyscale) for DA neuronal soma (**Fig 2A-F**). Estimated mean of total TH⁺ neurons within the SNpc were quantitated for each experimental animal group as follows: WT no treatment ($8,024 \pm 637.1$), WT with MnCl₂ ($8,779 \pm 777.0$), WT with MPTPp ($3,759 \pm 503.7$), WT with MPTPp/MnCl₂ ($3,867 \pm 222.1$), KO with MPTPp ($7,421 \pm 537.2$), KO with MPTPp/MnCl₂ ($6,957 \pm 1,049$). Both WT with MPTPp and with MPTPp/MnCl₂ displayed a significant ~51-53% loss of TH⁺ neurons compared to control. KO with MPTPp and MPTPp/MnCl₂ endured only a ~7.5-13.3 loss of TH⁺ neurons (**Fig 2G**). For total neuronal nuclei of the SNpc, sections were co-labeled with anti-NeuN. Mean estimate of total neuronal nuclei within the SNpc were quantitated as follows: WT no treatment ($14,034 \pm 631.2$), WT with MnCl₂ ($15,162 \pm 609.8$), WT with MPTPp ($9,778 \pm 379.3$), WT with MPTPp/MnCl₂ ($9,636 \pm$

159.0), KO with MPTPp (12,932 ± 1,167), KO with MPTP/MnCl₂ (11,695 ± 1,152). Comparably, WT with MPTPp and MPTPp/MnCl₂ displayed a significant ~30-31% loss of total neurons compared to control. KO with MPTPp and MPTPp/MnCl₂ only sustained a 7.8-16.7% loss of NeuN⁺ cells which was not significantly different from control (**Fig 2H**) (*n*=6 animals/per group; ***P* < 0.01, ****P* < 0.001).

MnCl₂/MPTPp induces neuronal death in the globus pallidus and striatum by an astrocyte-NF-κB dependent mechanism

In order to evaluate level of neuronal dysfunction in other areas of the brain, anatomically identical cyro-sections of the basal ganglia were selected for quantitation of total NeuN⁺ neurons in the globus pallidus and caudate putamen nuclei. Representative 10x-objective montage images of sections immunolabeled with anti-NeuN (green) shows level of resolution for measurement (**Fig 3A**). The globus pallidus (**Fig 3B**) and caudate putamen (**Fig 3C**) were highlighted as a region of interest (ROI) for accurate detection of total NeuN⁺ per area (μm²), notice blue objects dictate individual cell bodies within the ROI. Based on quantitation of total NeuN⁺/μm², there was an apparent decrease of neurons in WT animals treated with only MPTPp or MnCl₂ but was not statistically different from control. In contrast, WT animals treated with MPTPp/MnCl₂ had a ~44.1% loss of NeuN⁺ neurons within the globus pallidus. In contrast, KO animals with dual treatment were protected from loss of neurons, with no differences in neuronal numbers detected from WT control animals (**Fig 3E**). Quantitation of NeuN⁺ cells/μm² within the caudate-putamen showed a similar trend as the globus pallidus, however no groups were statistically different (**Fig 3F**). To measure integrity of TH⁺ presynaptic terminals of the caudate-putamen, sections were also co-immunolabeled with anti-TH (red) as depicted

in representative image (**Fig 3D**). A decrease in TH intensity was apparent in WT animals treated with MnCl₂ or MPTPp individually but were not significantly different from control. Dual treatment with both MnCl₂ and MPTPp in WT mice increased loss of DA terminals to ~62.5% of control animals, whereas KO animals with dual treatment only had a ~20.7% loss of terminals compared to control WT mice (**Fig 3G**) ($n=6-7$ animals/group; $*P < 0.05$, $**P < 0.01$, $***P < 0.001$). For detection of apoptosis, striatal tissue was collected from WT and KO animals treated with MPTPp and immunoblotted for cleaved caspase-3. Representative blot of three individual experiments shows an intense band detected in WT treated with MPTPp treatment and a suppression of c-caspase 3 protein was evident in KO with MPTPp treatment (**Fig 3H**).

IKK2 knockout mice are protected against behavioral and neurochemical deficits caused by exposure to Mn and MPTPp

Spontaneous locomotor activity was detected by open field test (OFT) for each experimental group. MnCl₂-only treatment seemed to only decrease the total distance traveled, as all other parameters did not change from baseline (**Fig 4A**). Whereas dual treated WT (with MnCl₂/MPTPp) animals displayed hyperactive behavior in multiple parameters of OFT analysis. Dual treatment significantly increased levels of margin time (**Fig 4B**), center time (**Fig 4C**), horizontal movement (**Fig 4E**), stereotypy movement (**Fig 4F**), and ambulatory movement (**Fig 4G**) compared to MPTPp-only treatment. Interestingly, treated KO animals did not display hyperactive behavior and were no different from WT control animal behavior as depicted in representative images of total trace and pseudocolored time plots of activity over a 5 min interval (**Fig 4D**) ($n=7-10$ animals/group; $*P < 0.05$, $**P < 0.01$, $***P < 0.001$, $****P < 0.0001$).

Quantitative analysis of stride length from each experimental animal was conducted using a real-time video gait analysis system. WT animals treated with MPTPp and MnCl₂/MPTPp exhibited an apparent decrease of stride length compared to WT control but was not statistically different. However, dual treated KO animals had a significantly longer stride length compared to treated WT animals during the course of the study (**Fig 4H**) ($n=5-6$ animals/group; $*P < 0.05$). Levels of striatal catecholamines and metabolites were detected with HPLC analysis. All MPTPp treated animals with or without MnCl₂ exhibited a drastic loss of DA and DOPAC. Additionally, a slight increase of DA levels was apparent in MnCl₂-only treated WT animals but was not statistically different from control (**Fig 4I, J**). Dual treated WT animals also displayed a significantly higher ratio of DOPAC/DA compared to control (**Fig 4K**). Assessment of DA metabolite, HVA, also displays MPTPp treatment significantly decreased HVA levels, independent of MnCl₂ treatment and genotype (**Fig 4L**). Serotonin (5H-T) content showed no statistical difference between experimental groups (**Fig 4M**). However, analysis of the serotonin metabolite (5-HIAA) showed a significant increase in both WT and KO dual treated animals compared to MPTPp-only treatment (**Fig 4N**) ($n=5-9$ animals/group; $*P < 0.05$, $**P < 0.01$, $***P < 0.001$).

Dual MnCl₂/MPTPp treatment intensifies microglia activation in the globus pallidus and is suppressed by the intercellular effects of astrocyte NF- κ B inhibition

Relative number of microglia within basal ganglia was detected by immunolabeling with anti-IBA1 (green) as depicted in representative images of the Gp and Cp (**Fig 5A-C**). Both MPTPp and MPTPp/MnCl₂ treatments in WT animals increased number of IBA-1⁺ cells/ μm^2 within the caudate putamen and treated KO animals displayed significantly

less as depicted in **Figure 5D**. Dual treated WT animals also exhibited the most IBA-1⁺ cells/ μm^2 within the globus pallidus and similarly, KO animals had significantly less (**Fig 5E**). There was a significant increase of IBA-1⁺ cells/ μm^2 in the SNpc of MPTPp treated WT animals and slightly fewer in KO animals, but was not statically different from WT (**Fig 5F**) ($n=5-6$ animals/group; $**P < 0.01$, $***P < 0.001$, $****P < 0.0001$). A similar trend of IBA-1⁺ cells/ μm^2 in the SNpr was apparent, although not statically different between groups (**Fig 5F**). For assessment of microglia morphology, 40x-objective IBA-1 (greyscale) images of the Cp and Gp were skeletonized to detect for number of branches as depicted in representative images in **Figure 5H**. WT dual treated animals exhibited significantly less branches/cell in the Cp (**Fig 5I**), Gp (**Fig 5J**), and less junctions/cell in the Cp (**Fig 5K**), and Gp (**Fig 5K**) compared to dual treated KO animals ($n=7$ animals/group; $*P < 0.05$).

Dual MnCl₂/MPTPp-induced astrocyte proliferation is regulated by NF- κ B in the basal ganglia

Expression of IKK2 was determined in hGFAP-cre^{+/-}/IKK2^{fl/fl} mice by co-immunolabeling with anti-GFAP (red) and anti-IKK2 (green), as depicted in representative 100x-objective images from the globus pallidus in WT control (**Fig 6A**), WT dual treated (**Fig 6B**) and KO dual treated (**Fig 6C**) mice. For assessment of the relative number of GFAP⁺ cells present in multiple nuclei of each experimental group, anatomically consistent cyrosections of ST and SN were selected for automated counting of GFAP⁺/ μm^2 . As depicted in representative 10x-objective montage images of the Gp and Cp, dual treated WT animals exhibited an amplified proliferation of GFAP⁺ in both nuclei (**Fig 6F**). Dual treatment significantly increased GFAP⁺/ μm^2 over MPTPp-only treatment

in WT animals in Gp and KO animals exhibited significantly less independent of treatment (**Fig 6 D-G**). Similarly, increased GFAP⁺/μm² was evident in dual treated WT animals in the Cp but was not statistically different from MPTPp-only WT treated animals for this region (**Fig 6H**). Comparably, dual treated WT animals exhibited the most amount of GFAP⁺ immunoreactivity in the SNpc and KO animals significantly suppressed GFAP⁺/μm² to control levels (**Fig 6I-L**). We also observed an apparent trend of GFAP⁺/μm² in the SNpr of each experimental group but was not statistically significant (**Fig 6M**) ($n=6$; $*P < 0.05$, $**P < 0.01$, $***P < 0.001$, $****P < 0.001$).

Complement protein-C3 is highly expressed in reactive astrocytes following treatment with MnCl₂/MPTPp and down regulated in IKK2 KO mice

To quantitate number of neurotoxic astrocytes present, anti- complement protein C3 (red) was utilized for an additional measurement of astrocyte activation in regions of the basal ganglia. Anti-S100β (green) was used to detect total amount of astrocyte cell bodies. By randomized sampling of each nuclei and quantitation of astrocytes co-expressing C3⁺S100β⁺ over total number of S100β⁺ cells, dual MnCl₂/MPTPp treated WT animals exhibited significantly more neurotoxic astrocytes in the Gp (**Fig 7B, D, F**), Cp (**Fig 7B, F, H**), SNpc (**Fig 7J, L, N**), and SNpr (**Fig 7J, N, P**). Inhibition of astrocyte NF-κB with same treatment suppressed the number of C3⁺ present in each region, as depicted in representative images in **Figures 7C, G, K, O** ($n=7$ animals/group; $*P < 0.05$, $**P < 0.01$, $***P < 0.001$). Immunostaining on test human brain tissue shows expression of GFAP (green) and IBA1 (yellow) appear to be specific for glia cells. Anti-C3 (red) was also tested for antibody efficiency, which appears to be primarily only expressed in

peripheral leukocytes as C3⁺ cells only in arterioles of control human tissue (**Fig 8A-C**) (images represent replicates of three sections/antibody).

2.4 DISCUSSION AND CONCLUSIONS

Almost two hundred years ago, James Couper described the first case of manganism from inhalation of Mn oxide ore dusts in workers who developed gait disorders similar to Parkinson's disease (Couper 1837). Today, the pathological mechanisms underlying irreversible neurological damage from Mn exposure are still not completely understood. However, neuroinflammatory activation of glial cells is a common mechanism underpinning the neurotoxicity of Mn in both humans and in animal models of the disease, as we have previously reported (Kirkley et al. 2017; Moreno et al. 2011). Accordingly, we demonstrated that PND 20-34 juvenile mice were particularly susceptible to Mn-induced neuroinflammation (Moreno et al 2009), potentially due to a critical period of striatal development in rodents (Soiza-Reilly and Azcurra, 2009). Recently, we characterized a novel astrocyte-IKK2 transgenic animal that prevented the production of proinflammatory factors NOS2 and TNF α and was neuroprotective in a MPTPp animal model of PD (Kirkley et al. 2018). The present study expanded on this work and elucidated the role of astrocyte activation induced by juvenile Mn intake, which resulted in neuronal loss from the globus pallidus, behavioral abnormalities and drastic differences in glia cell proliferation.

Combined developmental/adult exposure to Mn and MPTPp caused considerably different OFT performance compared to the other experimental groups. Spontaneous locomotor activity was increased in multiple parameters of total distance (**Fig 4A**), margin time (**Fig 4B**), center time (**Fig 4C**), horizontal count (**Fig 4E**), stereotypy count (**Fig 4F**),

and ambulatory count (**Fig 4G**), representing an overall hyperactive phenotype. CNS activity aberrations such as abnormal neuromuscular function and fine motor deficits have been documented in rat models ranging from low (4.8mg/kg) subchronic to high (50mg/kg) chronic MnCl₂ administration (Witholt *et al.*, 2000) (Beaudin *et al.*, 2016). This implies as to which neurotransmitter systems are dysregulated by dual treatment of MnCl₂/MPTPp to the presented hyperactivity. Pre-synaptic DA neurotransmission is not a major system effected since dual MnCl₂/MPTPp treatment did not exacerbate DA neuronal loss in the SNpc (**Fig 2G**) or striatal dopamine production (**Fig 4H**). Or maybe a threshold loss of DA and neuronal bodies was exceeded by MPTPp treatment alone because there was still a significant loss of TH⁺ immunoreactivity in the Cp of dual treated WT animals compared to control and MPTPp-only treatment (**Fig 3G**). Low subchronic dose of MnCl₂ for 5-weeks also demonstrated no further depletion of nigro-striatal DA depletion due to MnCl₂ treatment (Gwiazda *et al.*, 2002). In contrast, Beudin et al. showed chronic administration of 50mg/kg/day from PND 20-460 significantly depleted DA (Beudin *et al.*, 2016). Therefore, if treatment of MnCl₂ was extended longer than 30 days with the same dose (50mg/kg/day) prior to MPTPp treatment, more severe effects could have been observed on DA neurons in the current study.

Thus, we investigated MnCl₂ effects on Gp neurons, which receive and relay primarily inhibitory gamma butyric acid (GABA)-ergic innervation. By quantitation of total neuron marker (NeuN), there was an apparent decrease of NeuN⁺/μm² in both MnCl₂-only and MPTPp-only treated groups. Significant depletion was only detected in dual MnCl₂/MPTPp treated WT animals compared to controls, demonstrative of amplified loss neurons in the Gp (**Fig 3E**). Investigations of Mn-induced neurotransmitter dysregulation

in the Gp are variably dependent on the model and dose regimen. For example, chronic exposure (10 mg/kg) in non-human primates depleted expression of GS in the Gp, but no effect on GABAergic or glutamatergic systems (Burton *et al.*, 2009). Other investigations with rats treated with 6 mg/kg/per day led to significant increase of Mn brain levels and decrease in GABA (Lai *et al.* 1984). Conversely, another study demonstrated that 20 mg/kg/day treatments in rats led to a significant increase of both Mn and GABA concentrations in the brain (Lipe *et al.* 1999).

It is interesting to speculate that the observed hyperactive locomotor responses observed in Mn-treated mice represent loss of neurons in the Gp, which would cause less GABAergic output to the Sth and therefore increased Glu excitation to the SNpc and increased firing of DA neurons to the ST (Erikson and Aschner, 2003). This theory of increased DA firing could explain the modest increases in the number of TH⁺ neurons observed in the SNpc (**Fig 2G**), as well as increases in DA content (**Fig 4G**), TH immunoreactivity in the ST (**data not shown**) and hyperphosphorylation of the post-synaptic DA protein DARPP32 (**data not shown**) in Mn-treated WT animals. Serotonergic neurotransmission is also a possible target of juvenile Mn toxicity. Modulation of monoamine serotonin (5-HT) cause abnormalities in many physiologic functions, such as food intake, motor activity and sleep; which are also symptoms of manganism (Lesch *et al.*, 1996). There was significant increase of the 5-HT metabolite (5-HIAA) of the ST from both dual treated animal groups, but no differences for 5-HT (**Fig 4M**). This is coherent to a previous report where we observed only juvenile mice treated with MnCl₂ exhibited high levels of 5-HIAA compared to adult MnCl₂ treated animals (Moreno, Yeomans, *et al.*, 2009).

Irrespective of which neurotransmitter system is most affected by dual treatment, neuronal death was controlled by neurotoxic astrocyte activation regulated by NF κ B. Inhibition of astrocyte-NF κ B protected DA neurons from both MPTPp and MnCl₂/MPTPp-induced toxicity by ~90% compared to control within the SNpc (**Fig 2G**). KO animals also did not sustain any loss of neurons in the Gp, terminals of the Cp and were protected from apoptotic mechanisms such as activation of cleaved-caspase 3 (**Fig 3E-G**). Prior studies report constitutively active astrocyte-NF κ B increased cytokine production in a MPTP mouse model of PD and increased amyloid burden and gliosis in a mouse model of AD (Oeckl *et al.*, 2012; Lian *et al.*, 2016). Knock-out of IKK2 in all CNS cells demonstrated protection in an auto-immune encephalitis mouse model (van Loo *et al.*, 2006). However, IKK2/NF- κ B signaling in neurons is also necessary for protection against traumatic brain injury and synaptic plasticity for memory formation (Mettang *et al.*, 2017; Kaltschmidt *et al.*, 2006). Therefore, targeting NF- κ B pro-inflammatory function specifically in glia cells may be necessary for a desirable outcome. In the current study, we are the first to report inhibition of astrocyte-IKK2 protected the CNS from gliosis and neuronal death induced by both MnCl₂ and MPTPp treatment.

The astrocyte-specific genotype caused intercellular effects by triggering fewer activated microglia to the Gp (**Fig 5E, J, L**) and Cp (**Fig 5D, I, K**). Inhibition of microglia activation in the Gp of KO animals directly correlated with the preservation of NeuN⁺ cells with dual treatment (**Fig 5E, 3E**). However, no significant suppression was observed in the SNpc or SNr, consistent with the initial characterization of hGFAP-cre^{+/-}/IKK2^{fl/fl} treated with MPTPp (**Fig 5F-G**) (Kirkley 2018). These studies confirmed purified primary astrocytes isolated from KO mice exhibited 70% knockdown of IKK2 which was

consistently observed *in vivo* as depicted in representative images of IKK2/GFAP co-localization in Figure **6A-C**. Quantitation of GFAP⁺/μm² confirmed that the most affected nucleus in WT mice exposed to Mn/MPTPp was the Gp (**Fig 6D, F**). Interestingly, KO animals exhibited significantly less GFAP⁺/μm² in the Gp, Cp, SNpc. Albeit no groups were different in the SNpr, potentially due to high basal levels present in each experimental group prior to treatment (**Fig 6D-M**).

Studies of MPTP neurotoxicity demonstrate that astrocytes remain chronically activated long after activation of microglia subsides subsequent to DA neuronal death (Hirsch and SP Hunot, 2009; Huang *et al.*, 2018). Therefore, we expected that MnCl₂ exposure would prime astrocytes to an activated state which was further enhanced to a neurotoxic state by MPTP administration months later through an NF-κB dependent mechanism. To specifically detect neurotoxic astrocytes expressing a reactive A1 phenotype, we immunolabeled for complement protein-C3 in regions that we saw induction of gliosis and neuronal death (**Fig 7**). C3 has been known for decades as a major convergent factor of the classical complement pathway that mediates a peripheral innate immune response in the presence of pathogens (Ricklin *et al.*, 2016). The expression of C3 in the CNS has more recently been identified in astrocytes from patients with PD, AD, ALS and even HIV infection (Liddelow *et al.*, 2017; Nitkiewicz *et al.*, 2017). Several of these studies demonstrate that astrocyte-C3 expression is regulated through NF-κB (Lian *et al.*, 2016; Nitkiewicz *et al.*, 2017). Lian *et al.* reported that constitutively active NF-κB driven by hGFAP in astrocytes promoted an increase of C3 expression in a mouse model of AD. Inversely, the present study, the KO animals had significantly less C3⁺+S100β⁺/S100β⁺ expressing astrocytes in regions lesioned with dual MnCl₂/MPTPp

treatment compared to the WT animals (**Fig 7D, H, L, P**). These data suggest that astrocyte-NF- κ B regulated C3 expression may be a novel mechanism to attract reactive microglia, maintain a chronically neurotoxic state of astrocytes and drive neurodegeneration at the site of lesion, such as the Gp in this model.

To determine whether glial activation and expression of C3 in astrocytes was a feature of human manganese, we assessed reactive gliosis and C3 expression in post-mortem human brain tissue isolated from South African miners known to be highly exposed to Mn throughout their lifetime. Immunofluorescence staining for anti-GFAP (**Fig 8A**), anti-C3 (**Fig 8B**), and anti-IBA1 (**Fig 8C**) were performed on control human brain tissue to optimize staining efficiency. C3 expression was only expressed in blood cells present in the vessels of brain tissue, which is expected since the antibody was purified against plasma C3 protein (**Fig 8B**). However, we predict to see the bulk of C3 expression shift to GFAP⁺ astrocytes when we analyze/process the Mn exposed brains in the final data set. If the data we analyzed from mouse tissue is translatable to human samples, more C3⁺-GFAP⁺/GFAP⁺ and IBA-1⁺ cells should be evident in Gp, Cp, and SN from the miner brains as compared to control brain tissue (***data not shown***).

In conclusion, we have elucidated a novel neuroinflammatory mechanism associated with juvenile MnCl₂ exposure that exacerbated neurodegeneration from MPTPp treatment during adulthood in a transgenic mouse model. Our results reveal that the Gp is the most affected basal ganglion nuclei by dual treatment and neurodegeneration can be blocked by inhibition of astrocyte-NF- κ B. Additionally, we provide evidence that MnCl₂/MPTPp treatments in mice increase the presence of neurotoxic C3⁺ astrocytes and is highly regulated by astrocyte-NF- κ B activation. Ongoing

research that targets cell-specific NF- κ B in astrocytes could lead to a novel therapeutic approach for PD treatments and PD-like disorders, such as manganism.

2.5 FIGURES

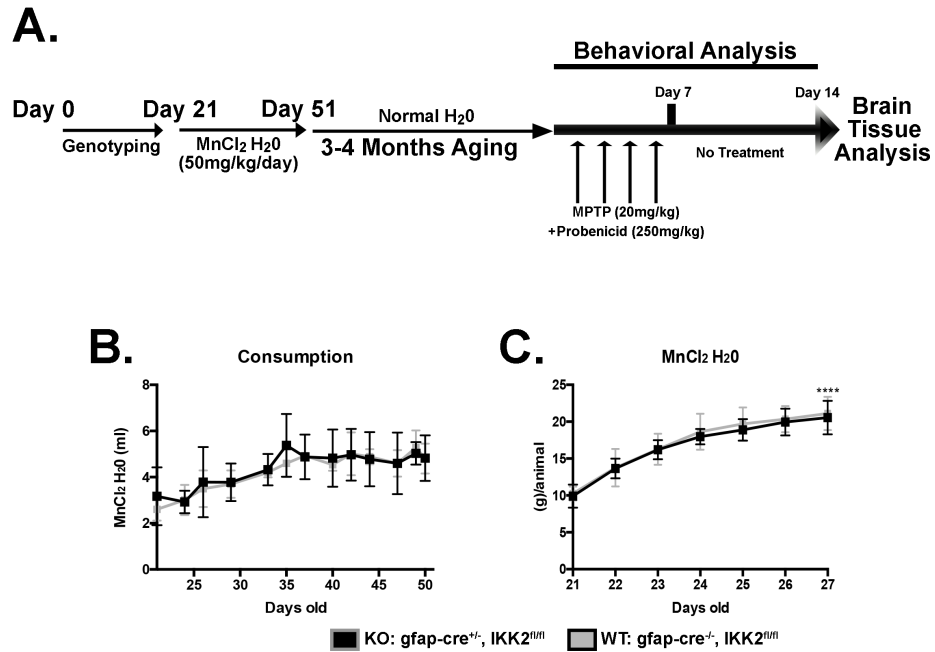


Figure 2.5.1 Two-hit neurodegenerative dosing schematic and monitoring of MnCl₂ intake (A) Depicted dosing schematic applied to both wild-type and knock animals Consumption of water containing MnCl₂ was monitored over the juvenile development period for accurate administration of Mn/50mg/kg/per day (B). Weight measurements were also conducted to monitor significant increases of body mass during juvenile development (C) (*****P* < 0.0001; data represented as *N*=4-5 animals/genotype).

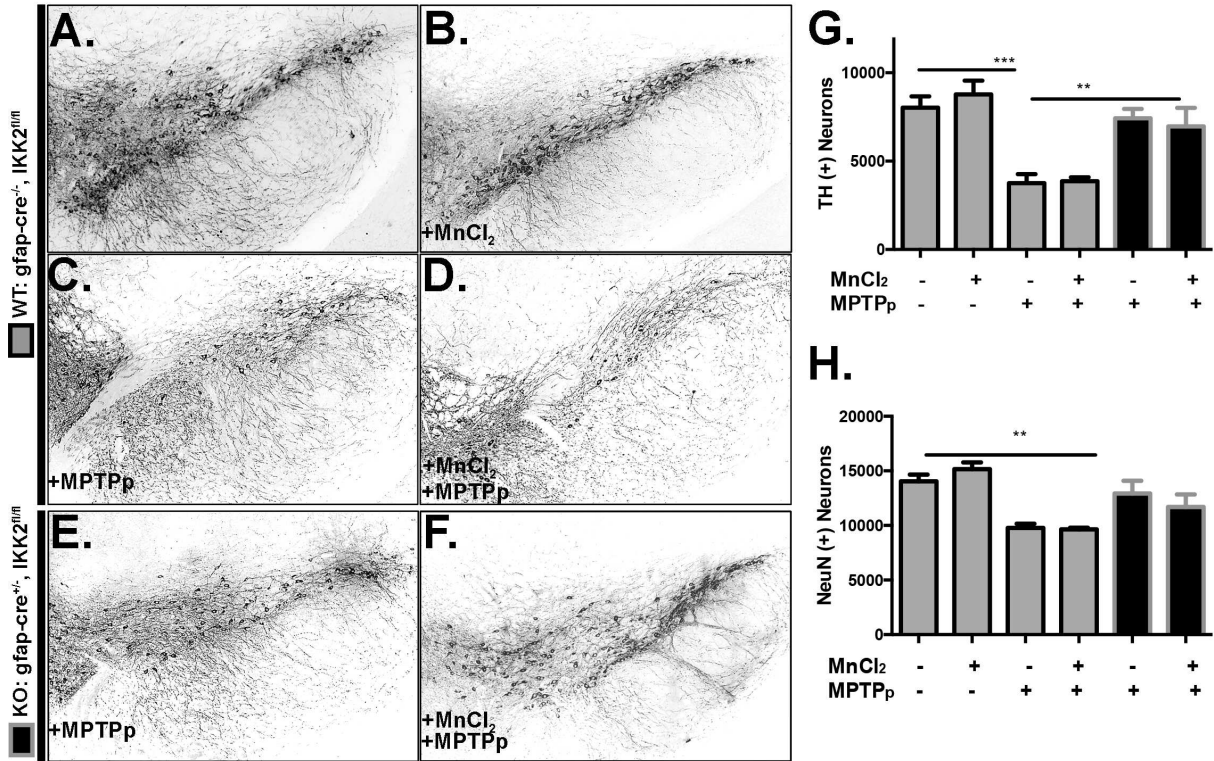


Figure 2.5.2 Stereological cell counting for total DA neurons of SNpc Nigral DA neurons were immunolabeled with anti-TH (black) and imaged for entire SN region as depicted in 10x-objective images of WT control (A), WT + MnCl₂ (B), WT + MPTPp (C), WT + MnCl₂/MPTPp (D), KO + MPTPp (E), KO + MnCl₂/MPTPp (F). (G) Quantitative assessment of TH⁺ neurons in the SNpc. (H) Quantitative assessment of total NeuN⁺ neurons in the SNpc (***P* < 0.01, ****P* < 0.001; *N*=6 animals/group).

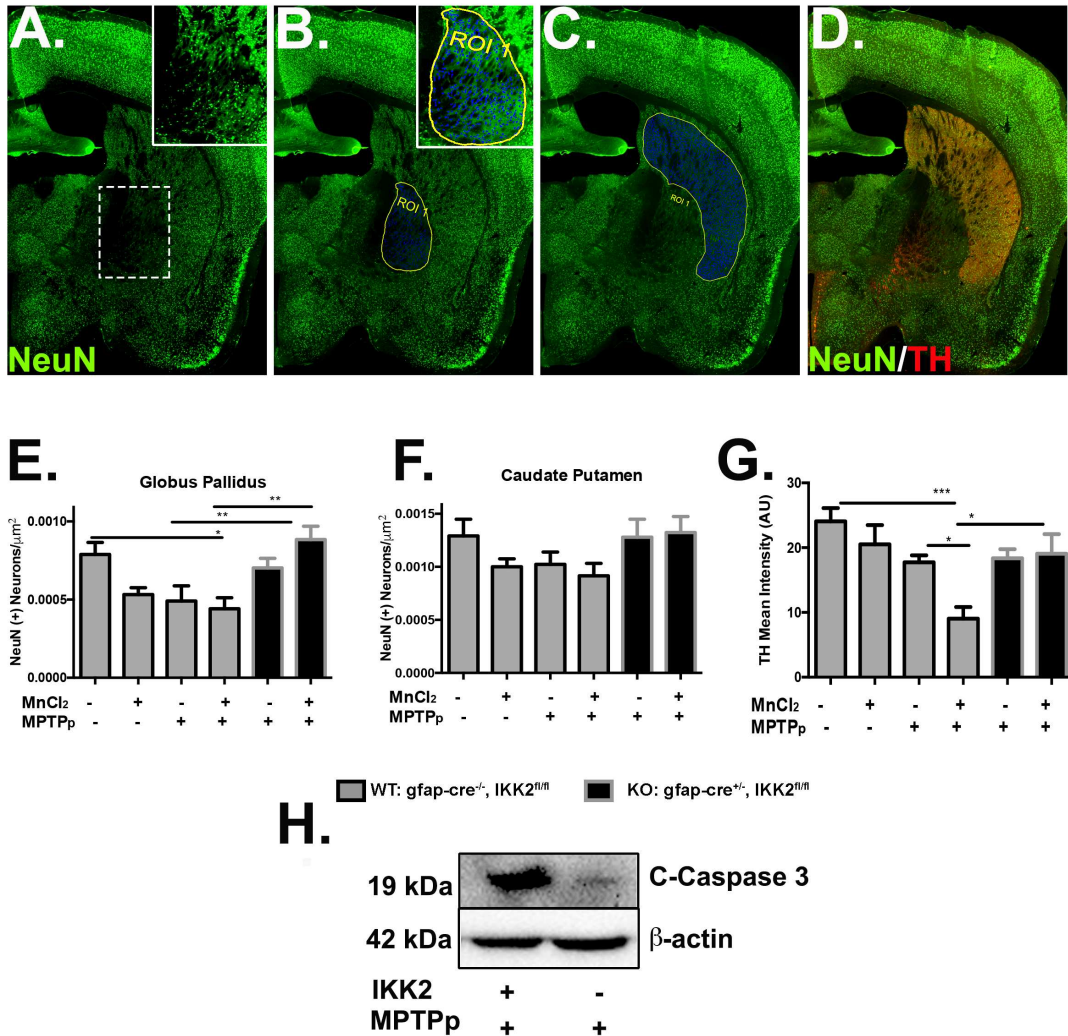


Figure 2.5.3 MnCl₂/MPTPp induces neuronal loss in Gp by astrocyte-NF-kB dependent mechanism (A) Automated total neuronal quantitation of specific brain regions were detected with anti-NeuN (green) immunolabeling as depicted in 10x-objective montage and zoomed in inset of Gp. The Gp (B) and Cp (C) were identified as ROIs for automated cell detection (blue). Co-labeling with anti-TH (red) depicts DA pre-synaptic terminals in the Cp (D). Total NeuN⁺/ μm^2 were quantitated for the Gp (E) and Cp (F). (G) Mean intensity of TH⁺ immunoreactivity was also measured for detection of DA innervation in the Cp (**P* < 0.05, ***P* < 0.01, ****P* < 0.001; *N*=6-7 animals/group). Representative western blot image depicts level of cleaved-caspase 3 protein expression from ST tissue isolated from KO and WT animals treated with MPTPp (blot is a representation of three individual experiments).

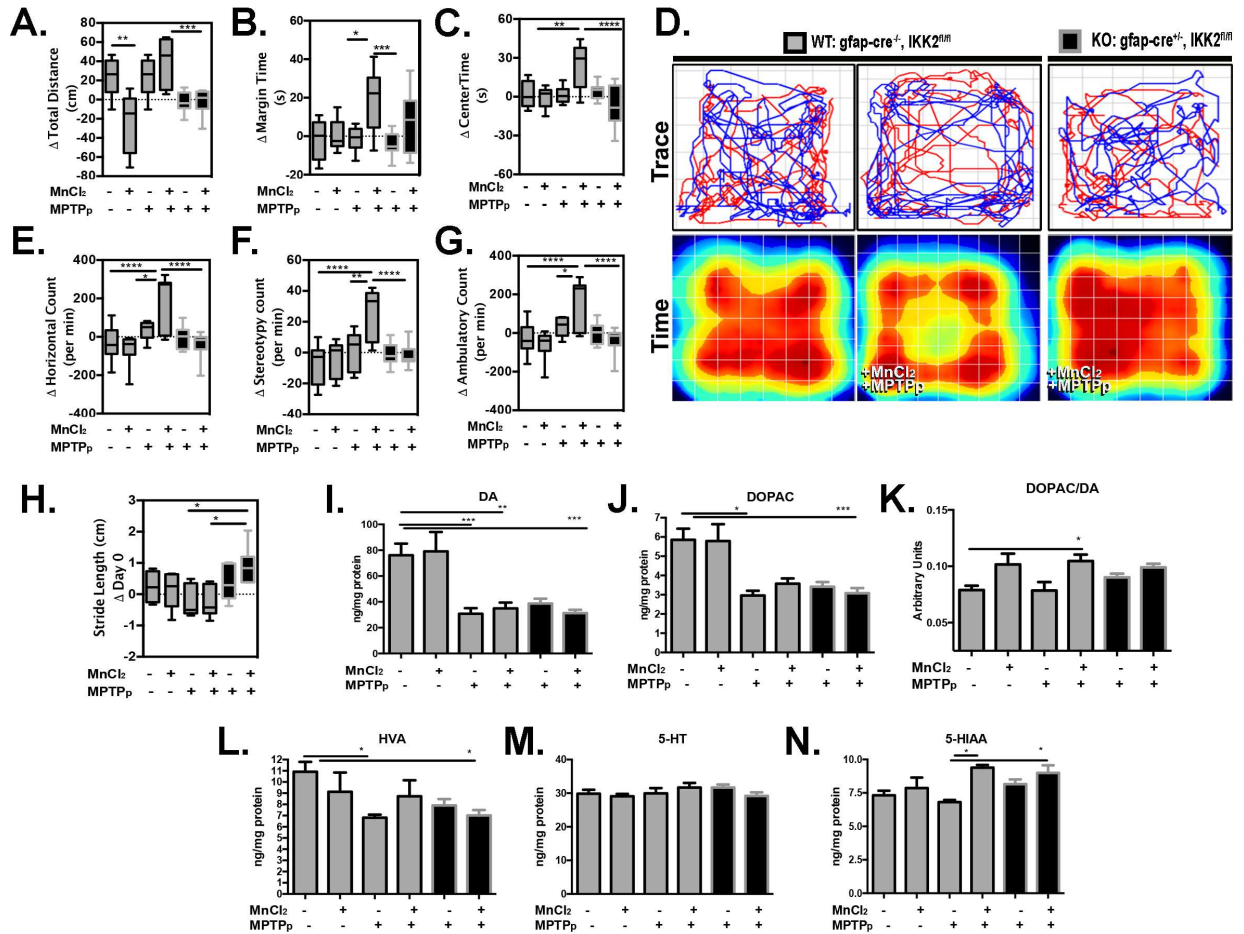


Figure 2.5.4. MnCl₂/MPTPp induces a hyperactive behavioral phenotype dependent on astrocyte-NF- κ B Open field test was conducted to detect for change of total distance (A), margin time (B), and center time (C) compared to day 0. (D) Representative trace plots (top) and pseudocoloring of total time spent (bottom) in position of chamber of 5 min intervals are depicted for WT-control, WT + MnCl₂/MPTPp and KO + MnCl₂/MPTPp treated animals. (E) Change in horizontal count, (F) stereotypy count, and ambulatory count (G) values were also subtracted from day 0 (**P* < 0.05, ***P* < 0.01, ****P* < 0.001, *****P* < 0.0001; *N*=7-10 animals/group). (H) Real-time video gait analysis was utilized to quantitate change of stride length from day 0 (**P* < 0.05; *N*=5-6 animals/group). HPLC analysis for detection of DA (I), metabolite DOPAC (J), DOPAC/DA (K), homovanillic acid (HVA) (L), serotonin (5-HT) (M), and metabolite 5-HIAA were analyzed for neurotransmitter content from ST tissue (**P* < 0.05, ***P* < 0.01, ****P* < 0.001; *N*=5-9 animals/group).

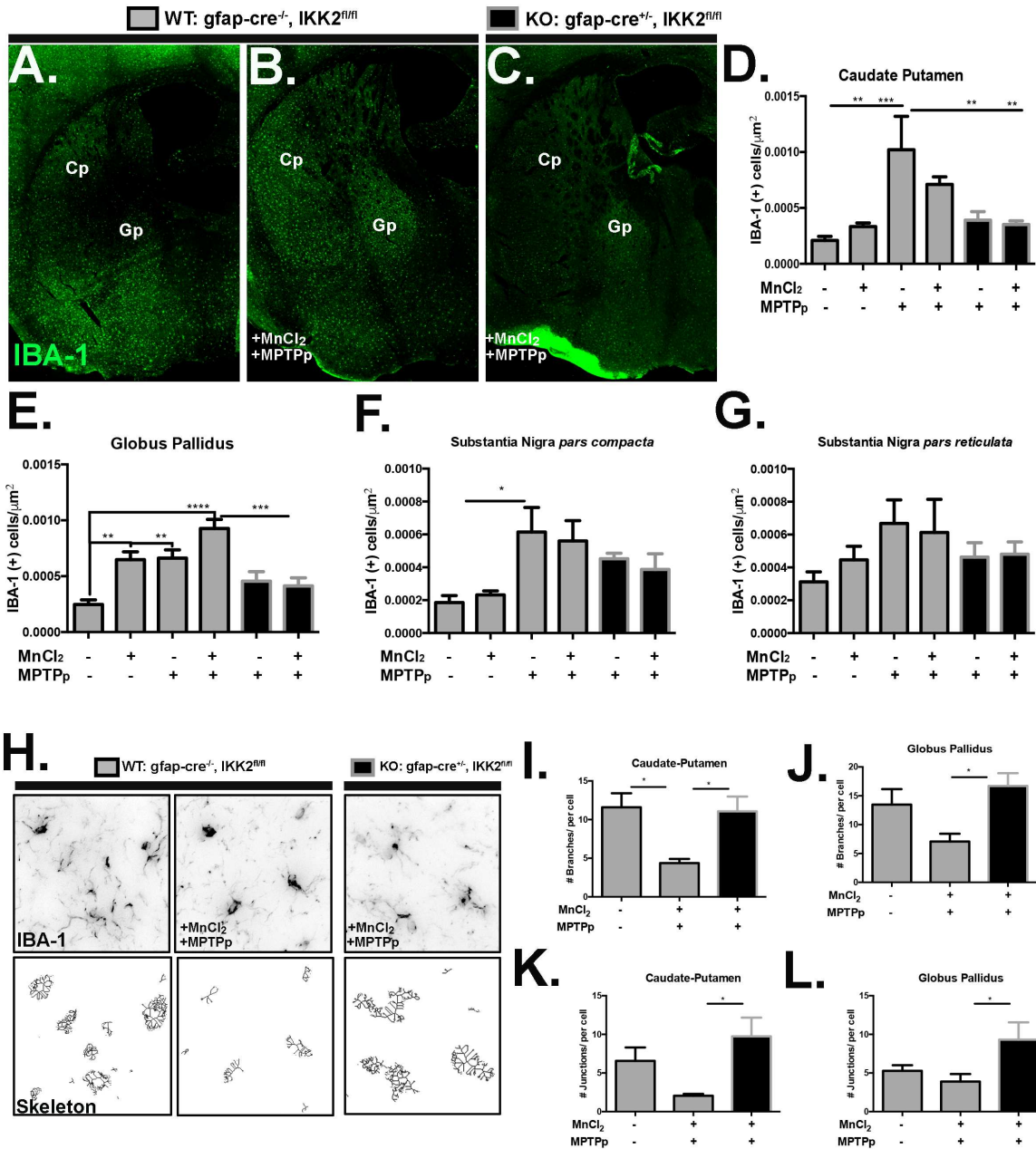


Figure 2.5.5 MnCl₂/MPTPp treatment increases microglia activation and by an astrocyte-NF-κB dependent mechanism Microglia cell bodies were detected by automated quantitation of tissue stained for anti-IBA1 (green) as depicted in 10x-objective images of WT-control (A), WT + MnCl₂/MPTPp (B), and KO + WT + MnCl₂/MPTPp (C) treated animals. Total IBA1⁺/μm² for the Cp (D), Gp (E), SNpc (F), and SNpr (G) were quantitated for all experimental groups (***P* < 0.01, ****P* < 0.001, *****P* < 0.0001; *N*=5-6 animals/group).. (H) Image skeletonization of IBA1⁺(black) cell morphology are depicted in representative images of WT-control, WT + MnCl₂/MPTPp, and KO + WT + MnCl₂/MPTPp. Three experimental groups were quantitated for #branches/cell in Cp/Gp (I-J), and #junctions/cell in Cp/Gp (K-L) (**P* < 0.05; *N*=7 animals/group).

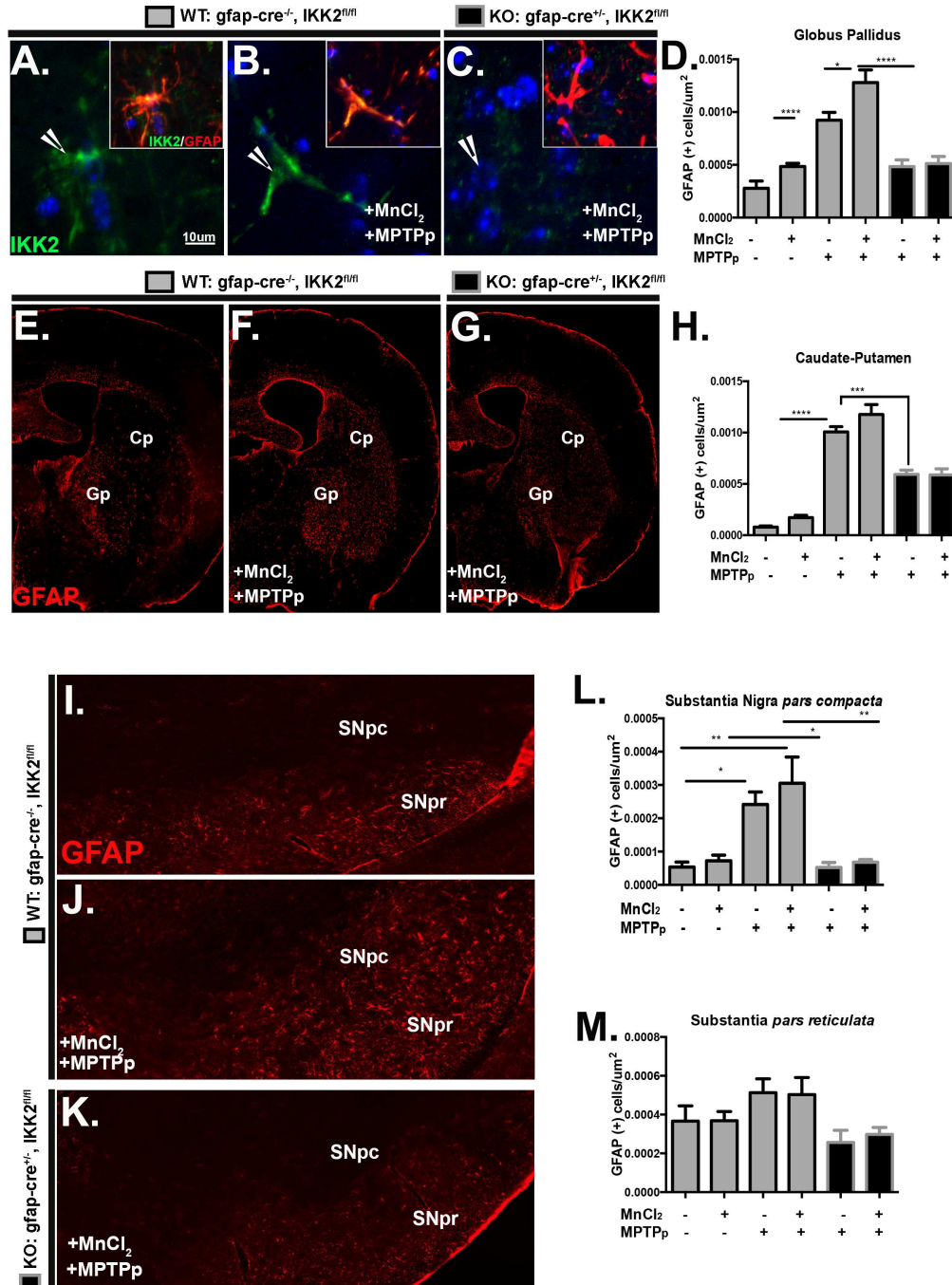


Figure 2.5.6 MnCl₂/MPTPp treatment increases astrocyte activation and by an astrocyte-NF-κB dependent mechanism 100x-objective representative images of anti-*IKK2* (green), anti-*GFAP* (red) colocalizing cells (arrowheads) from WT-control (**A**), WT + MnCl₂/MPTPp (**B**), and KO + MnCl₂/MPTPp (**C**) treated animals. Total GFAP⁺/μm² were quantitated from the Gp (**D**) and Cp (**H**) in all experimental groups, as depicted in 10x-objective montage images of ST with anti-*GFAP* (red) in three groups (**E-G**). SNpc and SNr was also immunostained for *GFAP* as depicted in representative 10x-objective images in (**I-K**). Analysis of GFAP⁺/μm² in SNpc (**L**) and SNpr (**M**) (**P* < 0.05, ***P* < 0.01, ****P* < 0.001, *****P* < 0.001; *N*=6).

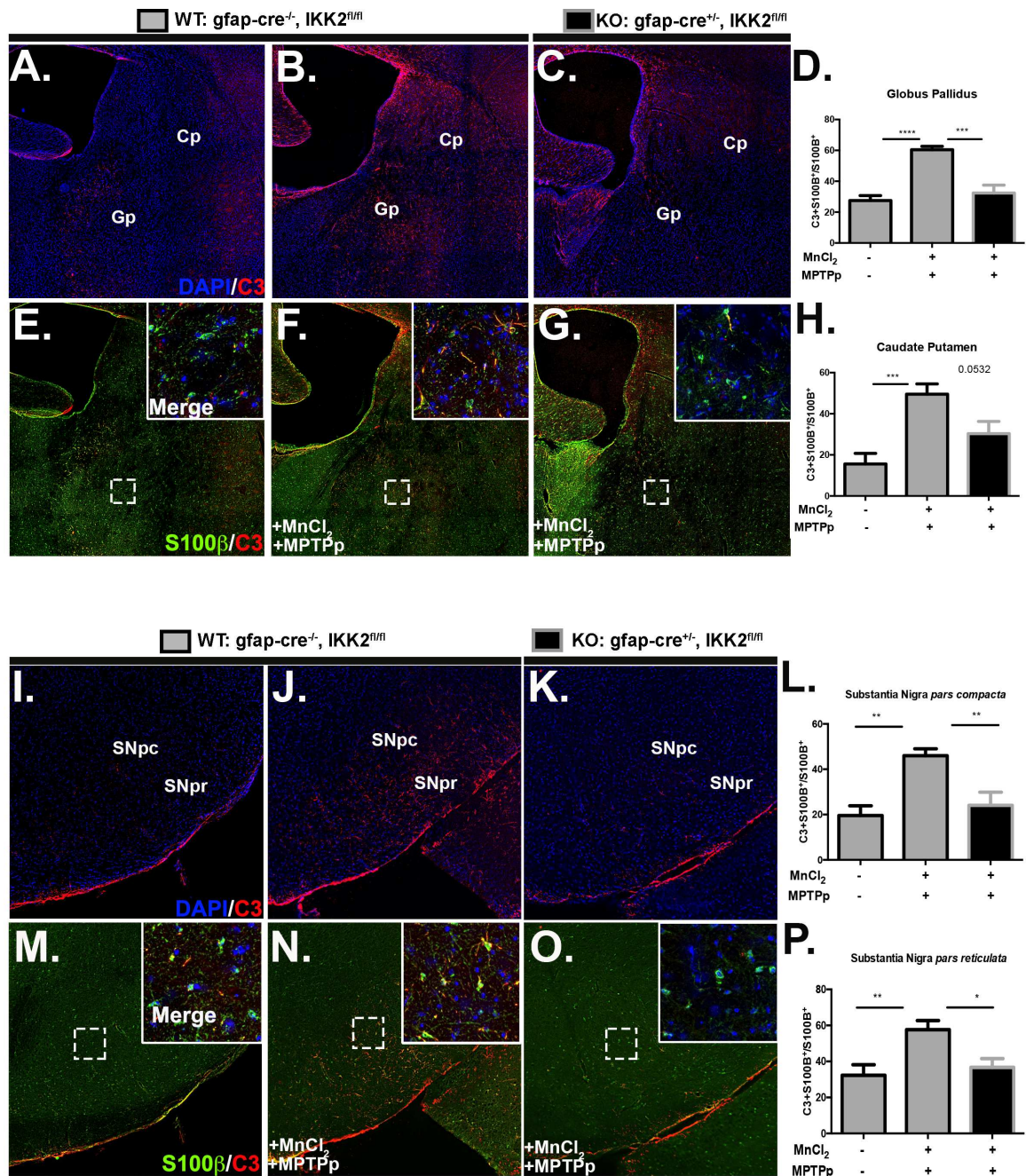


Figure 2.5.7 MnCl₂/MPTPp treatment induces neurotoxic astrocyte-C3 expression and is controlled by NF-κB Representative 10x-objective montage images of Gp/Cp co-immunostained for anti-C3 (red), dapi (blue) and S100β (green) from WT-control (A,E), WT + MnCl₂/MPTPp (B,F), and KO + MnCl₂/MPTPp (C,G) treated animals. Bottom inset displays 20x-magnification of outlined region with merged channels (E-G). Quantitation of C3⁺S100β⁺/S100β⁺ in the Gp (D) and Cp (E), were conducted for three experimental groups. Similarly, SNpc/SNpr 10x-objective images of C3 with dapi (I-K) and S100β with C3 (M-O) and quantitation of C3⁺S100β⁺/S100β⁺ in SNpc (L) and SNpr (P) (**P* < 0.05, ***P* < 0.01, ****P* < 0.001; *N*=7 animals/group).

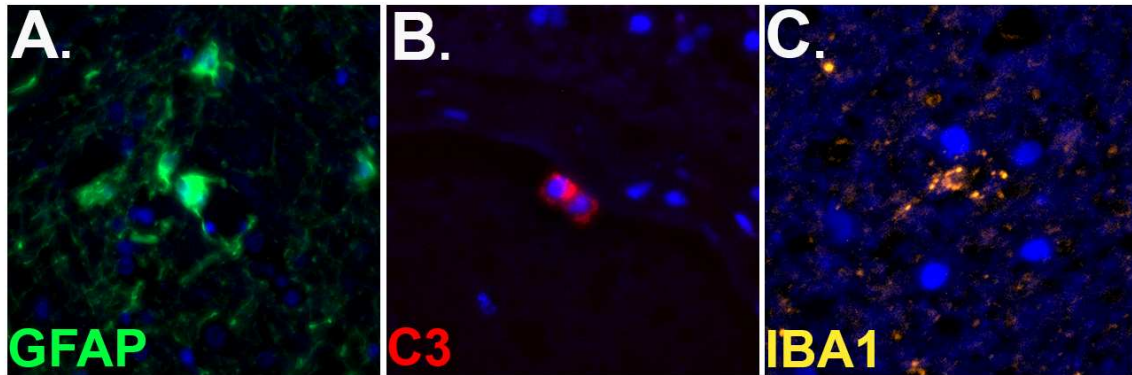


Figure 2.5.8 Preliminary data depicting immunostaining in post-mortem human tissue (A) GFAP (green) in astrocytes, (B) C3 (red) in arteriole walls, and (C) IBA1 (yellow) in microglia (Images representative of three individual experiments).

CHAPTER 3

A NOVEL SYNTHETIC ACTIVATOR OF NURR1 INDUCES DOPAMINERGIC GENE EXPRESSION AND PROTECTS AGAINST 6-HYDROXYDOPAMINE NEUROTOXICITY *IN VITRO*¹

3.1 INTRODUCTION

Parkinson's disease (PD) is the second most common neurodegenerative disorder worldwide. There are no disease-modifying therapies for PD and patients become resistant to current symptomatic treatments as loss of dopaminergic neurons progresses (Shastri, 2001). There is considerable interest in the nuclear receptor, NR4A2 (Nurr1), as a promising target for control of PD progression. Nurr1 is a member of the steroid/thyroid hormone nuclear receptor transcription factor superfamily (Jankovic *et al.*, 2005) and regulates DA metabolism by inducing expression of tyrosine hydroxylase (TH), vesicular monoamine transporter (VMAT2), and aromatic amino acid decarboxylase (AADC) (Kadkhodaei *et al.*, 2009; García-Yagüe *et al.*, 2013). Additionally, Nurr1 is important for development of DA neurons and can inhibit expression of neuroinflammatory genes in glial cells, suggesting a cell-specific context for the transcriptional regulatory effects of the receptor (Zetterström *et al.*, 1997; Saijo *et al.*, 2009). Ablation of Nurr1 in mature DA neurons recapitulates the progressive pathology of PD, with reduced striatal DA, impaired motor behaviors and dystrophic axon/dendrites (Kadkhodaei *et al.*, 2013). The endogenous ligand for Nurr1 is unknown but selected

¹Reprinted with the permission of Neuroscience Letters. All rights reserved.

synthetic lipophilic molecules can enhance the transcriptional activity of Nurr1 *in vitro* (X Li *et al.*, 2012; Smith *et al.*, 2015).

We previously demonstrated that one such molecule, 1,1-bis(3'-indolyl)-1-(*p*-chlorophenyl)methane (C-DIM12), has neuroprotective efficacy in the subacute 1-methyl-4-phenyl-1,2,3,6-tetrahydropyridine (MPTP) model of PD (Inamoto *et al.*, 2008; De Miranda *et al.*, 2014). C-DIM12 activates Nurr1 in pancreatic cancer and keratinocyte epidermal cells (X Li *et al.*, 2012) and also enhances expression of Nurr1 in DA neurons *in vivo*, along with the Nurr1-regulated proteins, tyrosine hydroxylase (TH) and the dopamine transporter (DAT) (De Miranda *et al.*, 2014). In the present study, we investigated the capacity of C-DIM12 to regulate expression of Nurr1 and Nurr1-regulated genes in cultured dopaminergic neuronal cell lines and in primary dopaminergic neurons. We found C-DIM12 induced expression of Nurr1-regulated genes in multiple neuronal cell lines and increased Nurr1 expression in TH expressing primary neurons. RNAi studies show these effects were dependent upon expression of Nurr1. Treatment with C-DIM12 also preserved cell viability following exposure to the neurotoxin, 6-hydroxydopamine (6-OHDA). These findings suggest that C-DIM12 is a direct transcriptional activator of Nurr1 in DA neurons.

3.2 MATERIALS AND METHODS

Cell culture and Reagents

Neuro-2a cells (N2A) and MN9D cells were cultured as previously described (García-Yagüe *et al.*, 2013; W Li *et al.*, 2015). N27 cells were cultured in RPMI1640 medium (Life Technologies, Carlsbad, CA) supplemented with 10% FBS and 1X-PSN. Primary

dopaminergic neurons were isolated at E18 and cultured as previously described (W Li *et al.*, 2015).

Quantitative PCR and transfections

qPCR was performed as previously described (De Miranda, Popichak, Hammond, Jorgensen, *et al.*, 2015) and total RNA was quantified relative to hypoxanthine-guanine phosphoribosyltransferase (N2A) or β -actin (N2A). The sequences of qPCR primers are listed in Supplementary Table 1. Transfections with DsiRNA oligonucleotides or expression plasmids was performed as previously described (De Miranda, Popichak, Hammond, Jorgensen, *et al.*, 2015).

Immunoblotting and immunofluorescence

Immunoblots were performed as described (De Miranda *et al.*, 2014) using the following antibodies: rabbit anti-Nurr1 (1:500; Santa Cruz, Dallas, TX), anti-Rabbit HRP (1:5,000; Cell Signaling), mouse anti-Beta Actin (1:1,000; Sigma, St. Louis, MO) and anti-mouse HRP (1:5,000; Cell Signaling, Danvers, MA). For immunofluorescence staining, N2A cells and primary neurons fixed and stained as previously described (W Li *et al.*, 2015). Primary antibodies used: rabbit polyclonal anti-Nurr1 (1:250; Santa Cruz, Dallas, TX), chicken polyclonal anti-Tyrosine Hydroxylase (1:500; Abcam, Cambridge, MA), rabbit polyclonal anti-Flag (1:500; Sigma F-7425). Secondary antibodies used: Alexafluor647 (1:500; Invitrogen, Carlsbad, CA) and Alexafluor488 (1:500; Invitrogen). All imaging was performed as previously described (De Miranda *et al.*, 2014)

Cell Viability Assays

MN9D and N2A cells were grown on 96-well plates for 24 hrs before treatment with 6-OHDA and C-DIM12. After 24 hrs, cells were imaged using the PrestoBlue Cell viability reagent (Life Technologies, Carlsbad, CA) per the manufacturers protocol.

Statistical Analysis

All data are presented as mean \pm SEM. Analyses of multiple experimental groups was performed using a one-way ANOVA with a Tukey *post hoc* test or Dunnett's multiple comparison test. With two group comparisons, an unpaired t-test Welch's correction and two-sided P-value with 95 % comparison interval was used. Statistical significance is represented by $p < 0.05$ (*), $p < 0.001$ (**), $p < 0.001$ (***), and $p < 0.0001$ (****).

Statistical analyses were performed using Prism software (version 6.0; Graph Pad Software, San Diego, CA).

RESULTS 3.3

Time-dependent expression of Nurr1, TH and VMAT2 was determined in N2A and N27 cells (Figure 1). Treatment with 10 μ M C-DIM12 increased expression of Nurr1 in N2A cells that was maximal at 8 hr (Fig 1A) and remained relatively constant up to 24 hrs, whereas mRNA expression of TH and VMAT2 in N2A cells was maximal at 4 and 8 hr, respectively (Fig 1A). In N27 cells, Nurr1 mRNA level was induced at 8 hr, TH was increased at 8 and 24 hrs and VMAT2 mRNA levels were significantly elevated at 4 hrs (Fig 1B). Dose-dependent expression of Nurr1, TH and VMAT2 was examined in N2A (Fig 1C) and N27 (Fig 1D) cells following treatment with 5 – 10 μ M C-DIM12. Treatment with 10 μ M C-DIM12 increased expression of Nurr1, TH and VMAT2 in N2A cells (Fig

1C), whereas mRNA levels for Nurr1 and VMAT2 were maximally induced by 5 μ M C-DIM12 in N27 cells and TH levels were increased by 10 μ M C-DIM12 in N27 cells (Fig 1D).

To determine whether C-DIM12-induced expression of TH and VMAT2 requires Nurr1, expression of Nurr1 was knocked down using RNA interference with Dicer substrate duplex RNA (DsiRNA) oligonucleotides (Figure 1E-G). Consistent knockdown was observed by immunoblotting in siNurr1-transfected cells compared to siScr-transfected cells (Fig 1E). Cell morphology was unaffected by transfection with RNAi oligonucleotides (Fig 1F), as determined by differential interface contrast (DIC) imaging. In N2A cells transfected with siScr control RNA oligonucleotides, C-DIM12 significantly induced expression of Nurr1 and VMAT2 (Fig 1G). Levels of mRNA for Nurr1, TH and VMAT2 were reduced relative to siScr controls in N2A cells transfected with siNurr1 oligonucleotides. Likewise, Nurr1 RNAi largely abolished the capacity of C-DIM12 to increase expression of Nurr1, TH and VMAT2 in N2A cells. A slight increase in C-DIM12-induced expression of VMAT2 was still observed following Nurr1 RNAi in N2A cells, although the overall level of expression VMAT2 was decreased relative to control cells transfected with scrambled RNAi oligonucleotides (Fig 1G).

To determine the capacity of C-DIM12 to enhance levels of exogenously expressed Nurr1, N2A cells were transfected with a plasmid containing FLAG-tagged full length human Nurr1 or Gal4 control vector and treated with C-DIM12 for 24 hrs (Figure 2 A-D). Expression of FLAG was evident 24 hrs after transfection and was localized to the nucleus of N2A cells (Fig 2A), identical to the pattern of Nurr1 expression (Fig 2B). Treatment with C-DIM12 (10 μ M) increased nuclear fluorescence of FLAG (Fig 2C,

$p < 0.05$) and Nurr1 (Fig 2D, $p < 0.0001$) relative to DMSO (0.1%) treated controls. No expression of FLAG was detected in N2A cells transfected with Gal4 control vector.

The effect of C-DIM12 on expression of Nurr1 in primary dopaminergic neurons was examined in Figure 2, E-G. Neurons were cultured for 1 week until morphologically mature and then treated with C-DIM12 (10 μM) or DMSO (0.1%) vehicle control for 24 hrs. Dopaminergic neurons were identified by expression of TH and Nurr1 expression was determined in TH-positive neurons by immunofluorescence (Figure 2E). C-DIM12 increased expression of both Nurr1 (Fig 2F, $p < 0.001$) and TH (Fig 2G, $p < 0.0001$) compared to control cells treated with DMSO (0.1%, vehicle control).

To examine the neuroprotective effects of C-DIM12 in both functionally mature neurons and undifferentiated neuronal cells, we compared the response of differentiated MN9D dopaminergic neurons cells to that of N2A cells following exposure to 6-hydroxydopamine (6-OHDA) (Figure 3). After five days of differentiation with sodium butyrate, MN9D neurons responded to a depolarizing K^+ stimulus with robust intracellular Ca^{2+} transients (Fig 3A,B). Relative changes in intracellular Ca^{2+} were determined by live cell imaging using Fluo-4-AM and compared to the baseline image prior to stimulation with K^+ (F/F_0). We next exposed N2A and differentiated MN9D cells to increasing concentrations of the neurotoxin, 6-hydroxydopamine (6-OHDA), for 24 hrs and determined viability by measuring cellular reducing potential. Treatment with 0.1 – 100 μM 6-OHDA caused dose-dependent cell death in MN9D and N2A cells, with LD50 values of 100 and 10 μM , respectively (Fig 3C,E). Exposure to 6-OHDA for 24 hrs in the presence of C-DIM12 (10 μM) significantly increased viability in both cell lines ($p < 0.01$, MN9D;

$p < 0.05$, N2A. Fig 3D,F). The protective effect was greater in differentiated MN9D cells than in undifferentiated N2A cells.

3.4 DISCUSSION AND CONCLUSIONS

Nurr1 DNA binding sequences regulate the transcriptional activity of genes necessary for DA production and transport, such as TH, the synaptic dopamine transporter (DAT) and the vesicular monoamine transporter (VMAT2) (Sakurada *et al.*, 1999; Sacchetti *et al.*, 1999). Nurr1 knockout mice fail to develop midbrain dopaminergic neurons and die soon after birth, whereas conditional Nurr1 knock-out mice exhibit deprecations in the nigro-striatal dopamine system and are more susceptible to alpha-synuclein toxicity (Zetterström *et al.*, 1997) (Decressac *et al.*, 2012). Thus, Nurr1 is thought to regulate both the development and maintenance of DA neurons, as well as protecting DA neurons from neurotoxic insults. Interestingly, transcriptional responses to Nurr1 appear to depend both on cell type and on the constitutive level of Nurr1 expression (Johnson *et al.*, 2011). For example, Nurr1 strongly induces TH expression in rodent neural precursor and differentiated cells, but the inductive effects on TH in human neural precursor cells are more modest (Romano *et al.*, 2005) and can even be repressive in human neural stem cells (TE Kim *et al.*, 2013). Such varying transcriptional responses to Nurr1 may depend on the constitutive level of protein expression. In studies that generated a number of neuronal cell lines with graded expression of Nurr1, bioinformatics analysis indicated that many transcripts that were induced at low levels of Nurr1 protein expression were suppressed at high levels of Nurr1 and vice versa (Johnson *et al.*, 2011). Thus, cell- and concentration-specific effects of Nurr1 likely influence the biological outcome in a different cell type.

In the current study, we noticed differences in the pattern of expression of dopaminergic genes between the different neuronal cell lines evaluated, indicated by variance in the time and magnitude of mRNA expression across the time points and concentrations of C-DIM12 evaluated in N2A and N27 cells (Figure 1). C-DIM12 treatment increased expression of Nurr1 and VMAT2 after 8 hrs of treatment in N2A cells, whereas expression of TH maximal at 4hrs, prior to the peak of induction of Nurr1 mRNA (Figure 1A), suggesting that expression of TH and VMAT2 depend on the concentration of Nurr1 or other regulatory factors needed for TH gene transcription. In N27 cells, Nurr1 mRNA levels also were moderately induced by C-DIM12 at 8hrs, whereas VMAT2 mRNA was significantly increased at 4hrs (1B). These temporal patterns in gene induction in response to C-DIM12 could also reflect saturation of Nurr1 binding by the compound. Although differences in mRNA responses were evident between cell lines, C-DIM12-induced expression of the Nurr1-regulated genes TH and VMAT2 was conserved across mouse and rat cells, suggesting a common mechanism of regulation. C-DIM12 directly activates Nurr1, based on transcriptional reporter assays in bladder cancer cells and protein induction studies in epidermal keratinocytes (Inamoto *et al.*, 2008) (Boakye *et al.*, 2013) and we recently reported that C-DIM12 induced Nurr1 nuclear translocation and increased protein expression in dopaminergic neurons in the MPTP/probenecid model of PD (De Miranda *et al.*, 2014). Although Nurr1 appears to lack a classic ligand binding pocket, a separate region of the LBD site is thought to possess ligand binding affinity at the co-activator binding site (Z Wang *et al.*, 2003). Computational modeling and binding studies indicated that other C-DIM compounds bind the co-activator binding site of NR4A1 (Nur77), which is highly homologous to Nurr1 (S-O Lee *et al.*, 2014). Further studies are

now being conducted to investigate whether C-DIM compounds have direct binding affinity for Nurr1 at a similar site in the LBD. To test the hypothesis that C-DIM12 requires Nurr1 to induce expression of dopaminergic genes in neuronal cultures, the expression of Nurr1 was ablated using RNAi in N2A cells (Figure 1E-G). Loss of Nurr1 expression prevented the capacity of C-DIM12 to induce expression of the Nurr1-mediated mechanism (Figure 1E-G), indicating that Nurr1 is required for the transcriptional activation of these genes by C-DIM12. Even in the absence of C-DIM12, expression of VMAT2 and TH significantly decreased in Nurr1 siRNA cells compared to siRNA control cells, indicating direct regulation of these genes by Nurr1 in N2A cells (Figure 1G). Our current findings support the hypothesis that C-DIM12 directly regulates dopaminergic gene expression of TH and VMAT2 in N2A cells through a Nurr1-dependent mechanism. Nurr1 is down-regulated in patients with PD and polymorphisms in Nurr1 increase the risk for a rare familial form of the late onset disease (Liu *et al.*, 2012). Therefore, preservation or increased expression of Nurr1 in neurons is a therapeutically desirable outcome in PD and related neurodegenerative disorders. In this regard, AAV-mediated gene delivery of Nurr1 and the forkhead transcription factor, Foxa2, preserved TH-positive neurons in a mouse model of PD (Oh *et al.*, 2015). When we expressed full length human Nurr1 in N2A cells (Fig 2A-D), C-DIM12 treatment increased expression of the Flag-tagged protein, as determined by immunofluorescence labeling for both Flag and Nurr1. Similarly, C-DIM12 increased expression of Nurr1 and TH in primary mouse dopaminergic neurons isolated from the ventral midbrain at E18 (Fig 2E-G). The capacity of C-DIM12 to increase protein levels of both exogenous human Nurr1 as well as to enhance expression of native Nurr1 protein in primary DA neurons suggests that C-DIM12 is a

direct regulator of Nurr1 in neurons. To examine the direct neuroprotective effect of C-DIM12 in functionally mature neurons compared to undifferentiated neuronal cells, we exposed differentiated MN9D cells and undifferentiated N2A cells to increasing concentrations of 6-OHDA in the presence and absence of C-DIM12. Differentiated MN9D neurons were less sensitive to 6-OHDA than undifferentiated N2A cells, with an LD₅₀ of 100 μM 6-OHDA, compared to 10 μM 6-OHDA in N2A cells (Figure 3C,E). This is consistent with other studies of 6-OHDA in MN9D cells and with similar studies comparing the response of differentiated and undifferentiated neuronal cells to mitochondrial toxicants (Polunas *et al.*, 2011). Moreover, undifferentiated N2A cells may share phenotypic similarity with other immortalized cell lines, which may render them less sensitive to the protective effects of C-DIM12 (X Li *et al.*, 2012). Concurrent treatment of MN9D and N2A cells with C-DIM12 and 6-OHDA at the LD₅₀ for each cell type significantly increased cell viability, particularly in differentiated MN9D neurons (Figure 3D,F), indicating that C-DIM12 provides direct neuroprotective benefit, although the underlying mechanisms require further investigation. Functionally mature MN9D neurons are also more similar to dopamine neurons than undifferentiated N2A cells and may therefore be more responsive to the neuroprotective effects of C-DIM12, similar to the perseveration of DA neurons we reported in the MPTP/probenecid model of PD, where levels of Nurr1 were strongly induced in TH-positive soma in the substantia nigra pars compacta (De Miranda, Popichak, Hammond, Jorgensen, *et al.*, 2015).

3.5 FIGURES

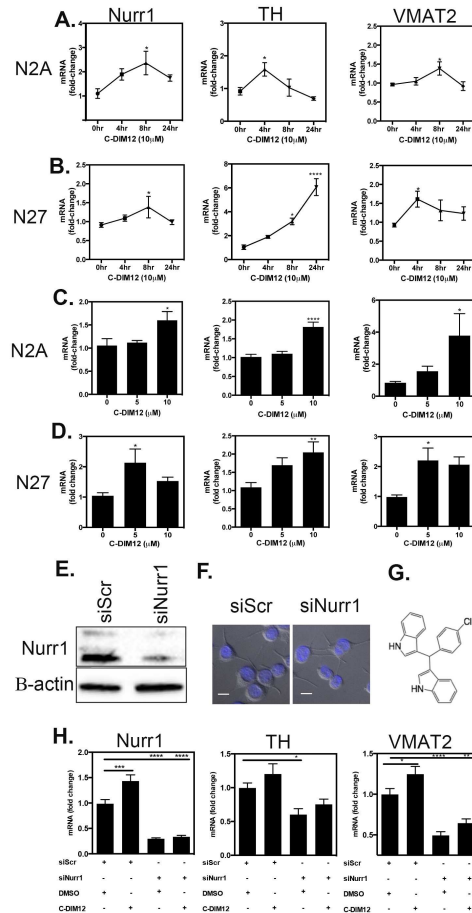


Figure 3.5.1 C-DIM12 induces expression of Nurr1-regulated genes in dopaminergic cell lines by Nurr1 dependent mechanism. Levels of mRNA for Nurr1, VMAT2 and TH were measured by qPCR in N2A (**A**) and N27 cells (**B**) following treatment with C-DIM12 (10 μM) for 4, 8 and 24 hrs. Dose-dependent changes in mRNA for Nurr1, VMAT2 and TH were measured by qPCR in N2A (**C**) and N27 cells (**D**) following treatment with vehicle control (DMSO) or C-DIM12 (5 and 10 μM) for 4, 8 and 24 hrs. * $p < 0.05$, ** $p < 0.01$, **** $p < 0.0001$, $n = 3-4$ biological replicates across 3 independent experiments. (**E**) Protein samples collected from N2A cells transfected with scrambled control sequence (siScr) and Nurr1 siRNA (siNurr1) were examined for expression of Nurr1 and β-actin as a loading control. (**F**) Morphology of N2A cells was determined following transfection with siScr and siNurr1 using differential interference contrast (DIC) imaging. Nuclei were counterstained with DAPI and visualized by fluorescence microscopy. Scale bar = 10 μm. (**G**) mRNA levels of Nurr1, TH and VMAT2 were measured by qPCR in N2A cells transfected with siScr or siNurr1 in the presence or absence of C-DIM12 for 24 hrs. * $p < 0.05$, ** $p < 0.01$, **** $p < 0.0001$, $n = 3-4$ biological replicates across 3 independent experiments.

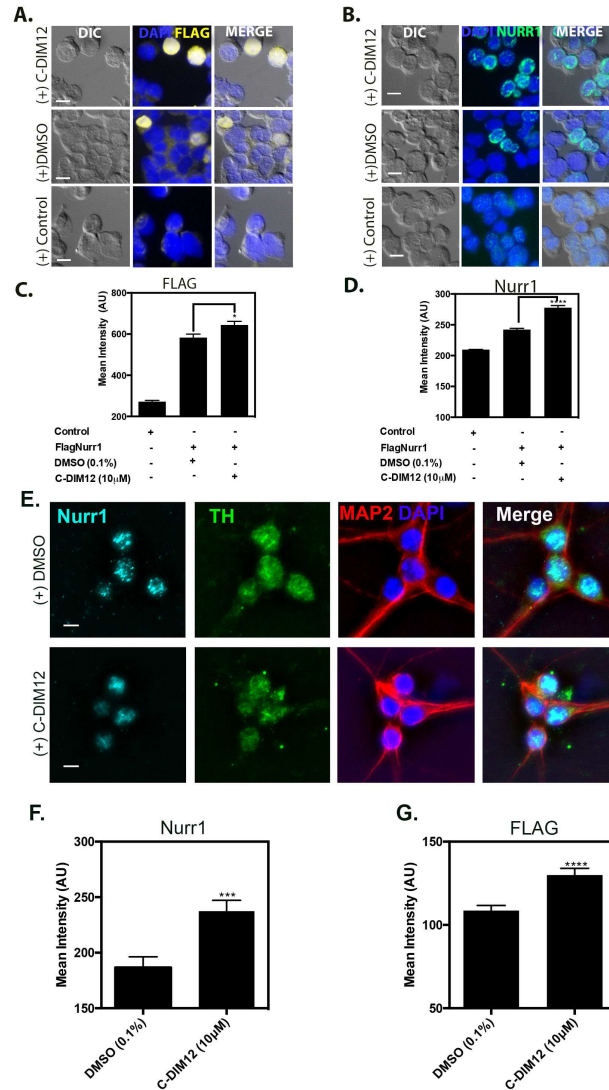


Figure 3.5.2 C-DIM12 induces expression of transfected human Nurr1 in N2A cells and induces expression of TH in primary dopaminergic neurons. (A, B) N2A cells were transfected with FLAG-Nurr1 or vector control and treated with C-DIM12 or DMSO for 24 hrs. Fixed cells were stained with anti-FLAG (yellow) and anti-Nurr1 (green) counterstained with DAPI (blue) and imaged using DIC and fluorescence microscopy. **(C, D)** Quantification of FLAG and Nurr1 fluorescence intensity in transfected N2A cells (arbitrary units, AU). * $p < 0.05$, **** $p < 0.0001$. $n = 100-200$ cells from three biological replicates across 3 independent experiments. **(E)** Primary mouse dopaminergic neurons were treated for 24 hrs with 10 μ M C-DIM12 or 0.1% DMSO (vehicle control) and immunostained for Nurr1 (cyan), Tyrosine Hydroxylase (TH, green) or MAP2 (red) and counterstained with DAPI (blue). Fluorescence images were acquired using a 40X air Planapochromat objective with a 1.6X optivar lens (64X total magnification, scale bar = 10 μ m). **(F)** Nurr1 and **(G)** TH protein levels were quantified based on fluorescence intensity in TH⁺ cells. *** $p < 0.001$, **** $p < 0.0001$ $n = 100 - 200$ cells per group from three biological replicates across 3 independent experiments.

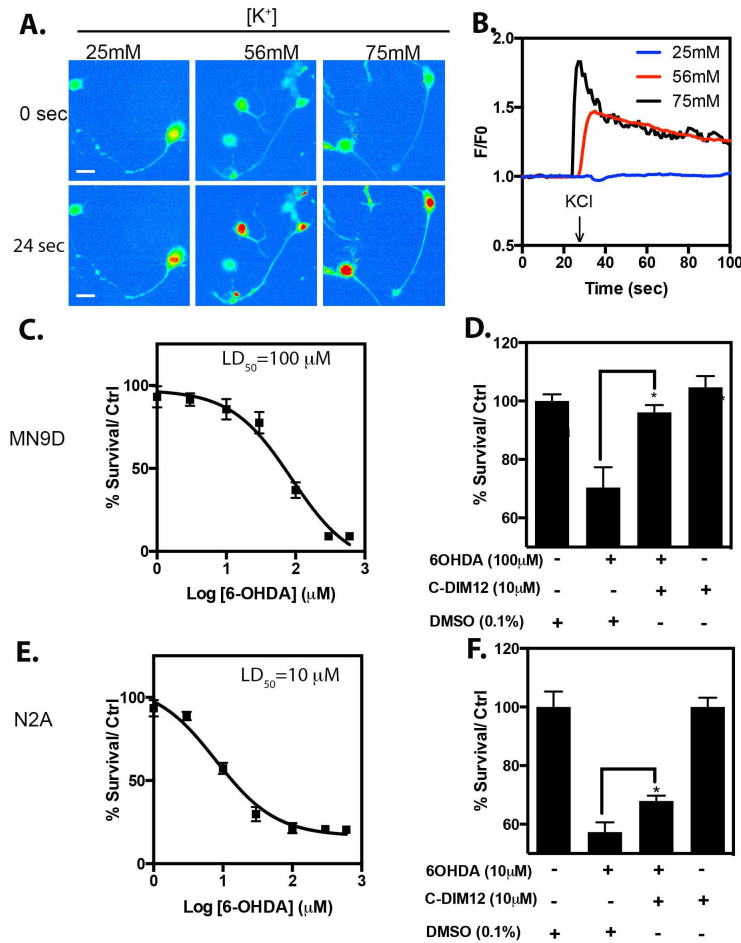


Figure 3.5.3 Treatment with C-DIM12 is neuroprotective against 6-hydroxydopamine in MN9D and N2A cells. (A) Pseudocolor images of Ca²⁺ influx pre-treatment (0 seconds) and upon administration of 25mM, 56mM and 75mM KCl (24 seconds) in live differentiated MN9D cells. 20X objective, Scale bars=10 μm. (B) Trace plots of dose dependent KCl induced Ca²⁺ influx over time, 8-16 cells from n=3 biological replicates. Arrow=KCl administration. (C, E) ½ log dosage of 6-OHDA administered to differentiated MN9D and undifferentiated N2A cells for LD₅₀ curve, n=6 biological replicates. (D, F) Cell viability of differentiated MN9D and N2A cells treated +/- 6-OHDA (100 μM) and +/- C-DIM12 (10 μM). *p<0.05.

CHAPTER 4

THE NURR1 LIGAND, 1,1-BIS(3'-INDOLYL)-1-(*P*-CHLOROPHENYL)METHANE, MODULATES GLIAL REACTIVITY AND IS NEUROPROTECTIVE IN MPTP-INDUCED PARKINSONISM

4.1 INTRODUCTION

Gene expression necessary for the synthesis and regulation of the dopamine (DA) in neurons of the substantia nigra *pars compacta* (SNpc) is controlled by the orphan nuclear receptor related 1 (Nurr1 or NR4A2) protein (Zetterström *et al.*, 1996; Sakurada *et al.*, 1999). Nurr1 is highly expressed in the ventral midbrain and is down-regulated in Parkinson's disease (PD) patients (Kadkhodaei *et al.*, 2013; Montarolo *et al.*, 2016). The homeostatic function of Nurr1 in DA neurons is mediated by nuclear binding to the nerve growth factor binding recognition element (NBRE) as monomers, homodimers or heterodimers with the co-activator protein retinoic acid receptor (RXR) (Saijo *et al.*, 2009; García-Yagüe *et al.*, 2013). NBRE sequences are recognized in the upstream promoter regions of DA genes such as tyrosine hydroxylase (TH), vesicular monoamine transporter 2 (VMAT2), dopamine transporter (DAT) and aromatic amino acid decarboxylase (AADC) (Smits *et al.*, 2003). Thus, Nurr1 activity is crucial for DA neuronal differentiation during development to maintenance throughout adulthood (Sakurada *et al.*, 1999; Jankovic *et al.*, 2005).

Homozygous Nurr1 (-/-) mice do not survive past 1 day postnatal and Nurr1 (+/-) mice are more susceptible to 1-methyl-4-phenyl-1,2,3,6-tetrahydropyridine (MPTP)-induced neurotoxicity (Saucedo-Cardenas *et al.*, 1998; Le *et al.*, 1999). Inhibition of

mitochondrial complex 1 by the active metabolite of MPTP, MPP⁺, causes loss of dopamine neurons in the nigro-striatal system and is accompanied by significant glial activation and neuroinflammation that is thought to exacerbate neuronal injury (Wu *et al.*, 2003; Glass *et al.*, 2010; Parillaud *et al.*, 2017). Nurr1 is now recognized as a critical regulator of inflammatory gene expression in glial cells, where it acts as a tonic regulator of NF- κ B-regulated inflammatory genes by stabilizing nuclear co-repressor proteins at p65/p50 *cis*-acting promoter elements, thereby limiting expression of inflammatory genes (Saijo *et al.*, 2009).

Despite the known transcriptional regulatory functions of Nurr1 (NR4A2), an endogenous ligand for this receptor is yet to be identified. Therefore, like Nur77 (NR4A1) and Nor1 (NR4A3), Nurr1 is classified as an orphan nuclear receptor (Safe *et al.*, 2015). However, multiple studies have demonstrated modulation of Nurr1 transcriptional activity using synthetic compounds (Ordentlich, 2003; X Li *et al.*, 2012; Smith *et al.*, 2015). Our previous studies using several phenyl-substituted diindolylmethane (C-DIM) compounds demonstrated that selected analogs are structure-dependent activators of NR4A orphan nuclear receptors (Inamoto *et al.*, 2008; Safe *et al.*, 2008). One compound from this series with high specific activity toward Nurr1, 1,1-bis(3'-indolyl)-1-(*p*-chlorophenyl)methane (C-DIM12) activates Nurr1 and induces antineoplastic effects in cancer cells (X Li *et al.*, 2012). We also reported that C-DIM12 inhibits expression of NF- κ B-regulated genes in glial cells and induces a dopaminergic phenotype in neuronal cell lines (De Miranda, Popichak, Hammond, Jorgensen, *et al.*, 2015; Hammond *et al.*, 2015). RNAi knockdown of Nurr1 in both glia and neurons ablated the effects of C-DIM12 in each cell type, demonstrating that in neural cells C-DIM12 acts through a Nurr1. *In vivo*, C-DIM12

displayed favorable pharmacokinetics and neuroprotective efficacy with oral dosing, including high bioavailability and distribution to the CNS, as well as protection against loss of dopamine neurons in the SNpc in the MPTP/probenecid (MPTPp) model of PD (De Miranda *et al.*, 2013; 2014). These studies demonstrating that C-DIM12 inhibits neuroinflammatory activation of microglia and astrocytes and protects against loss of dopamine neurons. However, it remains to be determined whether lower doses of C-DIM12 will have similar pharmacodynamic efficacy during concurrent lesioning with MPTPp will provide a similar degree of protection against an ongoing neurotoxic insult mimicking the complex I deficits in PD.

Based on the demonstrated neuroprotective and anti-neuroinflammatory effects of C-DIM12, we postulated that this Nurr1 activator would protect against loss of dopaminergic neurons during lesioning with MPTPp, despite the neurotoxic stress of mitochondrial complex 1 inhibition. To test this hypothesis, C57BL/6 mice were dosed with MPTPp twice weekly for two weeks and concurrently given C-DIM12 (25 mg/Kg daily, p.o.) once daily throughout the treatment period. Neurobehavioral analysis was conducted during the study to detect motor deficits consistent with depletions in nigro-striatal dopamine. Brain tissue (SN and ST) was collected to determine pharmacokinetic parameters of C-DIM12 at this dose, as well as stereological determination of dopamine neuron numbers, glial activation and qPCR array measurement of gene expression for inflammatory and cell death pathways. In addition, we conducted transactivation reporter studies in neural cell lines, as well as *in silico* modeling to identify putative binding sites for C-DIM12 within the ligand binding domain of human Nurr1. These findings demonstrate that C-DIM12 is an activating ligand of Nurr1 that induces an anti-

inflammatory phenotype in glial cells and preserves dopaminergic soma even during concurrent lesioning with MPTPp.

4.2 MATERIALS AND METHODS

Chemicals and Reagents

C-DIM12 was synthesized and obtained by Dr. Stephen Safe's laboratory at Texas A&M. Working concentrations of C-DIM12 were diluted in corn oil and sonicated in hot water bath until solubilized. MPTP (Sigma, St. Louis MO) was solubilized at final working concentration in saline (0.9% NaCl₂). Probenecid (Sigma, St. Louis MO) was prepared in 5% sodium bicarbonate/MilliQ water to final working concentration (pH 7.5). All additional reagents were obtained by Sigma Aldrich (St. Louis MO), unless stated otherwise.

Animals and Treatment Regimen

Inbred C57/Bl6 male mice (~24 weeks of age; 25-30 grams in weight) were acquired by Charles River Laboratories (Wilmington, MA) and housed on 12-hour light/dark cycles in a temperature-controlled room (maintained at 22-24°C) with access to standard chow and water *ad libitum*. Mice were administered C-DIM12 (25mg/kg) or corn oil (vehicle control) by oral gavage. Mice were dosed with MPTPp twice weekly for two weeks, with each dose delivered 2 days apart. On the day of dosing, probenecid was delivered in the morning by intraperitoneal injection (100 mg/kg) and then MPTP (20 mg/kg) or saline (0.9%NaCl) was administered 4 hrs later by subcutaneous injection, per our previously published protocol (De Miranda et al. 2014). C-DIM12 or corn oil was administered daily by intragastric gavage (14 doses total) throughout the treatment period. At the conclusion of the study, mice were anesthetized under deep isoflurane anesthesia and transcardially

perfused with 0.1M phosphate buffered saline (PBS)-cacodylate/heparin (10 U/mL) and 3% paraformaldehyde/PBS. Post perfusion, brains were dissected and stored in paraformaldehyde at 4 °C overnight, and then stored in sodium-cacodylate-PBS (pH 7.2) containing 15-30% sucrose at 4°C until processed for cryo-sectioning. For neurochemical sample collection, animals were also administered deep isoflurane before rapid removal of striatum and ventral midbrain for flash freezing in liquid nitrogen. Brain samples were then transferred to -80°C storage until processed for RNA, protein and HPLC analysis.

Real-time video gait analysis and open field behavioral testing. Changes in gait were determined by analysis of unrestricted movement along a fixed trackway using a video-based system constructed in our laboratory. Briefly, mice were allowed to walk along a 2 m long glass trackway with fixed sides and top that was illuminated with green LED lights such that paw placement results in total internal reflection of light downward toward a high speed video camera for digital recording. Animals were backlit from above with low power red LED lights to distinguish the silhouetted form of the mouse (black) from paw prints (green) for digital analysis. Incentive to traverse the trackway was provided by placement of the animal's home cage at the end of the trackway, thereby permitting reliable detection of unrestricted gait and motion. Mice were habituated to the trackway once daily for two days prior to the onset of the treatment period and a baseline of gait was recorded on the first day of the study prior to dosing with MPTPp. Video recording of mouse gait was filmed using a GoPro Hero3+ camera at 60 fps, 1080 dpi (GoPro; San Mateo, California) and analysis code was written in Matlab (Mathworks; Natick, MA) in conjunction with the Department of Electrical and Computer Engineering at Colorado State University.

field activity parameters were acquired with Versamax System (Omnitech Electronics, Inc; Columbus Ohio). Mice were allowed to acclimate to OFT behavioral chambers for two days prior to study for measurement of x-, y- and z-planes of activity for a monitoring period of 5 minutes under white noise and ambient light. OFT activity was then monitored for animals on day 0, 7, and 14 of study. Parameters were analyzed utilizing Fusion (Omnitech Electronics, Inc; Columbus Ohio) software for detection of total margin and center time activity. All Values were normalized for the difference from day 0 baseline.

Three-dimensional design-based stereology of neuronal cell bodies and assessment of striatal terminal density. Stereological determination for the number of neurons in the substantia nigra *pars compacta* was performed using a 3D design-based stereology method as we previously reported (De Miranda *et al.*, 2014). The entire SNpc was serially sectioned from rostral to caudal, which was demarcated by the subthalamic nucleus to the retrorubal field, respectively. Every fifth free-floating section (10 total) was selected from each animal and immunostained with antibodies against tyrosine hydroxylase (TH; Abcam) and MAP2 (Abcam). Stereological counting of both cell markers was performed using Slidebook software (version 5.0, Intelligent Imaging Innovations, Denver CO). The SNpc boundary was marked on a 10x-objective montage image of entire section. Optical fractionator method was employed with randomized 40x-objective z-stack image sampling setup frame size (100 X 100 μ m), frame spacing (200 X 200 μ m), dissector height (30 μ m), and upper guard distance (2 μ m). Each z-stack image was blindly quantitated for TH⁺ and MAP2⁺ cells to calculate a total estimate of neuronal cell bodies within the SNpc of each animal. For measurement of TH⁺ striatal terminals, two striatum sections/per animal with similar anatomical landmarks were selected and

immunostained for TH. 10x-objective montage images were generated for a masked outline of the caudate putamen. Each masked region was normalized for background subtraction and quantified for mean intensity fluorescence of TH.

Immunofluorescence staining

All brain tissue processed for IF was frozen with OCT on microtome stage and sectioned/collected for ST (25 μm in thickness) and SN (40 μm in thickness) regions. Tissue sections were stored in cryoprotectant (30% sucrose, 30% ethylene glycol, 0.5M phosphate buffer; pH 7.2) at 20°C until selected for immunostaining. IF staining was conducted as previously described by Miller et al. 2011, and all antibody dilutions were 1:500, unless stated otherwise (Miller *et al.*, 2011). For stereology, SN sections were immunostained with anti-tyrosine hydroxylase (Millipore AB152) and anti-MAP2 (Abcam AB5392). For gliosis, SN and ST sections were immunostained with either anti-IBA1 (1:250; Wako 016-20001) or anti-GFAP (Dako Z0334) and anti-tyrosine hydroxylase (Abcam AB76442). SN tissue was also immunostained with anti-TH and anti-Nurr1 (1:200; Santa Cruz SC991) for mean intensity measurements of Nurr1. All secondary antibodies used for IF were alexa flour 488, 555, and 647 (LifeTech, Carlsbad CA).

Measurement of Gliosis and Immunofluorescence Imaging

Quantitation of IBA-1⁺ and GFAP⁺ cells bodies was conducted on two sections of the SNpc and ST regions/per animal. Optical fractionator method employed was adjusted with counting frame size (150 X 150 μm) and frame spacing (for SN; 250 X 250 μm , for ST; 550 X 550 μm). Blind quantitation of cell bodies for relative number of glial cells per region was conducted on 40x z-stack images of IBA⁺ cells from the SNpc. Same IBA1⁺ cell images were also converted to a max projection, following a binary transformation

and then rendered to a skeletonized image in ImageJ, as previously described in Morrison and Filosa et al. 2013 (Schneider *et al.*, 2012; Morrison and Filosa, 2013). Images for quantitative measurements were all acquired with a Zeiss Axiovert 200M inverted fluorescent microscope equipped and a Hamamatsu ORCA-ER-cooled charge coupled device camera using a 10x and 40x air objective (Hamamatsu Photonics, Hamamatsu City, Japan). High magnification representative images were generated with a Plan-Apochromat 100X oil objective lens. High magnification images of three-dimensional IBA1+ cells were acquired with a 63X objective lens on a Zeiss LSM 510 laser-scanning confocal microscope, using Zen software (Oberkochen, Germany). Z-stack images of microglia were surfaced rendered in Imaris software (Bitplane; Zurich, Switzerland) for voxel view of morphology. Low magnification montage images of tissue sections were acquired with an air 10x-objective lens using a Hamamatsu ORCA-Flash4.0 digital CMOS camera, ProScan III stage controller (Prior, Rockland, MA USA) and CellSens Dimension software (version 1.12, Olympus, Center Valley, PA, USA).

Western blotting.

Striatal tissue was homogenized and lysed in RIPA buffer with protease inhibitor for western blot analysis. Protein concentration was determined using a BCA protein assay kit (ThermoScientific, Pierce Rockford, IL). 30 μ g of protein was loaded into a polyacrylamide 12% separating and 4% stacking gel. Anti-DAT (1:500; Millipore Ab1591P), anti-VMAT2 (1:750; gift from Dr. Gary Miller's Laboratory, Emory University), anti-TH (1:1000; AB152), anti-Nurr1 (1:100; SC991), anti-GFAP (1:1000; Z0334) and anti-Beta Actin (1:2000; Sigma A1978) were diluted in 5% milk/tris-buffered saline with tween (0.1%) blocking buffer. All western blots were imaged on a BioRad ChemiDoc MP imaging

system and raw TIFF files were analyzed for mean optical band density with ImageJ analysis software (Schneider *et al.*, 2012).

Pharmacokinetic Analysis of C-DIM12 and Determination of Catecholamine Content

For PK analysis of C-DIM12, male C57/Bl6 mice (27-30g) were administered C-DIM12 (25 mg/kg) dissolved in corn oil by intragastric gavage. Post administration, mice were euthanized at 0, 0.5, 1, 2, 4, 8, and 24 hours ($N=4$ /per time point) by decapitation under isofluorane anesthesia. Midbrain tissue samples were rapidly dissected using a 1 mm brain block. Plasma samples were collected from trunk blood and centrifuged at 1,500 rpm for 5 minutes. Frozen brain and plasma samples were then processed for liquid chromatography mass spectrometry (LC-MS) by the Pharmacology Core at Colorado State University as reported in previous studies from our group (De Miranda *et al.*, 2013). Striatal samples from each experimental group were measured for dopamine and DOPAC by high performance liquid chromatography (HPLC) coupled with electrochemical detection. The Neurochemistry Core Laboratory at Vanderbilt University's Center for Molecular Neuroscience Research group (Nashville, TN) processed all tissue samples from each experimental group with coded labeling for unbiased analysis.

Computational Modeling

Small molecule docking studies were conducted using Accelrys Discovery Studio 4.5 (Accelrys Inc., San Diego, CA) and the crystal structure coordinates for the human Nurr1 (NR4A2) ligand binding domain (PDB ID: 1OVL) (Wang, et al 2003, Nature 423: 555-560) were downloaded from the protein data bank (<http://www.rcsb.org/pdb>). The protein was prepared and subjected to energy minimization utilizing the conjugate gradient

minimization protocol with a CHARMM forcefield (Brooks *et al.*, 2009) and the Generalized Born implicit solvent model with simple switching (GBSW) (Feig *et al.*, 2004) that converged to an RMS gradient of < 0.01 kcal/mol. The Flexible Docking protocol (Koska *et al.*, 2008), which allows flexibility in both the protein and the ligand during the docking calculations, was used to predict the binding of C-DIM12 in the regions of both the coactivator and ligand binding pockets of NR4A2. Predicted binding poses were energy minimized *in situ* using the CDOCKER protocol (G Wu *et al.*, 2003) prior to final ranking of docked poses via consensus scoring combining the Jain (Jain *et al.* 1996), PLP2 (Parill *et al.* 1999), and Ludi3 (Böhm *et al.* 1994) scoring functions. Predicted binding energies were calculated using the distance-dependent dielectric model.

Transfections and luciferase assays

Neuron-like, PC12 cells were plated on 12-well plates at 2.5×10^5 per well in DMEM/F12 supplemented with 2.5% charcoal-stripped FBS and were allowed to attach and settle for overnight. Luciferase plasmids (UAS_{x5}-Luc, NBRE_{x3}-Luc and NurRE_{x3}-Luc) and corresponding expression plasmids (GAL4-NR4A2 or FLAG-NR4A2) were co-transfected in cells at 10:1 ratio, i.e., 1000 ng Luc and 100 ng NR4A2 per well. Lipofectamine 2000 reagent was used for transfection according to the manufacturer's protocol and all plasmids have previously been described (Li *et al.*, 2012). After 6 hr of transfection, cells were treated with medium (as above) containing either solvent (DMSO) or the indicated concentration of C-DIM12 for 18 hr. Cells were then lysed using a freeze-thaw protocol and cell extracts were used for luciferase assays. Luciferase activity values were normalized against corresponding protein concentrations determined in a Bradford assay.

Luciferase assays were run in triplicate for each determination and results are expressed as mean \pm SD.

RNA isolation and RT-qPCR array analysis

Midbrain tissue samples from each experimental group were homogenized and lysed using Qiashredder columns along with on-column and in solution DNase treatment (Qiagen; Hilden, Germany). Samples were purified for RNA using an RNeasy kit, eluted with RNase-free water and concentrations were determined using a Nanodrop One spectrophotometer (ThermoScientific; Waltham, MA). mRNA was reverse transcribed to cDNA with iScript (Biorad, Hercules, CA) reverse transcriptase enzyme for a total of 250 ng and qPCR reactions were prepared in SYBRgreen mastermix (BioRad; Hercules, CA). Samples from each experimental group were amplified using RT² profiler PCR arrays (Qiagen; Hilden, Germany) for NF- κ B signaling pathway target genes (PAMM-025ZG-4) and Parkinson's disease associated genes (Cat#: PAMM-124ZG-4) for a total analysis of 168 genes. Both sets of 384-well pathway array plates were run according the manufacturer's protocol on a Lightcycler 480 real time PCR instrument (Roche; Branford, CT, USA). Gene expression fold change was analyzed using the SAbiosciences software.

Statistical Analysis

Data was presented as the mean \pm SEM, unless noted otherwise. All experimental values from each mean were analyzed with a Grubb's ($\alpha=0.05$) test for exclusion of significant outliers. Differences between three experimental groups were analyzed with a one-way ANOVA followed by a Tukey *post hoc* multiple comparisons test. Two group comparisons for densitometry analysis was conducted with an unpaired student's t-test followed by Welch's correction. A two-way ANOVA was performed when incorporating

'day' as an experimental variable for behavioral tests. Significance was identified as $^{**}P < 0.01$, $^{*}P < 0.05$, $^{**}P < 0.01$, $^{***}P < 0.001$, $^{****}P < 0.0001$. All statistical analyses were conducted using Prism (version 6.0; Graph Pad Software, San Diego, CA).

4.3 RESULTS

C-DIM12 is highly concentrated in brain tissue

We previously conducted neuroprotection studies with several C-DIM compounds known to activate NR4A1 or NR4A2, using daily oral dosing at 50 mg/kg (De Miranda *et al.* 2014). To determine whether a lower dose would have similar neuroprotective efficacy, we first performed a pharmacokinetic study with C-DIM12 (chemical structure in **Fig 1A**) at 25 mg/kg by administering this dose *per oral* and sampling plasma and brain concentrations at 0, 0.5, 1, 2, 4, 8 and 24 hrs. Plasma and midbrain samples were analyzed by LC-MS analysis per our previously published methods (De Miranda 2013 *et al.*). As shown in **Figure 1A-C**, C-DIM12 reached a maximum concentration (C_{max}) at 4 hrs of 1120.0 ± 404.7 ng/ml and 3622.5 ± 1430.8 ng/g in plasma and brain, respectively. The half-life was 249 ± 23 min in plasma and 264 ± 17 min in brain, approximately 15 minutes longer in brain tissue compared to plasma (**Fig.1C**). Timing for C_{max} and total drug clearance is consistent with the previous dosage of 10mg/kg (**Fig 1A-B**) ($N=4$ animals/per time point).

Daily Administration of C-DIM12 protects against loss of dopaminergic neurons during con-current neurotoxic challenge with MPTP/probenecid.

Brain tissue was collected after 14 days of concurrent dosing with MPTPp and the presence or absence of C-DIM12 (25 mg/Kg), as depicted in dosing schematic in **Figure 2A**. Immunofluorescence images were generated for number of TH⁺ cell bodies (red) in

the SNpc on tissue from Saline + corn oil (C.O.) (**Fig. 2B**), MPTPp + C.O. (**Fig. 2F**), and MPTPp + C-DIM12 (**Fig. 2J**) experimental groups, as depicted in representative images. The total number of neurons was determined by staining with the general neuronal marker, mitogen-associated protein, MAP2 (green) (**Figure 2C, G, K**). Based on unbiased 3D-design based stereological quantitation of the number of TH⁺ neurons in the SNpc, mice treated with MPTPp+C.O. had a 63.75±4.27% loss of TH⁺ neurons, whereas mice treated with MPTPp+C-DIM12 had only a 35.28±8.46% loss of TH⁺ neurons (**Fig. 2N**). Similarly, loss of MAP2⁺ cells was 48.00±4.74% in the MPTP+C.O. treatment group, in contrast to only 25.50±7.92% loss of total neurons in mice lesioned with MPTPp in the presence of C-DIM12 compared to control (**Fig 2O**) (**P*<0.05, ***P*<0.01, *****P* <0.0001; *N*=10 animals/group). TH⁺ fiber innervations of the striatum were also immunostained as depicted in representative images of Salinep+C.O. (**Fig 2E**), MPTPp+C.O.(**Fig 2I**) and MPTPp+C-DIM12 (**Fig 2M**). Density of TH⁺ fibers was measured by mean pixel intensity of the caudate putamen region and compared back to saline control (set at 100%). Mice treated with MPTPp+C.O. had 81.05±1.05% loss of TH⁺ terminals in the ST compared to only a 62.92±6.40% loss of TH⁺ fibers in mice treated with MPTPp+C-DIM12 (**Fig 2P**) (**P* < 0.05; *n*=12 animals/per group). Thus, treatment with C-DIM12 reduced loss of TH⁺ fibers in the ST but did not completely protect against MPTPp-induced damage to innervating dopaminergic fibers projecting from the SNpc.

Assessment of neurobehavioral deficits associated with PD and neurochemical analysis of the nigrostriatal system.

Neurobehavioral function was assessed by open-field activity testing (OFT) on days 0, 7 and 14 during the 2-week study. Mice treated with MPTP+C.O. spent

significantly less time in the center of the chamber (dotted line represents baseline subtracted from Day 0) compared to controls, whereas the MPTP+C-DIM12 treatment group was not significantly different from control or the MPTPp+C.O. group at day 14 (**Fig. 3A**). Quantitation of time spent along the margins of the chamber (a measure of anxiety) indicated that MPTP+C.O. treated mice spent significantly more time in the margin compared to saline controls. Mice treated with MPTPp+C-DIM12 were not significantly different from controls or the MPTPp+C.O. group at day 14 (**Fig. 3B**) ($*P < 0.05$; $N=19-25$ animals/per group). Individual time traces and pseudocolored heat maps of activity across area over time (red=most time, blue=least time) plots from day 14 of OFT in each treatment group are represented in **Figure 3C**, demonstrating the trend toward decreased center time and increased margin time in MPTPp-treated mice that was prevented by concurrent treatment with C-DIM12. To assess locomotor function, we utilized a real-time video analysis system to determine stride length along a fixed track to measure alterations in gait related to changes in striatal dopamine. Representative images of illuminated paw print coordinates generated from video analysis are depicted in **Fig. 3D**. The overall rate of movement along the trackway was analyzed independently for left front (LF), right front (RF), left rear (LR) and right rear (RR) paws to identify changes in gait for each treatment group (**Fig. 3E**). An increased number of stop times and a correspondingly slower overall traverse rate along the trackway was noted in mice treated with MPTPp+C.O., which was largely restored to control levels at day 7 in mice treated with MPTPp+C-DIM12. Hind limb stride length analysis at day 7 also indicated a significantly shorter stride in the MPTPp+C.O. group and longer stride length in MPTPp+C-DIM12 group ($*P < 0.05$, $**P < 0.01$; $N=6-12$ /animals/per group) (**Fig 3F**).

MPTPp+C.O. vs. MPTPp+C-DIM12 groups were not significantly different at day 14 and the stride length of Salinep + C.O. treated animals was decreased, potentially due to either stress or habituation to the trackway by the conclusion of the treatment period. High-performance liquid chromatography (HPLC) was performed on ST tissue for measurement of dopamine (DA) neurotransmitter content and its metabolite, 3,4-dihydroxyphenylacetic acid (DOPAC). Significantly less DOPAC and DA were detected in MPTP+C.O. and MPTP+C-DIM12 compared to saline control (**Fig 3G-H**). Mice treated with MPTPp+C-DIM12 showed a trend towards protection against loss of DOPAC and DA compared to the MPTPp+C.O. group, but this was not statistically significant. The DOPAC/DA ratio was also higher in MPTPp+C.O. compared to control mice and the MPTPp+C-DIM12 group showed an intermediate effect that was not different from either control or the MPTPp+C.O. group (** $P < 0.01$, *** $P < 0.001$; $N=9-10$ animals/per group) (**Fig 3I**). Proteins associated with the production and release of DA in ST tissue was also measured by western blot. Levels of TH were significantly depleted in both MPTPp+C.O. and MPTPp+C-DIM12 compared to saline control (set at 100%) but C-DIM12 treatment mitigated loss of TH compared to MPTP-only group (**Fig 3J**). Correspondingly, the amount of vesicular monoamine transporter 2 (VMAT2; $P=0.1125$), (**Fig 3K**) and dopamine transporter (DAT; * $P < 0.05$) (**Fig 3L**) were depleted in MPTPp+C.O. groups and higher in C-DIM12 treated animals ($N=6-8$ animals/per group).

C-DIM12 suppresses microglial activation and preserves a ramified morphological phenotype in the substantia nigra.

The relative number of microglia in the SN and ST were determined by immunostaining for ionized binding adaptor molecule (IBA-1; green), with counterstaining

for TH (red) to demarcate each region, as depicted in the representative images in **Fig 4A-C**. An increased number of activated microglia compared to control was evident in MPTPp-treated SNpc tissue (**Fig 4B-C**). To quantitate these observations, stereological assessment of IBA-1⁺ cells was performed on SNpc and ST. In the SNpc, an increased number of IBA-1⁺ cells were counted in both MPTP-receiving mice, characterized by intense staining for IBA-1 and a change in morphology from a ramified phenotype to a more amoeboid shape. C-DIM12 treatment significantly suppressed the number of IBA⁺1 cells in the SNpc compared to MPTP+C.O., however, in the ST the number of IBA-1⁺ was not significantly lower than in the MPTPp+C.O. group but also not significantly different from the control group ($P=0.1162$ for MPTPp + C.O. vs. MPTPp + C-DIM12, $**P < 0.01$, $****P < 0.0001$, $N=10$ animals/per group for SN and $N=12$ animals/group for ST) (**Fig 4D, E**). For analysis of a microglia morphological phenotype within the SNpc, the same 40X images used for IBA-1 counts were also rendered for skeletonization as depicted in the representative images in **Fig 4F**. Skeletonized images were quantitated for the number of branches/cell (**Fig 4G**), junction voxels/cell (**Fig 4H**), endpoint voxels/cell (**Fig 4I**) and average branch length/cell (**Fig 4J**). C-DIM12 increased the number and complexity of each morphological parameter, except average branch length/cell, which showed only a trend toward increase relative to the MPTPp-treated group ($++P < 0.1$), whereas all other parameters in the MPTPp+C-DIM12 group were increased comparably to the control group ($**P < 0.01$, $***P < 0.001$, $****P < 0.0001$, respectively; $N=6$ animals/per group). The morphology of IBA-1⁺ cells within the SNpc was also characterized by high-resolution confocal microscopy to visualize three-dimensional morphology (**Fig 4K, Supplemental Videos 1-3**). Multiple optical z-planes were acquired and rendered in 3D using Imaris

Bitplane software to produce volumetric surface renderings of microglia from each treatment group. Microglia in the SNpc of MPTPp-treated mice displayed a loss of ramified cytoplasmic processes and a generally amoeboid shape, whereas mice treated with MPTPp+C-DIM12 had a cellular morphology more consistent with microglia from the control group. Amoeboid-shaped microglia were also seen phagocytosing TH⁺ neurons in the SNpc in the MPTPp+C.O. group (see **Supplemental Video 4**).

C-DIM12 suppresses astrocyte activation during progressive DA neuronal loss.

Relative activation of astrocytes following MPTPp treatment was measured by quantitation of the intermediate filament, glial fibrillary acidic protein (GFAP), in cells in the SN and ST. Total levels of GFAP protein levels in the striatum were also analyzed by western immunoblotting. SN tissue was immunostained for GFAP (red) and TH (green) to delineate the *pars compacta* region for stereological counts, as depicted in high and low magnification representative images (**Fig 5A-C**). A basal level of GFAP⁺ expressing cells within the substantia nigra *pars reticulata* (SNr) was evident in saline control animals (**Fig 5A**) and astrocyte proliferation noticeably increased within the SNpc upon treatment with MPTPp (**Fig 5B**). Based on stereological counts of GFAP⁺ expressing cell bodies, MPTPp+C.O. treated animals exhibited significantly more astrocytes within the SNpc compared to saline control. Mice that received MPTPp + C-DIM12 had significantly fewer GFAP⁺ cells within the SNpc compared to MPTPp-only treated animals (**Fig 5C,D**). Similarly, C-DIM12 suppressed the number of GFAP⁺ cells within the ST comparable to saline control levels ($N=9$ animals/per group for SN, $N=6$ animals/per group for ST; $*P < 0.05$, $**P < 0.01$, $****P < 0.0001$) (**Fig 5E**). GFAP expression levels within the ST were also confirmed by western blot analysis, as depicted in **Figure 4F**. Based on optical

density measurements of GFAP protein, compared to control (saline set at 100%), C-DIM12 significantly decreased total levels of striatal GFAP ($*P < 0.05$; $N=4$ animals/per group) (Fig 4G).

C-DIM12 reverses MPTP-induced changes in gene expression related to PD and NF- κ B signaling.

To analyze patterns of gene expression in each experimental group, we isolated mRNA from midbrain tissue for real-time RT-PCR analysis of 168 genes in PD-associated and NF- κ B-regulated gene arrays. Heat maps for PD-associated (Fig 6A) and NF- κ B (Fig 6B) gene arrays depict ontology dendrograms indicating that transcript expression in the MPTPp+C-DIM12 group clustered with the saline (control) group, whereas mRNA levels in the MPTPp+C.O. segregated independently, based on clustergram analysis. Volcano plots for NF- κ B regulated (Fig 6C,D) and PD-associated genes (Fig 6E,F) identified a number of genes upregulated in the MPTPp+C.O. group relative to control (Fig 6 C,D) that were downregulated in the MPTPp+C-DIM12 group (Fig 6D,F). Several unique transcripts identified in volcano plots that were significantly altered by MPTPp but not different from controls in the MPTPp+C-DIM12 group included the plasma membrane Ca^{2+} transporting atpase (*Atp2b2*) (Fig 6G), cell death regulator B cell leukemia/lymphoma 2 related protein *Bcl2a1a* (Fig 6H), motif chemokine ligand *Ccl5* (*RANTES*) (Fig 6I), hypoxia-inducible factor prolyl hydroxylase 2 (*Egln10*) (Fig 6J), neural plasticity transcription factor early growth factor 1 (*Egr1*) (Fig 6K), synaptotagmin 1 (*Syt1*) (Fig 6L), tumor necrosis factor (ligand) superfamily, member 10 (*Tnfs10*) (Fig 6M) and TNF receptor associated factor 6 (*Traf6*) (Fig 6N) ($*P < 0.05$, $**P < 0.01$; $N=4$ animals/per group).

C-DIM12 maintains nuclear Nurr1 localization in DA neurons and prevents MPTPp-induced Nurr1 protein expression changes in SNpc and ST.

To visualize the subcellular localization of NR4A2/Nurr1 shuttling in DA neurons after treatment with MPTPp, we immunostained SNpc tissue for TH (green) and Nurr1 (red) protein expression, as depicted in the representative high-magnification images in **Figure 7A** (white arrows depict subcellular localization). Nuclear Nurr1 in TH⁺ neurons was quantified for mean fluorescence intensity and indicated higher levels of nuclear Nurr1 in DA neurons within the SNpc in mice treated with MPTPp+C-DIM12 compared to DA neurons in mice treated with MPTPp+C.O. (* $P < 0.05$, **** $P < 0.0001$; $N=3$ animals/per group) (**Fig 7B**). qPCR analysis of mRNA isolated from SN tissue also demonstrates a trend for increased expression of Nurr1 mRNA following C-DIM12 treatment (**Fig 7C**, $P < 0.1081$ compared to MPTPp +C.O.; $N=4$ animals/per group). mRNA expression data for the NR4A family member, Nur77 (NR4A1) display a 2.67 ± 0.79 -fold induction with C-DIM12 ($P=0.1154$ compared to MPTPp + C.O.; $N=4$ animals/per group) (**Fig 7D**). Additionally, total Nurr1 protein from ST tissue was analyzed by western blot and demonstrates a $39.5\pm 4.6\%$ depletion of Nurr1 with MPTP+C.O. that was prevented by treatment with C-DIM12 to $77.2\pm 14.40\%$ compared to control levels (**Fig 7E-F**).

C-DIM12 activates Nurr1-dependent transactivation and modeling interactions of C-DIM12 with Nurr1.

C-DIM12 also induced NR4A2-dependent transactivation in PC12 cells transfected with a GAL4-NR4A2 chimera (full length human NR4A2 fused to the yeast GAL4 DNA-binding domain) and a luciferase reporter gene construct containing five GAL4 response

elements (UAS-Luc) (**Fig 8A**). In addition, PC12 cells were transfected with NBRE-Luc and NurRE-Luc constructs containing binding sites for NR4A2 monomer and homodimer, respectively (Li et al, 2012) (**Fig 8B-C**). C-DIM12 activated transactivation in PC12 cells in all three assay systems with the highest responses observed for the GAL4-NR4A2/UAS-Luc assay (**Fig 8A**). To examine the potential for direct binding of C-DIM12 to Nurr1, we performed computational-based small molecule docking studies to predict its possible binding orientation in either the coactivator binding site or the ligand-binding site. The modeling results in **Figure 8D-F** indicated that C-DIM12 was predicted to bind with high affinity to the co-activator binding site (binding energy: -73.3 kcal/mol), with the chlorobenzene ring buried into the hydrophobic region of the pocket, which includes Mse414, Ile587, and Leu591 and the indole moieties participating in hydrogen bond interactions with Glu415, pi-anion and pi-sigma interactions with Glu440, and pi-cation interactions with Arg418. The only substantive predicted interaction at the ligand binding site involved a pi-cation interaction between one of the indole moieties and Arg515 (binding energy: -12.2Kcal/mol), with the balance consisting of comparatively weak hydrophobic interactions with Arg563, Cys563, and Leu570 (**Fig 8G-I**).

4.4 DISCUSSION AND CONCLUSIONS

Efficacy of small molecule therapeutics for neurodegenerative disease is dependent on the capacity to penetrate the blood brain barrier. We have previously demonstrated that selected C-DIM compounds have excellent structure-dependent bioavailability, with C-DIM12 having the greatest area under the curve (AUC) in brain compared to other *p*-phenyl substituted analogs when administered orally 50 mg/Kg daily (De Miranda *et al.*, 2013). To assess brain/plasma distribution at the lower dose of 25

mg/kg used in the current study, we administered C-DIM12 to mice orally over a 24 hr period and observed ~3.5 times greater C_{max} at 4 hours compared to our previous pharmacokinetic study that examined plasma and brain distribution at 10 mg/kg. At 25 mg/Kg p.o., the AUC in brain was ~4.2 times higher in brain than in plasma, representing a brain:plasma AUC ratio indicative of highly favorable penetrance of the CNS, as indicated by the data in **Figure 1**. This dose-dependent increase in brain levels of C-DIM12 confirms the utility of this analog for reaching the molecular target in brain as a pharmacological modulator of neuroinflammation.

At the time of diagnosis, an individual with PD has already lost approximately 60% of dopaminergic neurons in the SNpc and 70% of striatal dopamine (Marsden, 1982; O Cooper *et al.*, 2009). The subacute MPTPp mouse model used in this study conferred similar lesioning with approximately 63% loss of SNpc TH⁺ neurons, 52% loss of SNpc MAP2⁺ neurons and an 81% loss of DA terminals in the ST (**Fig 2M-O**). Based on stereological analysis of neuronal numbers after two weeks of exposure to MPTPp, concurrent treatment with C-DIM12 ameliorated neuronal loss to only 35% and 63% for DA cell bodies and terminals, respectively, compared to controls. However, C-DIM12 provided less protection against loss of striatal DA, which is consistent with the use of MPTP as a potent toxicant damaging neuronal mitochondria in nerve terminals in projecting dopaminergic fibers in the striatum (Giovanni *et al.*, 1994). The protective effect of C-DIM12 was consistently observed in MAP2⁺ neurons in the SNpc in addition to TH⁺ cells, demonstrating that neuroprotection was not confined to dopaminergic neurons only, but rather a general protective mechanism consistent with the anti-inflammatory activity of C-DIM12.

Subacute administration of MPTPp in C57/BL6 mice causes cognitive and locomotor dysfunction resembling that seen in PD (Goldberg *et al.*, 2011; XH Wang *et al.*, 2012; De Miranda *et al.*, 2014). Generally, anxiety-like, thigmotaxis behavior of mice is accompanied with reduced exploratory and spontaneous activity (Simon *et al.*, 1994; George *et al.*, 2008), consistent with the trends we observed in open field activity assays (**Fig 3A-C**). We also noted decreased hind limb stride length in MPTPp-treated mice that was prevented by co-treatment with C-DIM12 (**Fig 4D,F**), indicating protection against deprecations in striatal dopamine. However, this effect was not detected at day 14 (**Fig D-F**), possibly due to the characteristically severe loss of DA within the nigrostriatal system caused by MPTPp treatment that was partially prevented by C-DIM12 (**Fig 3G-I**). Yet, C-DIM12 preserved protein expression of TH within the striatum, as well as the synaptic and vesicular DA transporters, DAT and VMAT2 ($P = 0.1125$), respectively (**Fig 3J-L**). The transporter proteins were induced at higher levels upon C-DIM12 treatment compared to TH, suggesting an imbalance of DA transport within the ST or due to vulnerability of TH to MPP⁺ induced oxidation.

Animal studies suggest that microglial activation could be an etiologic factor in pathogenesis as well as a sequela of neurodegeneration due to MPTP exposure (PL McGeer and EG McGeer, 2008; Ramsey and Tansey, 2014). Regardless, microglial activation exacerbates DA neuronal loss, suggesting that suppressing inflammatory activation of microglia could be a viable therapeutic strategy for slowing the progression PD. Previous studies with the Nurr1 agonist, SA00025, showed that suppression of microglia activation and neuroinflammatory cytokine production was neuroprotective in the 6-hydroxydopamine (6-OHDA) rat model of PD (Smith *et al.*, 2015). Similarly, we

demonstrated that C-DIM12 blocked neuroinflammatory gene expression in LPS-treated BV-2 microglial cells (De Miranda *et al.*, 2014) and suppressed the relative number of IBA-1⁺ cells in the SNpc and ST following treatment with MPTPp *in vivo* (De Miranda *et al.* 2014). In the current study, microglial numbers were significantly reduced within the SNpc by concurrent treatment with C-DIM12, but only slightly in the ST (**Fig 4A-E**). Microglia within the SNpc were further examined to discriminate ramified, resting morphology from an amoeboid, activated-like cell type using three-dimensional IBA⁺ morphometric analysis (**Fig 4F-K, Supplemental Videos 1-3**). Based on the morphometry of skeletonized images, MPTPp+C.O. treatment reduced ramification and increased the number of phagocytic microglia surrounding dopamine neurons (**Fig. 4K and Supplementary Video 4**). C-DIM12 preserved a ramified morphology in SNpc microglia (**Fig. 4G-K**), indicating that inhibition of inflammatory activation directly correlated with preservation of dopaminergic soma.

Increased astrocyte proliferation and hypertrophy surrounding DA neurons occurs at approximately 3-4 days after MPTP exposure in mice (Breidert *et al.*, 2002; Hirsch and S Hunot, 2010). Although a certain level of astrogliosis may be neurotropic (Liddelow *et al.*, 2017), severe activation leads to neuronal death (Carbone *et al.*, 2008; Liddelow *et al.*, 2017). In astrocyte cultures, by neurotoxin-induced nitric oxide synthetase (NOS2), C-DIM compounds are potently anti-inflammatory and neuroprotective (Tjalkens *et al.*, 2008; Carbone *et al.*, 2008). Based on the gliosis quantitation of GFAP⁺ cells in both the SNpc and ST, concurrent C-DIM12 treatment suppressed gliosis in both regions (**Fig 5A-E**). Interestingly, there was greater reduction of striatal GFAP⁺ astrocytes than striatal IBA-1⁺ microglia (**Fig 5E-G, 4E**). This cell specific effect of C-DIM12 could be due to an

established deficit of striatal IBA-1⁺ cells by the end of MPTPp treatment regimen, or astrocyte activation persists as a more chronically activated state in PD animal models (Hirsch and SP Hunot, 2009). Overall, C-DIM12 appears to modulate both glial cell types in MPTPp-induced models, suggesting C-DIM12's regulatory role of inflammatory gene expression to be a promising neuroprotective mechanism.

Neuroinflammatory gene expression mediated by NF- κ B is up-regulated in PD post-mortem brain tissue (Hirsch and SP Hunot, 2009)). It is also essential for glial crosstalk signaling and has been demonstrated to be effected by multiple Nurr1 agonists in *in vivo* models (Kirkley *et al.*, 2017; Smith *et al.*, 2015; De Miranda *et al.*, 2015). Based on heat map analysis of 168 genes from both qRT-arrays, C-DIM12 gene pattern expression was clustered similarly to Saline control levels compared to MPTP+C.O. treatment (**Fig 6A-B**). When comparing fold change levels from both gene arrays, NF- κ B related genes were more prominently regulated by C-DIM12 than genes from the PD array (**Fig 6C-F**). This included *Traf-6*, *Tnfsf10*, *CCl5*, *Bcl2a1a*, and *Egr1*. Genes differentially regulated by C-DIM12 under the PD array were calcium homeostasis genes *Atp2B2* and *Syt1*, as well as the redox sensing transcription factor *Egn1* (**Fig 6G-N**). These data indicate that C-DIM12-Nurr1 transcriptional activation may modulate death signaling regulated by NF- κ B-dependent gene expression, whether or not these effects are from neurons, glia or both remain to be validated by future studies.

Previous studies show that C-DIM12 induced NR4A2-dependent transactivation in pancreatic and bladder cancer cells (Li et al, 2012; Inamoto et al, 2008) and this response was consistently observed in neuronal-like PC12 cells (**Fig. 8A-C**). Additionally, in other work, we have observed C-DIM12 induced NR4A2-dependent transactivation in SY5Y

cells transfected NBRE-Luc and NurRE-Luc constructs (data not shown). C-DIM analogs have strong binding affinity to the ligand binding pockets of the NR4A family member, Nur77 (S-O Lee *et al.*, 2014). X-ray crystal studies of the Nurr1 structure revealed that the classical ligand binding pocket is blocked by several bulky hydrophobic amino acid residues, suggesting that an alternative co-activator domain may allow ligand binding for transcriptional activation (Z Wang *et al.*, 2003; Volakakis *et al.*, 2006). Our computational modeling results predicted substantial greater binding affinity for C-DIM12 at the coactivator site (-73.3 kcal/mol) than to the ligand binding site (-12.2 Kcal/mol) (**Fig 8E, H**). Therefore, C-DIM12 interactions at the coactivator-binding likely modulates transcriptional activity. Nuclear import and export sequences (NLS/NES) mediate Nurr1 shuttling from the nucleus to the cytosol during oxidative stress (García-Yagüe *et al.*, 2013). We demonstrated that C-DIM12 maintains Nurr1 nuclear localization in DA neurons, which was consistently observed with post-lesion intervention as well (**Fig 7A-B**) (De Miranda *et al.* 2014). Total levels of Nurr1 protein from ST were depleted about 60% with MPTP+C.O. treatment and significantly restored to ~80% in C-DIM12 treated animals (**Fig 7C, 7D**). Furthermore, by qPCR analysis of Nurr1 expression we demonstrated C-DIM12 induces Nurr1 by ~3.5-fold times higher than both control and MPTP + C.O. (**Fig 7E**). There was also a ~2-fold induction of related NR4A member, Nur77 as well (**Fig 7F**). This is consistent to previous studies that confirm C-DIM12 has binding affinity to Nur77, albeit to a lesser extent than Nurr1 (S-O Lee *et al.*, 2014).

In conclusion, we demonstrated that C-DIM12 crosses the blood brain barrier, suppresses glial activation, protects against DA neuronal cell body loss, preserves DA terminals, improves neurobehavioral function and decreases NF- κ B regulated

neuroinflammatory gene expression in the MPTPp mouse model of PD by modulating transcriptional activity of Nurr1. Given these findings, we conclude that C-DIM12 is a functional Nurr1 ligand with distinct effects in neurons and glia that could represent a disease-modifying treatment strategy for PD.

4.5 FIGURES

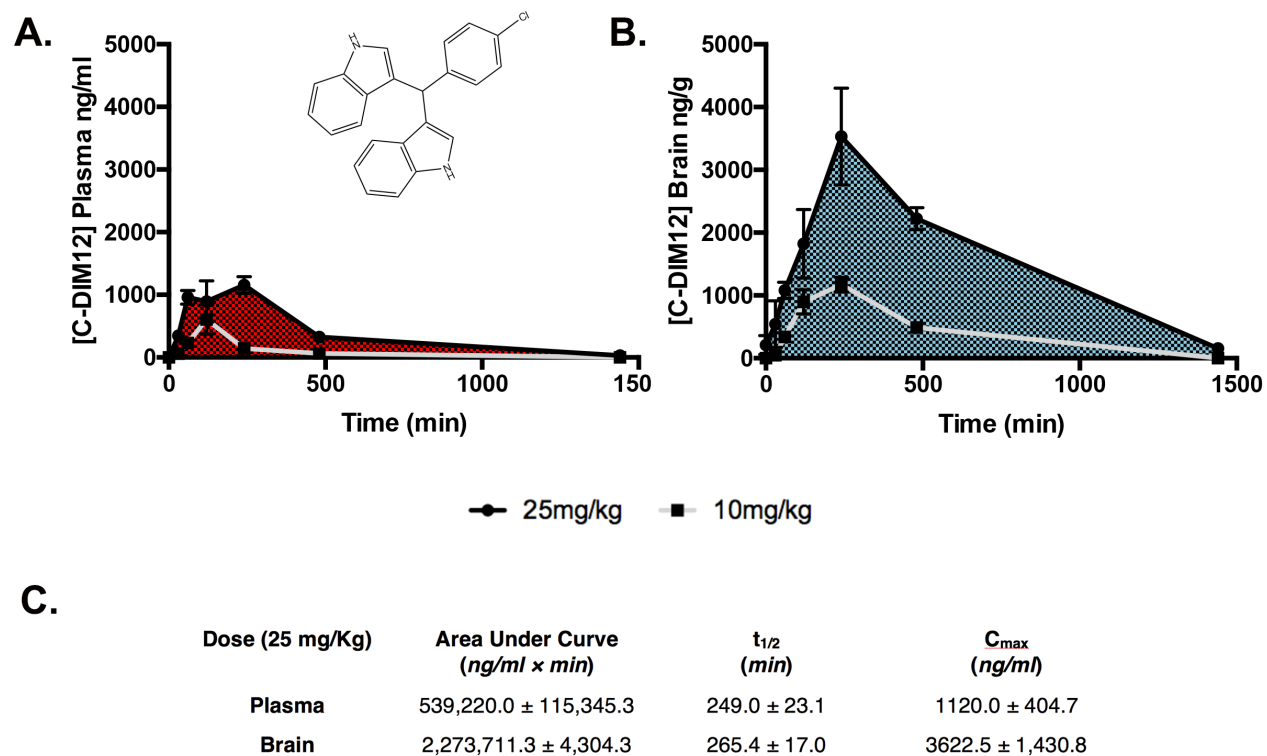


Figure 4.5.1 Pharmacokinetic analysis depicts high concentration of C-DIM12 in brain tissue. Plasma (A) and brain (B) samples were collected from mice at 24, 8, 4, 2, 1, .5 and 0 hours after oral gavage of C-DIM12 (25mg/kg; black line, 10 mg/kg; grey line- De Miranda et al. 2013) and analyzed for C-DIM12 concentration via LC-MS. (C) Chart of AUC, $t_{1/2}$ and C_{max} depict a higher partitioning of C-DIM12 to brain tissue ($n=4$ animals/per time point).

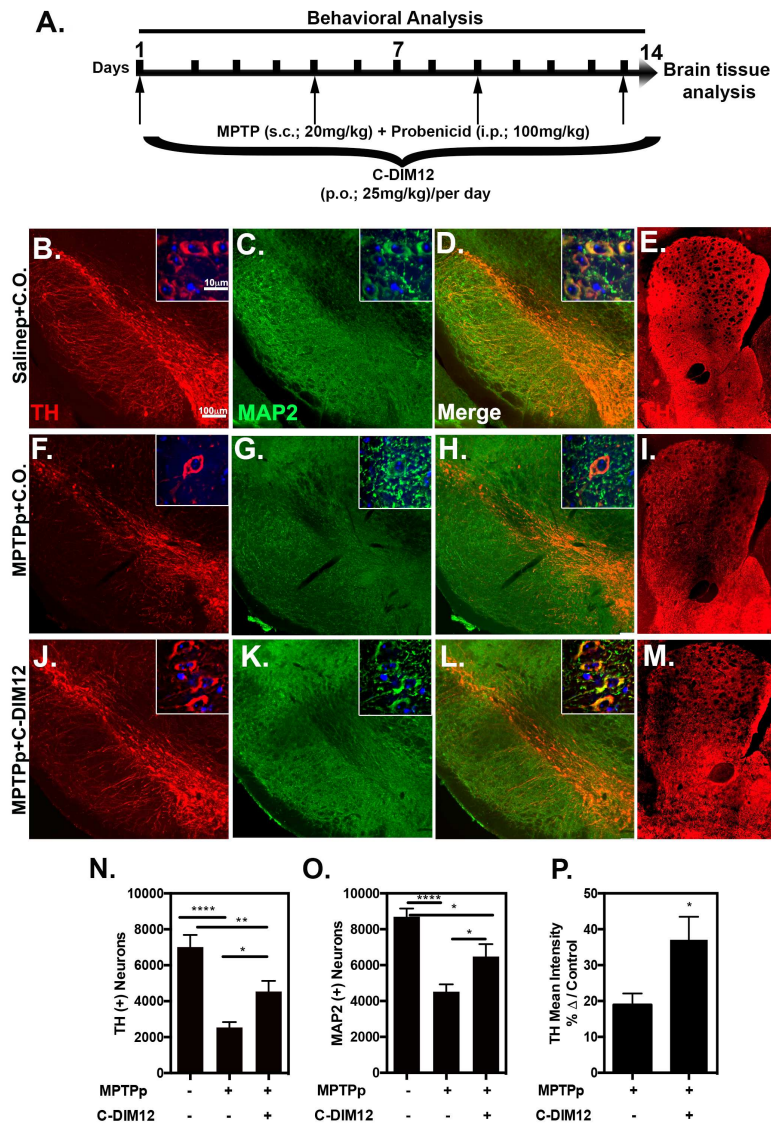


Figure 4.5.2 C-DIM12 protects DA neuron bodies/terminals from MPTP induced degradation. Concurrent dosing schematic with C-DIM12 and MPTPp treatments (A). 10X and 100X objective images of SN/ST tissue immunostained for TH (red) and MAP2 (green) treated with (B-E) Salinep + C.O., (F-I) MPTPp + C.O., and (J-M) MPTPp + C-DIM12. (N) Stereological counts for TH⁺ and (O) MAP2⁺ cells bodies of the SNpc demonstrate significantly more neurons in MPTP +C-DIM12 treated group vs. MPTP+C.O. group. (P) TH immunoreactivity intensity levels also measured significantly more in C-DIM12 treated group (* $P < 0.05$, ** $P < 0.01$, **** $P < 0.0001$, $N=10-12$ animals/per group).

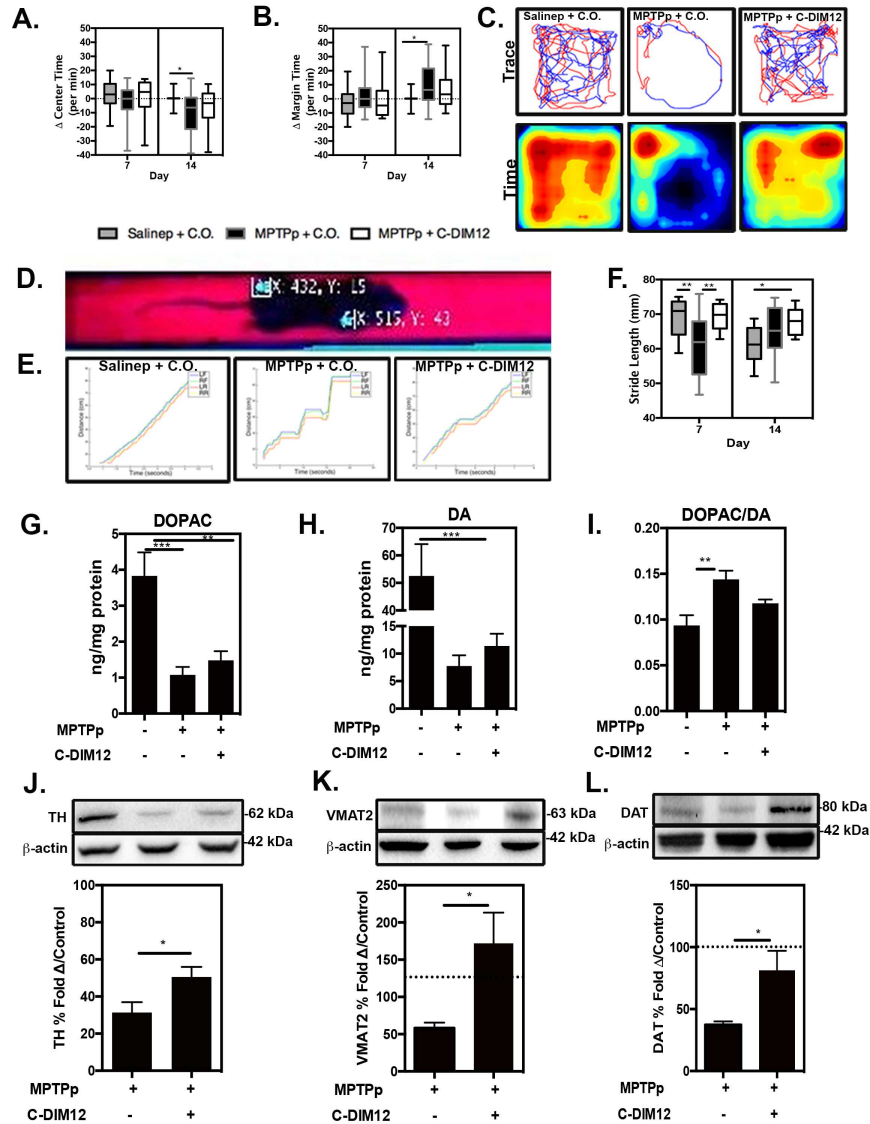


Figure 4.5.3 Neurobehavioral deficits associated with PD are ameliorated and DA proteins are preserved with C-DIM12 treatment. Open-field test (OFT) was conducted on mice at 0, 7 and 14 days during study. (A) Change from day 0/per min OFT center time and (B) margin time was quantitated at day 7 and 14. (C) Trace and pseudo-colored time plots represent OFT mouse movement at day 14. (D) Representative image shows a real-time video gait analysis system used to detect paw coordinates for quantitative measurement. (E) Gait images depict distance vs. time graphs in animals in each group at day 7. (F) Graph displays stride length measured with RT-VGAS at day 7 and day 14. (G) High performance liquid chromatography (HPLC) was used for measurement of DA metabolite, DOPAC, (H) dopamine and (I) ratio of DOPAC/DA from each experimental group. Western blot analysis of striatal protein depicts levels of TH (J), VMAT2 (K), and DAT (L) (* $P < 0.05$, ** $P < 0.01$, **** $P < 0.0001$, $N=10-12$ animals/per group for behavior, $N=6-8$ animals/per group for WB).

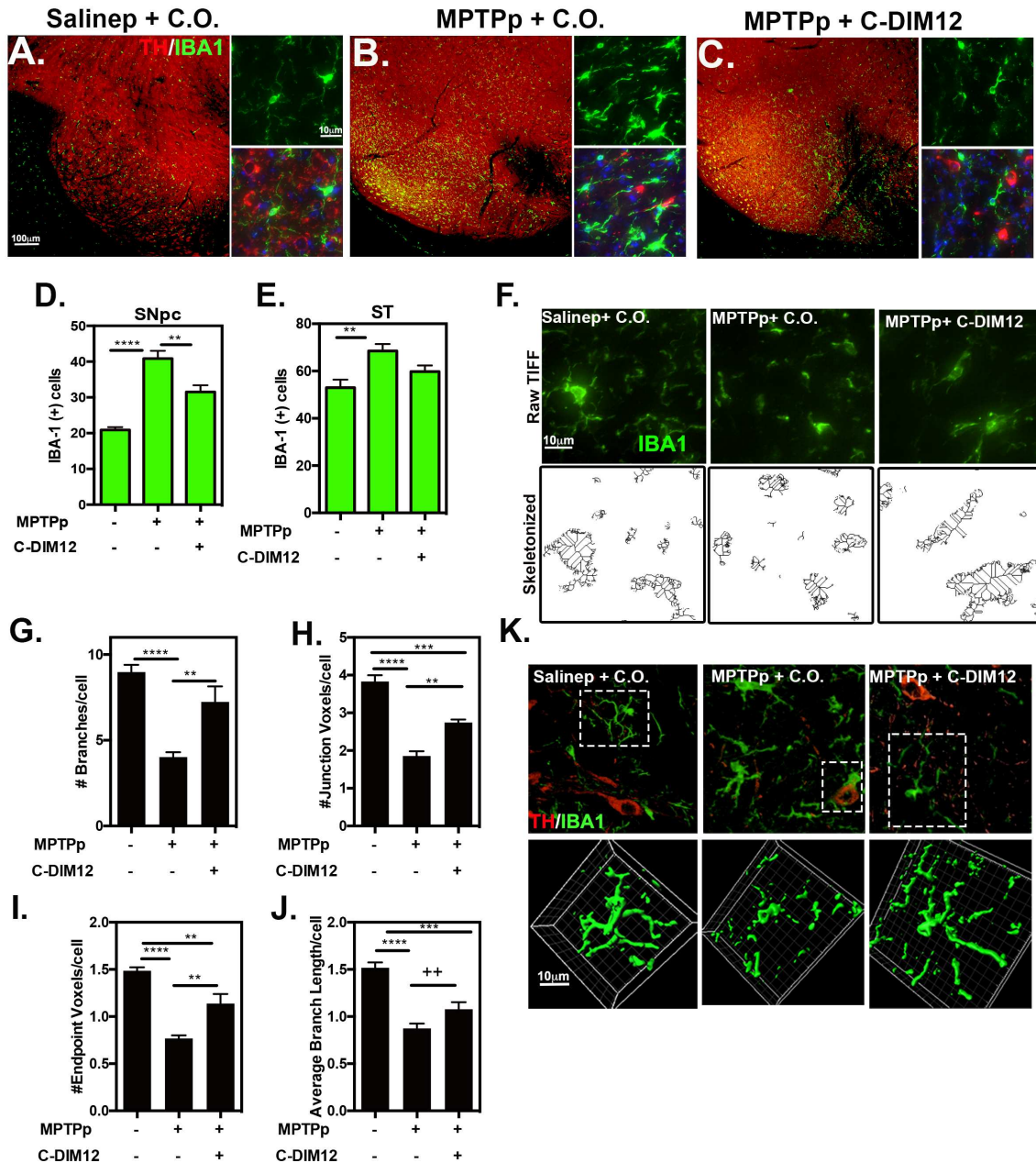


Figure 4.5.4 C-DIM12 suppresses microglia proliferation and maintains a ramified morphological phenotype. 10X and 100X objective representative images of TH (red) and microglia marker, IBA1 (green) in the substantia nigra are depicted for Salinep+C.O. (A), MPTPp+C.O. (B) and MPTPp +C-DIM12 (C). (D) Gliosis counts of the substantia nigra (SNpc) and (E) ST tissue were conducted for amount of IBA⁺ cells. To visualize microglia morphology changes of IBA⁺ cells in the SNpc, (F) multiple 40x-objective images were also transformed in ImageJ for skeletonization and quantitation of microglia (G) branches, (H) junctions, (I) endpoints, and (J) average branch length (***P* < 0.1, **P* < 0.05, ***P* < 0.01, ****P* < 0.001, *****P* < 0.0001; *N*=12 animals/per group for counts, *n*=6 animals/per group for skeletonization). (K) 64x-objective, 3D images of microglia in SNpc were surfaced rendered on channel for IBA1 in each experimental group (boxed cells from top images with IBA1/TH were selected; **See Supplemental Videos 1-4**).

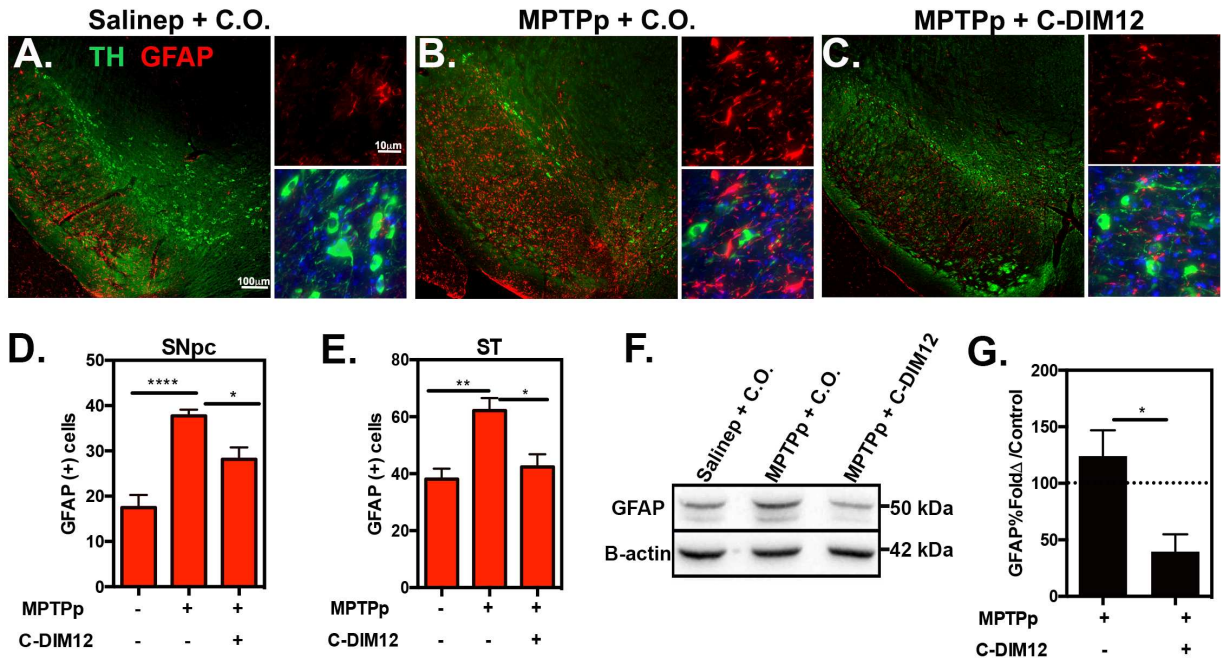


Figure 4.5.5 Astrocyte activation is suppressed by C-DIM12. 10x and 100x, objective images of SN tissue sections isolated from (A) Salinep + C.O., (B) MPTPp + C.O., and (C) MPTPp + C-DIM12 depict TH⁺ neurons (green), GFAP⁺ astrocytes (red). Stereological counts of GFAP⁺ cells in the (D) SNpc and (E) ST demonstrate significantly less astrocyte proliferation in C-DIM12 group. (F) Western blot of striatal protein has significantly less GFAP with C-DIM12 as quantitated in (G) (**P* < 0.05, ***P* < 0.01, *****P* < 0.0001, *N*=6 animals/per group).

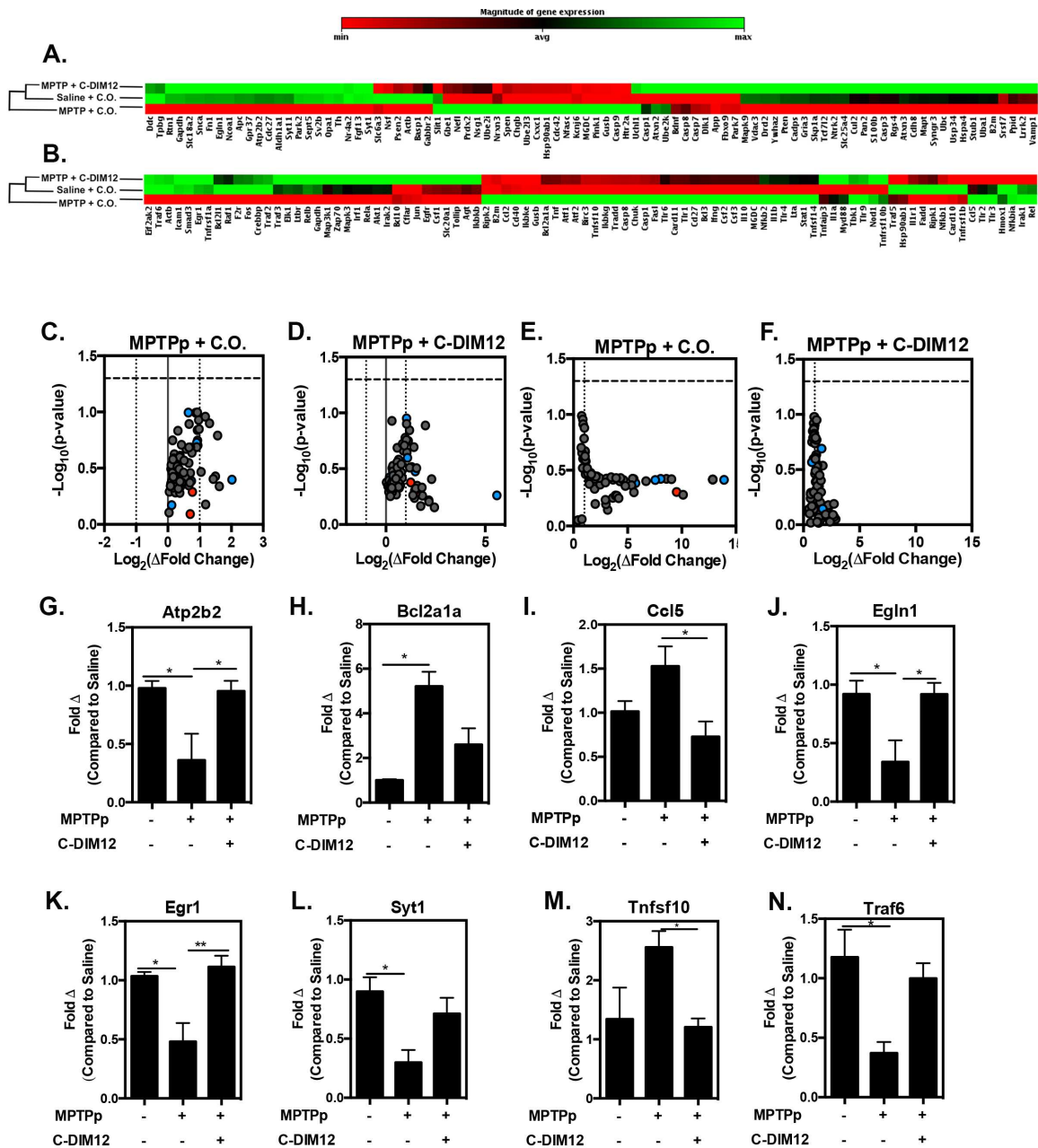


Figure 4.5.6 PD associated/NF- κ B regulated gene expression is preserved in MPTPp + C-DIM12 mice. (A) Ontology dendrogram heat maps of 84 PD associated genes from SNpc RNA depicts a cluster grouping with MPTP+C-DIM12 and Saline treated groups. Notice NR4A2 (Nurr1) is lower in MPTP +C.O. treated group. (B) Heat map of 84 NF- κ B regulated genes analyzed from SNpc RNA. Map depicts a cluster grouping to Saline control levels in MPTP+C-DIM12 treated tissue (red=increase, green=decrease). Volcano plots from PD (C-D) and NF- κ B (E-F) arrays show fold changes for MPTP + C.O. and MPTPp + C-DIM12 groups compared back to Saline controls (red=min, green=max expression). Graphical display for *Atp2b2* (G), *Bcl2a1a* (H), *Ccl5* (I), *Egln1* (J), *Syt1* (G), *Tnfsf10* (M) and *Traf6* (N) depict significant gene fold changes with experimental groups (* $P < 0.05$. ** $P < 0.01$; $N=4-5$ mice/group).

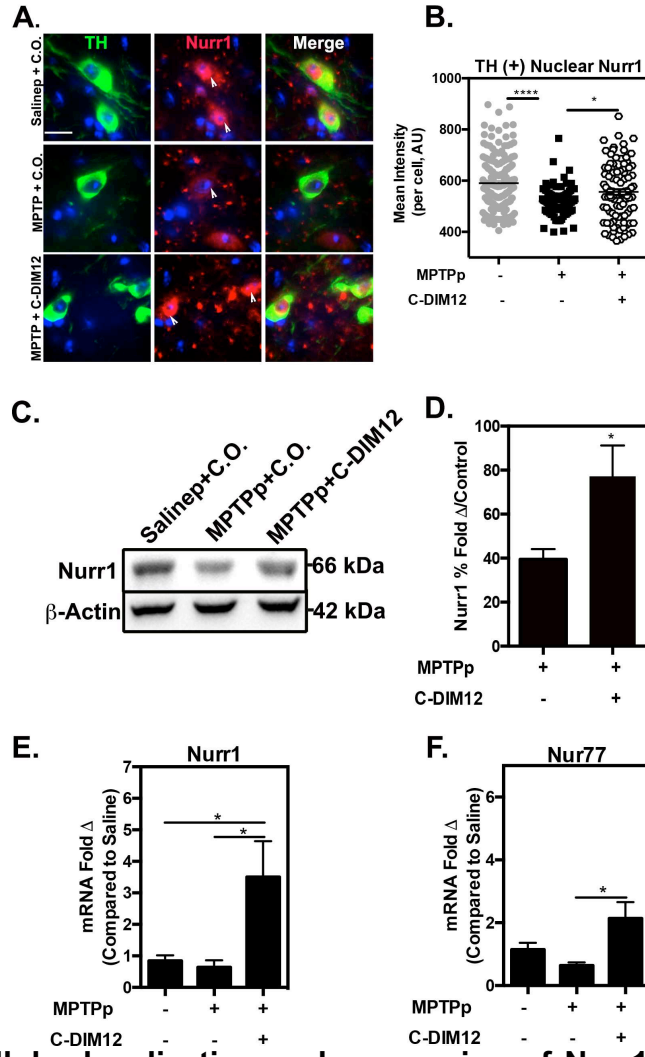


Figure 4.5.7 Subcellular localization and expression of Nurr1 are modified by C-DIM12 treatment *in vivo* (A) 100X objective images of TH⁺ neurons (green) show Nurr1 (red) is sequestered to the nucleus with C-DIM12 treatment, white arrows depict nuclear localization. (B) Mean intensity of TH⁺ nuclear Nurr1 is significantly higher in C-DIM12 group compared to MPTP + C.O. (**P* < 0.05, *****P* < 0.0001; *N* = 4 animals/group). (C) Western blot of Nurr1 protein isolated from ST tissue show C-DIM12 prevents MPTPp-induced protein changes, (D) as illustrated in quantitative measurement of mean optical density (control set to 100%; **P* < 0.05, ***P* < 0.01, ****P* < 0.001, *N* = 6-8 animals/group). qPCR data of mRNA isolated from SNpc for (E) Nurr1 and (F) Nur77 (NR4A1) expression show C-DIM12 induces higher levels of NR4A2 (**P* = 0.05, respectively; *N* = 8 animals/group).

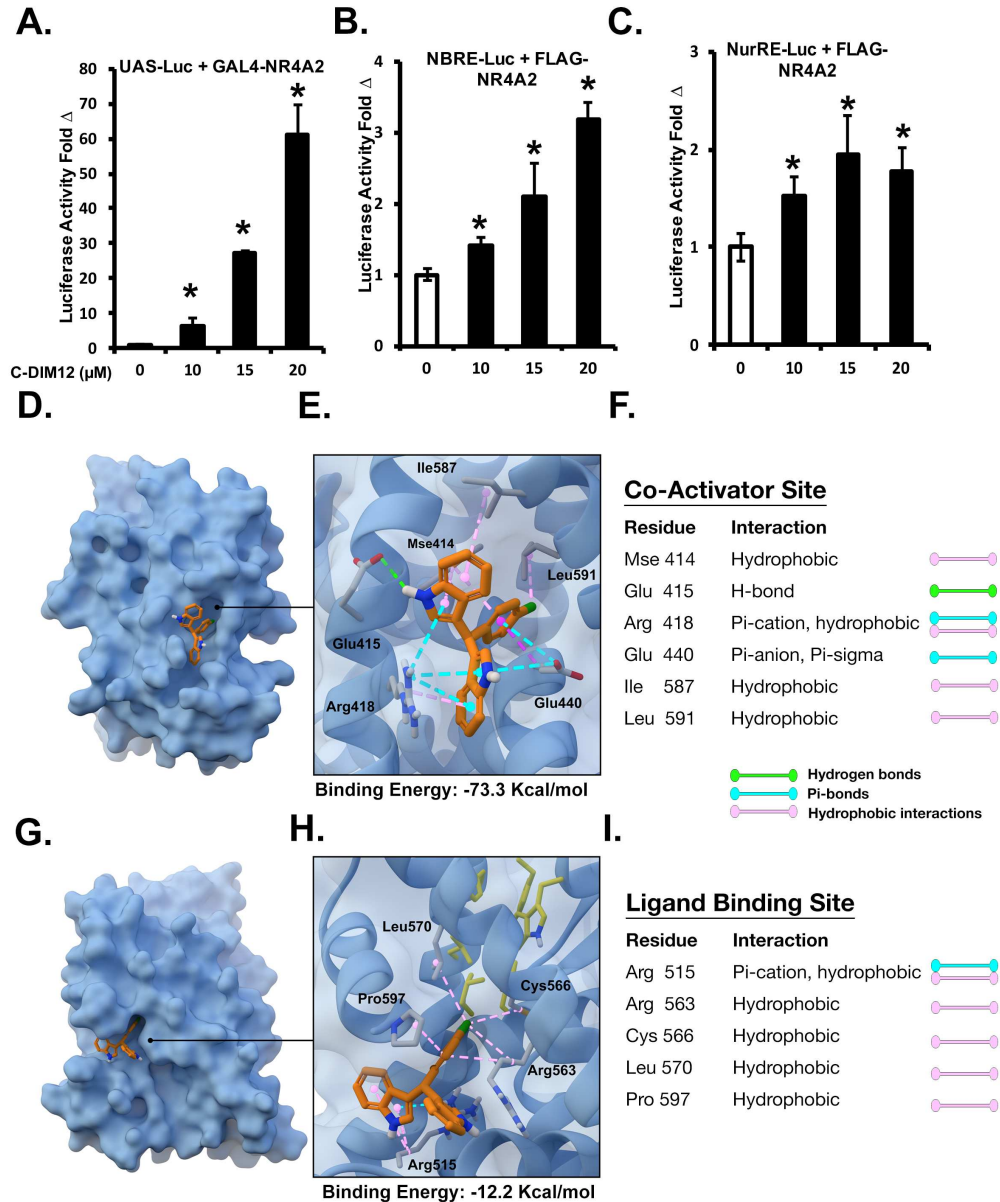


Figure 4.5.8 C-DIM12-dependent transactivation of Nurr1 reporter constructs in neuronal cells and putative binding sites within the ligand binding domain of human NR4A2. Luciferase expression of PC12 cells co-transfected with UAS-Luc + GAL4-Nurr1 (A) NBRE-Luc + FLAG-Nurr1 (B) and NurRE-Luc + FLAG-Nurr1 (C) in the presence of 0-20 μ M C-DIM12 (* $P < 0.05$; $N=3$ /experiment). *In silico* modeling of the Nurr1 ligand binding domain displays putative binding sites for C-DIM12 at the co-activator interface with a calculated binding energy of -73.3 Kcal/mol (D-F) and at the ligand binding pocket with a calculated binding energy of -12.2 Kcal/mol (G-I).

CHAPTER 5

CELLULAR SELECTIVITY OF AAV SEROTYPES FOR GENE DELIVERY IN NEURONS AND ASTROCYTES BY NEONATAL INTRACEREBROVENTRICULAR INJECTION²

5.1 INTRODUCTION

Adeno-associated viruses (AAVs) are the most commonly used vector for gene delivery to central nervous system (CNS). AAVs are small (20nm), non-pathogenic in humans and animals, contain a single-stranded DNA genome and are a member of the *Parvoviridae* family within the *Dependovirus* genus (Kotterman and Schaffer, 2014) (Daya and Berns, 2008). Serology of AAVs is an important functional characteristic for cell specific transduction efficiency within the CNS. AAV2 was the first serotype cloned into a bacterial plasmid and has since been used as a comparison to identify other serotypes. Each serotype has a different CNS transduction capacity and does not cross-react with naturally-occurring human AAV2-neutralizing antibodies (Samulski *et al.*, 1982). Twelve serotypes (AAV1-12) have been tested thoroughly for their ability to transduce specific cell types and tissue and differentiated between capsid protein motifs that bind specific cell surface receptors for cell attachment [4]. For example, AAV1, AAV4, AAV5, AAV7 (sialylated glycoproteins), AAV2/AAV3 (heparin sulfate proteoglycans), AAV9 (galactose) and AAV8 do not have a known primary receptor, although laminin is a potential co-receptor for these viruses (Akache *et al.*, 2006). More recently, a universal receptor,

²Reprinted with permission of PLOS ONE. All rights reserved.

KIAA0319 or AAVR, has been identified that mediates rapid endocytosis after cell binding and attachment for all AAV serotypes (Pillay *et al.*, 2016). AAV hybrid serotypes or pseudo-serotypes have been created by viral engineering, which are constructed with integrated genome containing (cis-acting) inverted terminal repeats (ITR) of AAV2 and capsid genes of other serotypes for increased viral specificity and transduction (Choi *et al.*, 2005). Several studies display AAV serotype transduction differences *in vitro* and *in vivo*; dependent on cell type specificity, cell toxicity, viral delivery method, viral delivery timing, and AAV transgene expression stability over time (RL Klein *et al.*, 1998; Royo *et al.*, 2008; Howard *et al.*, 2008; Chakrabarty *et al.*, 2013; Aschauer, Kreuz, and Rumpel, 2013a). However, some of these studies lack informative, transitional data incorporating both hybrid and wild type serotype differences found in neural cell culture preceding serotype comparisons in mouse brain.

Neonatal intracerebroventricular (ICV) injection is a promising delivery technique for AAVs in mice that is minimally invasive and displays widespread tropism throughout the brain, as opposed to stereotactic injection procedures in adult mice, which are highly invasive and localize only to site of injection. Previous studies reported that when AAV2 is injected directly into the cerebral lateral ventricles at birth, it can circulate through the subarachnoid space, disseminate through the ventricle ependymal cell lining and deliver viral vector throughout the CNS (Passini and Wolfe, 2001). Transgene expression following neonatal ICV injection can persist for at least 12 months, and there are regional differences in tropism amongst different AAV serotypes delivered by this method (J-Y Kim *et al.*, 2013). Because of the reported variability in serotype-dependent regional tropism

amongst different studies, there remain questions as to which serotype is best suited to transduce neurons or astrocytes in specific regions of interest within the CNS by ICV.

In the present study we therefore used multiple AAV serotypes expressing fluorescent GFP reporters to examine regional tropism and efficiency in transducing gene expression in primary neuron and astrocyte cultures and *in vivo*. AAVs were administered by ICV injection into neonatal P0 mice for delivery to the CNS. Tissue was collected at 3 and 6 weeks post-ICV injection to compare AAV serotype stability in multiple regions of the brain. Previous investigations of AAV serotype differences have predominately focused on the localized expression after stereotaxic injection in adult mice for intervention in neurodegenerative disease models. Still, few studies have fully investigated the capacity of multiple ICV delivered AAVs serotypes to penetrate to deep ventral midbrain regions and transduce specific cell types (Chakrabarty *et al.*, 2013; J-Y Kim *et al.*, 2013; McLean *et al.*, 2014). Using immunofluorescence and imaging, we report different patterns of cell specific AAV serotype tropism in cell culture and in multiple regions of mouse brain, including the substantia nigra (SN). Further testing was conducted with glial fibrillary acidic protein (GFAP) promoter-driven AAV using the optimal serotype to exclusively target astrocytes. These studies identified different AAV serotypes that preferentially transduced gene expression in astrocytes or neurons with surprising variability in regional tropism, suggesting several suitable serotypes for achieving gene expression with the desired regional and cellular selectivity.

5.2 MATERIALS AND METHODS

AAV serotypes

The following AAV serotypes tested were acquired from Vector BioLabs; AAV1(Cat# 7002), AAV2/1(Cat# 7071), AAV2/DJ (Cat# 7078), AAV2/DJ8 (Cat# 7118), and AAV2/DJ9 (Cat# 7119) and astrocyte-specific, AAVDJ8-GFAP-mCherry-WPRE. AAV8 and AAV9 were from Virovek. All pseudo-serotypes incorporated ITRs of wildtype AAV2 and mRNA stabilizing woodchuck hepatitis virus posttranscriptional regulator elements (WPRE). AAV2/1 had capsid protein of wildtype AAV1, AAVDJ was a synthetic serotype made from 8 wildtype serotypes, AAVDJ8 was AAVDJ modified to specific residues of AAV8, and AAVDJ9 was modified to specific residues of AAV9. Each pseudo-serotype also had a CMV/Chicken-beta-actin hybrid promoter and eGFP transgene. Wildtype AAV1 had a CMV promoter and an eGFP transgene. All Vector BioLabs serotypes were stored in a PBS/glycerol 5% stock at an initial concentration of 1×10^{13} GC/ml. Serotypes acquired from Virovek had a CMV promoter, a GFP reporter and a modified wildtype capsid. AAV8 was an initial concentration of 2.14×10^{13} GC/ml and AAV9 was at 2.10×10^{13} GC/ml, stored in a PBS/pluronic F-68 0.001% stock, before dilution to working concentration. All serotypes were made in aliquots to minimize freeze/thaw cycles and stored at -80°C .

Use of animals

Timed pregnant female C57BL/6 mice were obtained E16-E19 (Charles River aged 3-4 months). P0 neonatal mice were ICV injected within ~12 hours post birth. Mice were housed in a 12hr-light/dark cycle and temperature-controlled room (maintained $22-24^{\circ}\text{C}$) with access to standard chow and water *ad libitum*. All animal procedures were conducted

in compliance with National Health Institute guidelines and approved by Colorado State University Institutional Animal and Use Committee. Neonatal ICV injections were conducted under heavy cyroanesthesia and adult terminal procedures were performed under isoflurane anesthesia.

***In vitro* AAV transduction experiments and immunostaining**

Primary cortical neurons were isolated from P0 neonatal C57BL/6 mice, as previously described, and then seeded on Poly-D-Lysine (Sigma Cat# P6507-5mg) coated 12-mm coverslips at a density of 5.0×10^4 /well (W Li *et al.*, 2015). For live cell fluorescent plate reading/imaging, neurons were seeded at 5×10^3 /well in 96-well black-walled plates (Thermo Scientific, Waltham MA). Neuronal cultures were allowed to grow for 7 days prior to viral treatments. For mixed glial cell isolations, astrocytes were also isolated from P0 neonatal C57BL/6 mice, as previously described (De Miranda, Popichak, Hammond, Jorgensen, *et al.*, 2015). Mixed glia were seeded on FBS coated 12-mm coverslips at 5.0×10^4 /well 24 hours prior to viral transductions. All AAV-GFP serotypes were diluted to 5×10^{10} GC/ml in Neurobasal Medium (Life Technologies) for primary neurons or serum-free MEM/EBSS (Hyclone) for astrocyte transductions. Native GFP fluorescence signal was monitored at 488nm emission/519nm each day on a Cytation3 Cell Imaging Multi-Mode plate reader (BioTek Instruments, Winooski, VT). DIV 7 cells were washed with phosphate-buffered saline (1X PBS) and replaced growth medium with Fluorobrite DMEM (Life Technologies) for GFP and bright-field 20X objective imaging on plate reader, then fixed with ice cold methanol for 20 min at -20° . For mixed glia transduction experiments with AAVDJ8-GFAP-mCherry, a higher titer of 1.9×10^{11} GC/ml was necessary for successful detection of mCherry expression and cells were fixed at DIV 11.. Both cell

types were immunostained for chicken polyclonal anti-GFP (1:500; AvesLabs Cat# 1020), rabbit polyclonal anti- mitogen associated protein (MAP2) (1:500; Abcam Cat# 32454) for neurons and mouse polyclonal anti-GFAP (1:500; Cell Signaling Cat# 3670S) for astrocytes and anti-mCherry (1:100; Abcam) for AAVDJ8-GFAP-mCherry transduced cultures. Secondary antibodies used were AlexaFluor donkey anti-rabbit 555, goat anti-chicken 488, and donkey anti-mouse 555 (1:500; Life Technologies). All 12mm-coverslips were mounted on glass slides with VectaShield mounting medium containing 4',6-diamidino-2-phenylindole (DAPI; Vector, Burlingame, CA) and stored in 4°C until imaged.

Neonatal Intracerebroventricular injections

ICV injection procedures were closely adapted from several established protocols by Kim et al. 2013 & 2014 and Charkrabarty et al. 2013 (J-Y Kim *et al.*, 2013; 2014). In brief, P0 neonatal pups were induced with hypothermic anesthesia by placement on a cold aluminum plate in ice. Anesthesia was confirmed by neonatal color change from pink to purple, squeezing of paw and cessation of movement before injections. ICV injections were performed using a 10uL Hamilton micro syringe with a 32 G, 0.5", 30° bevel RN needle. Ventricular injection sites were identified by 2/5 distance from lambda suture to eye and 3mm ventral from skin (marked on needle shaft). Working viral solutions were diluted in PBS at 1×10^{10} GC/uL, and injected as a 2uL volume/hemisphere, equivalent 2×10^{10} GC/hemisphere. Injected pups were placed on warming pad and regained movement before returned to dam cage. Juvenile weanlings were terminated at 3 weeks for brain collection or weaned/aged for an additional 3 weeks for 6-week post ICV injection.

Histological Preparation of Tissue and Immunostaining

AAV injected mice were terminated at 3/6 weeks under deep isoflurane anesthesia and decapitated for rapid brain dissection. Dissected brains were stored in 3% paraformaldehyde overnight and then stored in cacodylate-PBS containing 15-30% sucrose at 4°C until processed for cryo-sectioning. Brains were then frozen in OCT and sectioned at 40µm thickness (coronal/sagittal) on microtome. Free-floating brain regions of interest (ROI) were mounted on glass slides and imaged for AAV-GFP or stored in cryoprotectant at -20°C until immunostaining. Immunofluorescent tissue staining was conducted as previously described by Miller et al. (Miller *et al.*, 2011), with the addition of antigen-retrieval by incubating tissue sections in 0.01 M sodium citrate buffer (pH 8.45) for 20 min prior to blocking. Primary antibodies diluted in 0.1% triton-X containing tris-base-saline (TBS) are rabbit polyclonal anti-MAP2 (1:500; Abcam Cat# 32454), rabbit polyclonal anti-S100β (1:100; Abcam Cat# ab41548), chicken polyclonal anti-GFP (1:500; AvesLabs Cat# 1020), and rabbit polyclonal anti-tyrosine hydroxylase (1:500; Millipore Cat#: AB152). Sections were stained for DAPI (Sigma) and mounted on glass coverslips in VectaShield mounting medium and stored at 4°C until imaging.

CLARITY tissue-transmutation

Passive clarification was conducted similarly to protocol established by Tomer et al. 2014 (Tomer *et al.*, 2014). In brief, brains were embedded in hydrogel (4% acrylamide/0.05% Bis-acrylamide) and sectioned at 400µm thickness on a cryo-microtome. Sections were placed in clearing solution (4% sodium dodecyl sulfate/200mM boric acid, pH 8.5) for 7 days at 37 °C and 35 rpm. Sections of clarified substantia nigra region were then selected for immunostaining. Clearing solution was removed by washing 3 times with TBS and

then sections were incubated for immunostaining with chicken polyclonal anti-tyrosine hydroxylase (1:200; Abcam Cat# ab76442), rabbit polyclonal anti-GFAP (1:200; DAKO Cat# Z0334), anti-GFP (1:200; AvesLabs) or anti-mCherry (1:200; Abcam Cat# ab167453). Antibodies were diluted in TBS at 37 °C and incubated with tissue sections with an orbital shaker at 35 rpm overnight and then at 4°C for 1 day afterward. Multiple washes were performed over 2 days at 37 °C (with orbital shaking at 35 rpm) and then cleared sections were placed in TBS containing goat anti-chicken AlexaFluor 647 (1:200; Life Technologies) and donkey anti-rabbit AlexaFluor 555 (1:200; Life Technologies) at 37 °C overnight with orbital shaking (35 rpm). The next day, sections were washed several times with TBS and stored at 4°C until imaged.

Imaging and Cell Counting

Images of transduced primary cells and all quantitated AAV infected brain regions were acquired using a 20X air objective with a Zeiss Axiovert 200M inverted fluorescent microscope equipped and a Hamamatsu ORCA-ER-cooled charge coupled device camera (Hamamatsu Photo-nics, Hamamatsu City, Japan). For IF quantitation, multiple random, z-stack images of approximately 30 µm disector height for both hemispheres of all brain regions (*in vivo* quantitation) or a single 2D images (for *in vitro* quantitation) were acquired per coverslip/brain region and counted total %GFP cell/image field using Slidebook software (version 5.5, Intelligent Imaging Innovations, Denver CO). A background subtraction was performed for all IF *in vivo* images, prior to quantitation. Representative high-magnification images were acquired with a Zeiss Plan-Apochromat 100X oil objective lens. Representative 10X objective montage images of ROI were acquired with a BX51 microscope (Olympus, Center Valley, PA, USA) equipped with a Hamamatsu

ORCA-Flash4.0 digital CMOS camera, ProScan III stage controller (Prior, Rockland, MA USA) and CellSens Dimension software (version 1.12, Olympus, Center Valley, PA, USA). All bright field images of mock-injected brains were acquired with Olympus SZX12 stereo-dissecting microscope. For enhanced CLARITY fluorescence imaging of AAVDJ8-GFP, 40X oil objective montage images were acquired using a Fluoview 1200 scanning-laser confocal microscope to penetrate ~80µm thickness of tissue (Olympus, Center Valley, PA USA). CLARITY fluorescent imaging of AAVDJ8-GFAP-mCherry was conducted on a Zeiss LSM 510 Laser-scanning confocal microscope to penetrate and capture ~180µm thickness of tissue. Both sets of CLARITY images were 3D-rendered in ImageJ analysis software (Schneider *et al.*, 2012). Representative images of whole brain fluorescence were acquired with ChemiDoc MP imaging system (BioRad). Uninjected controls were imaged with each serotype for comparison of background fluorescence (**Supplemental Fig. 3**).

Statistical Analysis

All data are expressed as mean ± SEM. Grouped analyses was performed using a Two-way ANOVA with Sidak's post hoc test to compare biological replicate means between groups. For semi-quantitative representation of GFP⁺ cells/brain region as depicted in **Table 1**, cell counts were divided into quartiles as follows; +++≤55.5 GFP⁺ cells/image field, ++≤31.3 GFP⁺ cells/image field, +≤11.6 GFP⁺ cells/image field and -≤5.8 GFP⁺ cells/image field. Statistical significance was identified as **p* <0.05, ***p* <0.01, ****p* <0.001, *****p* <0.0001. All statistical analyses were conducted using Prism (version 6.0; Graph Pad Software, San Diego, CA).

5.3 RESULTS

Comparison of multiple AAV serotypes in primary astrocyte and neuronal cultures.

Several wildtype and hybrid serotypes carrying eGFP or GFP fluorescent reporters were compared for transduction efficiencies in astrocytes. Mixed glia cultures were transduced for 1 week with different serotypes and fixed for double immunofluorescent labeling for the astrocyte marker, GFAP (red) and GFP (green) (**Fig. 1A, C, E, G, I, K, M**). Astrocyte (GFP⁺GFAP⁺/GFAP) transduction efficiencies (Mean \pm SEM; $n=3-7$ /serotype) were as follows: 4.785% \pm 2.635 for AAV1, ~71% \pm 7.79 for AAV2/1, 33.17% \pm 9.169 for AAVDJ, 58.49% \pm 11.43 for AAVDJ8, 46.64% \pm 10.31 for AAV8, 36.77% \pm 4.749 for AAVDJ9, and 41.88% \pm 11.49 for AAV9 (**Fig. 1O**). Similarly, primary cortical cultures were transduced for 1 week and fixed for double immunofluorescent labeling for the neuronal marker, MAP2 (red) and GFP (green) (**Fig. 1B, D, F, H, J, L, N**). Neuron (GFP⁺MAP2⁺/MAP2⁺; $n=6-10$ /serotype) transduction efficiencies were quantitated as follows: 40.5% \pm 11.9% for AAV1, 63.5 \pm 5.4% for AAV2/1, 49.1 \pm 5.0% for AAVDJ, 39.2 \pm 5.7% for AAVDJ8, 21.4 \pm 6.6% for AAV8, 49.6 \pm 7.1% for AAVDJ9, 49.2 \pm 8.7% for AAV9 (**Fig. 1P**). AAV-GFP fluorescence intensity was also monitored in neuronal cultures once per day for 1 week via live cell imaging using a fluorescence microtiter plate reader. AAV-GFP expression was noticeable at approximately 3 days post-infection and increased every day *in vitro* (DIV). AAV2/1 displayed a significantly higher fold-change in fluorescence intensity compared to all other serotypes at 6 DIV (1.733 \pm 0.117) and 7 DIV (1.988 \pm 0.161) ($n=6$ /serotype/time point; * $p<0.05$, *** $p<0.001$) (**Fig 1Q**).

Intracerebroventricular injection of AAV constructs

To administer several selected AAV serotypes to the murine CNS, ICV injections were conducted on P0 neonatal mice (**Figure 2**). Lateral ventricles were targeted for injection on both hemispheres as depicted in the schematic in **Fig. 2A**. Successful injection into ventricle space was confirmed by mock injection of trypan blue/PBS solution administered to neonatal P0 mouse brain for visualization of injection distribution and imaged on bright field stereo dissecting microscope, arrowheads indicate injection sites (**Fig. 2B-C**). Mock injected brains were incised along coronal and sagittal planes to visualize sites of viral solution spread from the lateral ventricles (LV), third (3V), mesencephalic aqueduct (MA) and fourth ventricle (4V), arrowheads indicate ventricular spaces (**Fig. 2D, Supplemental 1A-C**). For *in vivo* AAV serotype characterizations, AAV2/1, AAVDJ8 and AAV9 were selected based on the capacity to efficiently transduce primary neural cultures and the noticeable distribution differences of other serotypes by ICV injection (**Figure 1, Supplemental Figure 4B-F**). Basic plasmid (pAAV) maps of each serotype are illustrated in **Figure 2E**. To monitor AAV tropism throughout the CNS, whole brains were ICV injected with AAV2/1 (**Fig. 2F**), AAVDJ8 (**Fig. 2G**) and AAV9 (**Fig. 2H**) and dissected 3 weeks post-injection or imaging of intrinsic GFP expression. Lateral views of each whole brain are shown in the top image in pseudo color (**Fig 2F-H**). Medial intrinsic fluorescence is depicted in representative images of sagittal cross sections (bottom), along with serial coronal cross sections rostral to caudal on right of each panel, depicting penetrance of each AAV serotype throughout the CNS (**Fig 2F-H**).

Quantitation of AAV2/1-GFP tropism at 3 and 6 weeks post-injection

To determine degree of AAV2/1-GFP tropism in neurons and astrocytes from multiple brain regions at 3 and 6 weeks post ICV injections, anatomical regions including the olfactory bulb, striatum, motor cortex, hippocampus and cerebellum were immunostained for anti-NeuN (red, neuronal marker) and S100 β (purple, astrocytic marker) at 6 weeks post ICV (**Fig 3A-E**). Mitral cells of the granular layer were primarily transduced, with no observed astrocytes in the olfactory bulb (**Fig 3A**). AAV2/1 had modest penetration from ventricular space to striatal neurons, without any GFP⁺ astrocytes observed in the caudate putamen (**Fig 3B**). Most GFP⁺ cells in the primary motor cortex were in Layer 6a-6b, and fewer GFP⁺ pyramidal neurons of cortical layers 5 and 2/3 (**Fig 3C**). Pyramidal layer neurons of CA1 hippocampus heavily expressed GFP, as well as some infected neurons in the molecular layer of the dentate gyrus (**Fig 3D**). Central lobules of the cerebellum had GFP⁺ Purkinje fiber neurons, no astrocytes were observed. Quantitative measurement of AAV2/1-GFP⁺ cells quantitated for each region/time point at 3 and 6 weeks are as follows: 47.5 \pm 11.7 and 37.7 \pm 17.5 in the olfactory bulb; 9.9 \pm 4.1 and 6.9 \pm 1.5 in the striatum; 38.2 \pm 10.3 and 20.7 \pm 6.7 in the cortex; 55.467 \pm 18.584 and 53.167 \pm 17.873 in the hippocampus; 21.8 \pm 12.3 and 2.9 \pm 1.6 in the cerebellum ($n=3$ /Time point) (**Fig 3F**).

Quantitation of AAVDJ8-GFP tropism 3 and 6 weeks post injection

The tropism of AAVDJ8-GFP in multiple brain regions at 3 and 6 weeks post ICV injections was also monitored in the olfactory bulb, striatum, motor cortex, hippocampus and cerebellum (**Fig 4A-E**). At 6 weeks post-ICV mitral layers of the olfactory bulb were heavily infected, including some observed AAVDJ8-GFP⁺ astrocytes (**Fig 4A**). Striatal

neurons and astrocytes of the caudate putamen were primarily infected in the dorsal region of the striatum (**Fig 4B**). High AAVDJ8-GFP infection was observed in all layers of the primary motor cortex, with robust signal in pyramidal neurons of layer 5 and astrocytes of multiform layer 6 (**Fig 4C**). AAVDJ8-GFP⁺ pyramidal neurons of CA1 were observed in the pyramidal layer and infected astrocytes were observed in the dorsal hippocampal layer and stratum oriens (**Fig 4D**). Similar to AAV2/1, central lobules of the cerebellum GFP⁺ Purkinje fiber neurons were transduced but no GFP⁺ astrocytes were observed (**Fig 4E**). AAVDJ8-GFP⁺ cells quantitated for each region/time point at 3 and 6 weeks are as follows: 24.7±6.3 and 29.0±2.8 in olfactory bulb; 10.9±1.6 and 12.0±2.1 in the striatum; 51.7±15.5 and 38.3±4.7 in the cortex; 47.1±4.6 and 36.7±3.4 in the hippocampus; 3.78±0.6 and 5.8±1.1 in the cerebellum (n=3/Time point) (**Fig 4F**).

Quantitation of AAV9-GFP tropism 3 and 6 weeks post injection

AAV9-GFP tropism was similarly monitored at 3 and 6 weeks post ICV injection. The olfactory bulb displayed comparable tropism to AAV2/1 with mainly infectivity in the mitral cells of the granular layer and no observed GFP⁺ astrocytes (**Fig 5A**). Minimum AAV9-GFP infection was present in the striatum, although infected neurons and astrocytes were identified within the caudate putamen region (**Fig 5B**). Both cell types were infected in the primary motor cortex, primarily neurons of layer 5 and astrocytes of layers 6a-b (**Fig 5C**). Neurons and astrocytes were minimally infected within the pyramidal layer of CA1 hippocampal region, and AAV9-GFP was noticeably expressed within the fiber tracts of the dentate gyrus (**Fig 5D**). Similar to AAV2/1 and AAVDJ8, Purkinje fiber neurons within the central lobules of the cerebellum were primarily infected, and no AAV9-GFP (+) astrocytes observed (**Fig 5E**). Transduction efficiencies of AAV9-

GFP⁺ cells quantitated for each region/time point at 3 and 6 weeks are as follows: 9.6±4.2 and 5.3±1.5 in the olfactory bulb; 8.4±3.0 and 1.7±0.8 in the striatum; 39.1±11.1 and 6.4±3.3 in the cortex; 12.3±8.2 and 2.4±0.8 in the hippocampus; 11.3±2.7 and 5.9±2.8 in the cerebellum (***p*< 0.001; *n*=3/Time point) (**Fig 5F**).

Analysis of AAV serotype-specific variation within the substantia nigra.

For further analysis/quantitation of the ventral midbrain region, specifically the substantia nigra (SN) was examined. Tissue sections were immunostained for dopamine neuron marker, tyrosine hydroxylase (TH), at 3 and 6 weeks post-ICV injection and quantitated for number of GFP⁺ cells. Representative IF images of AAV2/1, AAVDJ8 and AAV9 6 week SN tissue immunostained for dopamine neuron marker, tyrosine hydroxylase (TH) is depicted in **Figure 6A-C**. Transduced GFP⁺ cells quantitated in the SNpc at 3 and 6 weeks are as follows: 2.2±14.3 and 0.5±0.16 for AAV2/1; 8.0± 2.6 and 13.8±2.1 for AAVDJ8; 15.1±5.3 and 5.8±1.8 for AAV9 (**p*<0.05, *n*=3/serotype/time point) (**Fig 6D**). Number of dopaminergic neurons transduced/per image field in the SN *pars compacta* (SNpc) at 6-weeks were measured by counting GFP⁺/TH⁺ co-localizing cells (**Fig 6E**). Transduction efficiency of astrocytes was also quantitated by number of GFP⁺/S100β⁺ co-localizing cells. AAVDJ8 transduction efficiency measured 56.4±7.5% S100β⁺/per image field cells and 14.9±7.6% and TH⁺ cells/per image field. AAV9 transduced 22.3±1.0% S100β⁺ cells/per field and 45.5±2.8% TH⁺ cells/per image field (**p*<0.05, *n*=3/serotype) (**Fig 6E-G**). Pearson's co-localization coefficient was also calculated for both cell markers as follows: 0.57±0.06 (GFP⁺/S100β⁺) and 0.46±0.04 (GFP⁺/TH⁺) for AAV9; 0.48±0.06 (GFP⁺/S100β⁺) and 0.54±0.05 (GFP⁺/TH⁺) for AAVDJ8 (25-42 GFP⁺ cells/over *n*=3 animals/serotype; **Supplemental Fig. 2A**. Mean intensity of

GFP fluorescence was also measured for both cell types as accordingly: 295.1 ± 75.5 AU/per S100B⁺ cells and 309.6 ± 65.8 AU/per TH⁺ cells for AAV9; 1207.0 ± 142.2 AU/per S100B⁺ cells and 1157.0 ± 105.9 AU/per TH⁺ cells for AAVDJ8 (25-42 GFP⁺ cells/over $n=3$ animals/serotype; $p < 0.0001^{****}$; **Supplemental Fig 2B-C**). CLARITY tissue transmutation was performed on SN tissue to visualize AAVDJ8 transduction in 3D volumetric space. Clarified tissue was co-immunostained for TH (cyan), GFAP (red) and GFP (green), with expression of GFP primarily confined to astrocytes, noted by co-localization of red and green fluorescence (yellow) (**Fig 6H, Supplemental Video 1**).

AAVDJ8-GFAP-mCherry specifically targets astrocytes of SNpc

After determining the suitability of AAVDJ8 to transduce astrocytes within the SNpc, we used this serotype to express red fluorescent mCherry under the control of a truncated version of the astrocyte-specific *gfap* promoter (0.7kb) that is active and can be efficiently cloned into AAV (**Fig. 7A**). Strong expression of AAVDJ8-GFAP-mCherry was observed in primary cortical astrocyte cultures at $83.2\% \pm 6.5$ mCherry⁺/GFAP⁺ as depicted in representative images in **Fig. 7B**. AAVDJ8-GFAP-mCherry was also tested *in vivo* by ICV to observe cell-specificity and tropism throughout the brain. By 3 weeks post-injection, high levels of mCherry expression were detected within cortical, hippocampal, thalamic and midbrain areas, as depicted in whole brain images of sagittal cross sections (**Fig. 7C**). To determine if there was similar penetrance to the SN as AAVDJ8-eGFP, we imaged immunostained SN tissue for TH, S100 β and mCherry, shown in the representative images in **Figure 7D**. Images of tissue at 3 weeks post-injection were quantitated for the number of transduced astrocytes within the SN, indicating 80.3 ± 6.3 mCherry⁺/S100 β ⁺ cells/image field. No TH⁺ neurons were found to express mCherry.

Mice injected with AAVDJ8-GFAP-mCherry were also aged for 6-weeks to determine the stability of expression with this vector. No significant difference was observed between time points; mCherry⁺ cells/image field was quantitated at 7.2 ± 2.3 and 8.8 ± 1.9 at 3 and 6 weeks respectively ($n=3$ /time point; **Fig. 7E**). GFAP⁺-mCherry⁺ co-localization within the vicinity of dopaminergic neurons is visualized similar to AAVDJ8-GFP by a 3D volumetric view of the clarified SNpc tissue at ~4.5 times thicker (180 μ m) than typical tissue sections cut for cell quantitation (**Fig. 7F**; **Supplemental Video 2**).

5.4 DISCUSSION AND CONCLUSIONS

AAV vectors are valuable tools for transduction of both mitotic and post-mitotic cells of the CNS. The high levels of tropism in multiple brain regions permit expression of a diverse array of transgenes suitable for mechanistic investigation of basic biological function as well as neurological disease. AAV serotype transduction differences have been highly studied for primary cell culture and for gene expression *in vivo*. However, there are few studies that provide a systematic approach for selection of AAV serotypes to achieve both *in vitro* and *in vivo* gene expression in murine neurons and astrocytes in a region-specific fashion. By use of multiple different AAV-GFP serotypes with CMV/CAG promoters, we demonstrate differences in infectivity and gene expression in primary astrocytes and neurons, as well as tropism in multiple regions of the brain, stability of AAV-GFP expression between 3-6 weeks post ICV injection and expression of AAV-GFP in ventral midbrain areas. In addition, we identified an AAV serotype to transduce astrocytes within the SNpc through evaluation of AAVDJ8-GFAP-mCherry.

Serotype transduction differences have been previously reported in rat primary cortical neuronal cultures utilizing naturally occurring serotypes and engineered capsids.

Howard et al. found AAV1-CMV-GFP to have the highest expression of GFP compared to other naturally occurring serotypes in neuronal cultures (Howard *et al.*, 2008; Royo *et al.*, 2008). Accordingly, we screened both the naturally occurring AAV1-CMV-GFP serotype in comparison to engineered hybrid serotypes AAV2/1-CAG-eGFP, AAVDJ-CAG-eGFP, AAV8-CMV-GFP, AAVDJ8-CAG-eGFP, AAV9-CMV-GFP and AAVDJ9-CAG-eGFP to determine transduction efficiency in both MAP2⁺ and GFAP⁺ cells in culture. AAV2/1 transduced the most MAP2⁺ neurons and GFAP⁺ astrocytes in culture based on immunostaining. Additionally, according to daily measurements of GFP in cultured neurons, AAV2/1 was the most rapid and highest expressing serotype by DIV 7. Hence, AAV2/1 was the most efficient for transducing cells *in vitro* amongst the serotypes tested (**Fig. 1**). AAV2/1 has been utilized to target neurons for anti-inflammatory effects of dominant-negative chemokine CCL2 mutant, interleukin-10 (IL-10) in mouse models of Alzheimer's Disease (AD) and brain-derived neurotrophic factor (BDNF) in rat models of Huntington's Disease (Sadasivan *et al.*, 2017) (Kiyota *et al.*, 2012) (Connor *et al.*, 2016). High transduction efficiency has been reported in regions of the basal ganglia in rat and non-human primate animal models by stereotaxic injection using AAV2/1 (McFarland *et al.*, 2009) (Burger *et al.*, 2004; Dodiya *et al.*, 2009). In comparison to AAV1 sagittal cross-sections, the patterns of transgene expression were drastically different with ICV delivery. AAV1 transduction was limited to the ependymal cells of the choroid plexus, whereas AAV2/1-GFP expression was observed throughout the brain (**Supplementary Fig. 4C, Fig. 2C**). Restriction of AAV1 to the ventricular epithelia when delivered via ICV is consistent with studies by JY Kim et al. 2013 and further supports our findings (J-Y Kim *et al.*, 2013). These data suggest the ITR *cis*-acting elements of AAV2 and CAG promoter

within pseudotype AAV2/1 are crucial for transduction efficiency in culture and penetration from ventricle to parenchymal space. With these findings, we selected AAV2/1 for further quantitative analysis in multiple brain regions.

AAVDJ8 displayed promising results in glial cultures, comparable to AAV2/1 (**Fig. 10**). Wide distribution and higher levels of GFP expression were noticeable throughout the brain compared to AAV8 (**Fig. 2D, Supplemental Fig. 4E**). It was previously demonstrated that the AAVDJ8 pseudo-serotype produces ~10-fold higher titers than AAV2/1 and more efficiently drives expression of red fluorescent protein (RFP) in neurons of the rat amygdala (Holehonnur *et al.*, 2014). Prior studies have also indicated that AAV2/8 is an effective vector for targeting neurons of the nigrostriatal system in neurodegenerative studies when administered via stereotaxic injection directly to the substantia nigra in rats (McFarland *et al.*, 2009; 2014). Also, AAV8-based vectors have shown selective expression in astrocytes of the spinal cord, hippocampus, striatum and substantia nigra of adult rats when used with human GFAP promoter to drive transgene expression (Lawlor *et al.*, 2009; K Li *et al.*, 2014). Our findings with AAVDJ8-CAG-eGFP are consistent with these studies and support the use of the AAVDJ8 serotype to target neurons and astrocytes of specific brain regions. Furthermore, AAVDJ8 was a suitable serotype for GFAP-mCherry design to restrict transgene expression in astrocytes.

AAV9 was chosen for further investigation based initially on the ability to transduce neurons *in vitro* and from reports that it can target multiple cell types *in vivo* (Foust *et al.*, 2008; Gray *et al.*, 2011; Aschauer, Kreuz, and Rumpel, 2013a; McLean *et al.*, 2014). AAV9 and AAVDJ9 had the same efficiency in primary neuronal cultures but AAV9 transduced 5% more astrocyte than AAVDJ9 in culture (**Fig. 1**). AAVDJ9 did depict a high

level and wide distribution of transgene expression throughout most brain regions evaluated, yet had lower levels of penetrance to the ventral midbrain regions when compared to AAV9 (**Supplemental Fig. 4F, Supplemental Fig. 5A-B**). In previous studies, AAV9 has been used to target hippocampal neurons when delivered via stereotaxic injection in mice (Aschauer, Kreuz, and Rumpel, 2013b). However, it was also reported that AAV9 crosses the blood brain barrier when delivered intravascularly and targets neurons in neonatal mice but then expresses in astrocytes in adult mice (Foust *et al.*, 2008). In contrast, Gray *et al.* asserted that AAV9 preferentially targets neurons in adult mice when utilizing the same delivery method and promoter/GFP reporter (Gray *et al.*, 2011). Interestingly, AAV9 has been used to target TH⁺ neurons of the SNpc under control of the human synapsin (hSYN1) promoter to drive GFP expression after neonatal delivery via ICV (McLean *et al.*, 2014). Based on these findings and our data, we selected AAV9 for further quantitative analysis in multiple brain regions.

Since initial ICV studies, this method has been tested and optimized for timing of injection and serotype comparisons (J-Y Kim *et al.*, 2013; 2014). It was found that when injecting at different time points (0-72hrs), AAV2/1 had broadest distribution throughout the brain at P0, whereas AAV2/8 and AAV2/9 transduced independently of the age at which they were injected (Chakrabarty *et al.*, 2013). For the most efficient viral dissemination and consistency, we administered all AAV serotypes at P0. At 3-weeks post injection, AAV2/1 transduced the most cells of the olfactory bulb, hippocampus and cerebellum (**Table 1**). AAVDJ8-GFP⁺ cells were most prevalent in the striatum and cortex; and AAV9 transduced the most cells of the substantia nigra (**Fig. 3F-5F, Table 1**). Based on previous studies, ICV-delivered AAVs have been proven to be stable for up to 1-year

post injection(Passini *et al.*, 2003; J-Y Kim *et al.*, 2013). Interestingly, we noticed AAV-GFP expression decreased in many of the regions examined infected at 6-week post injection. AAV9-GFP and AAV2/1-GFP lost expression in all brain regions at 6-weeks post-ICV, whereas AAVDJ8-GFP expression decreased only in the cortex and hippocampus. The reduction in AAV transgene expression is consistent with other studies utilizing CMV-promoter based AAVs(McCown *et al.*, 1996; RL Klein *et al.*, 1998). Explanations for the observed loss of AAV transgene expression over time could be attributed to cell turnover within the given regions or that CMV promoters are prone to transcriptional inactivation by DNA methylation during viral latency (Royo *et al.*, 2008). It was also reported that AAV transgene expression and persistence is improved when utilizing an endogenously expressed promoter-neuron-specific enolase (NSE)-containing construct compared to a CMV-containing construct (RL Klein *et al.*, 1998).

AAV2/1 had very minimal penetrance to the ventral midbrain area at both time points. AAVDJ8 was persistent in expression and AAV9 decreased from ~15 to ~6 GFP⁺/image field in the SNpc. In support of our findings, previous studies reported ~46% of neurons in the SN were transduced with AAV9-hSyn-GFP at 6 weeks post ICV(McLean *et al.*, 2014). Correspondingly, we quantitated ~45% TH⁺ neurons and ~22% S100 β ⁺ astrocytes/per field with AAV9 (**Figure 6D,H**). Also, AAV9 transduced more TH⁺ neurons than AAVDJ8, whereas AAVDJ8 transduced more astrocytes (**Fig 6G**). Co-localization (GFP +TH or S100B) and intensity values of GFP signal were also measured. As expected, AAVDJ8 had significantly higher GFP signal in both cell types due to the construct containing CAG promoter and eGFP, but Pearson's colocalization coefficients were not significantly different between serotypes, indicating higher GFP signal did not

interfere with quantitative analysis (**Supplemental Fig 2A**). Based on morphological co-localization studies, we noted a lack of co-localization of GFP with IBA1⁺ cells using any serotype (see **Supplementary Figure 6A-B**). This is consistent with other reports using these AAV vectors, which identified oligodendrocytes as an additional cell type transduced by these vectors rather than microglia (Lawlor *et al.*, 2009; Chakrabarty *et al.*, 2013; Aschauer, Kreuz, and Rumpel, 2013a). Although the levels of AAV infectivity in the SNpc by ICV delivery were not as robust compared to the alternative SN stereotaxic injection method, there was evident penetration with AAV9 and AAVDJ8 within this region of the brain that suggests these two serotypes would be suitable for targeting specific cells of the SNpc via ICV administration (**Fig 6H**).

Neuroinflammatory mechanisms that cause dopaminergic neuronal loss during PD progression are heavily mediated by astrocyte activation (De Miranda *et al.*, 2014). Here, we report AAVDJ8 to be a stable serotype to transduce astrocytes of the SNpc by ICV at 6 weeks (**Fig. 6G-H**). By use of enhanced CLARITY microscopy, AAVDJ8-eGFP expression can be visualized in brain tissue at ~2 times greater z-dimensions primarily in GFAP⁺ astrocytes in a 3D-volumetric view of the SN (**Fig 6E, Supplemental Video 1**). To further limit AAV transgene to astrocytes, we tested the use of truncated 681 bp human-*gfap* (*gfaABC1D*) promoter in AAVDJ8-GFAP-mCherry constructs by ICV delivery (**Fig. 7A**). The *gfaABC1D* promoter was previously designed to have two-fold greater activity than full-length (2.2kb) promoter and with much smaller size, ideal for the limited cloning capacity in AAV vectors (Y Lee *et al.*, 2008). The full-length human-*gfap* was previously validated to transduce astrocytes with AAV2/1 striatal neonatal injections and selectivity of the 1.74 kb GFAP promoter has been tested with combined serotype

AAV2/5/7/8/9 by cortical injection. More specifically, gfaABC1D promoter has been used with AAV9 via intramuscular delivery (Jonquieres *et al.*, 2013; Meng *et al.*, 2015; Vagner *et al.*, 2016). The data presented here are the first report that AAVDJ8-GFAP-mCherry efficiently and selectively expresses in cultured astrocytes and in the SNpc following neonatal ICV delivery in mice (**Fig 7B, 7D**). In culture, longer DIV incubation time and higher titer was required for robust mCherry expression, most likely because the GFAP promoter is weaker than CAG/CMV in culture. However, *in vivo* we noticed similar distribution patterns of AAVDJ8-GFAP-mCherry compared to AAVDJ8-eGFP in sagittal plane views (**Fig. 7C, Fig 2G**). There was also comparable number of mCherry⁺ cells/image field at 3-6 weeks to GFP⁺ cells/image field in the SN. AAVDJ8-eGFP had slightly higher number of transduced cells in this region at 6 weeks due to observed neurons transduced with this vector and no identified TH⁺/mCherry⁺ cells with AAVDJ8-GFAP-mCherry (**Fig 6D-G, Fig 7D-F**). To fully visualize exclusive astrocyte-specific targeting of AAVDJ8-GFAP-mCherry we also conducted CLARITY immunofluorescent imaging, this time at ~4.5 times greater z-stack thickness than normal tissue samples for a better view of AAV penetrance within the SN (**Fig 7F, Supplemental Video 2**). Serotype differences *in vivo* were partially attributed to the ability to penetrate into the parenchymal space by ICV administration method, however there were differences in brain regions and cell specific transduction patterns compared to *in vitro* results. For example, AAV2/1 had the highest transduction efficiency *in vitro*, but did not virally express as well compared to AAV9/AAVDJ8 in the SNpc or was as stable in other regions compared to AAVDJ8 at 6-weeks. The observed differences of serotype transduction efficacies *in vitro* compared to *in vivo* are a common issue when determining ideal serotypes for specific brain regions

and further supports the rationale to proceed past an initial *in vitro* assessment if the viral models are intended to be used *in vivo* (Hemphill *et al.*, 2014). Lastly, with selection of the appropriate combination of serotype and promoter, targeting specific cell types within the SNpc can be accomplished for transgene expression for studies of biological mechanism or disease intervention.

5.5 FUTURE DIRECTIONS AND PRELIMINARY DATA

The previous data set described optimization of AAV serotype transductions into neurons and astrocytes. We therefore were interested in using the identified serotype for optimal astrocyte transduction (AAVDJ8-GFAP) to overexpress a transgene that would counter-regulate NF κ B proinflammatory gene expression and potentially protect DA neurons from degeneration in mouse model of PD. Based on our previous results described in chapters 2-4, we decided to overexpress the coding sequence of Nurr1, specifically in astrocytes of the SN. The vector design for this approach used the previously validated backbone AAVDJ8-hGFAP-mCherry with a 2A-peptide linker sequence. During translation the 2A-peptide linker allows for a ribosomal skip after the last amino acid of the C-terminus end and release of the first fused protein, GFAP-mCherry, along with most of the 2A peptide (~18 amino acids). The ribosome then translates the rest of the open reading frame (ORF), including 1 amino acid fused to the N-terminus (NTD) of the second downstream protein, Nurr1. In contrast to IRES sequences, the 2A-linker allows for an equimolecular proportion of both proteins, so mCherry fluorescent expression should directly correlate to Nurr1 transgene expression (de Felipe, 2004; Heinonen *et al.*, 2014). The directionality of this ORF considered the location of Nurr1s' proposed ligand binding domain located at the C-terminus, so mCherry

was placed upstream of the 2A-linker to carry the fused ~18 amino acids at the NTD (**Fig 8A**).

We tested the newly designed AAV-Nurr1 in primary astrocyte cultures (method previously described earlier in this chapter). After a week of transduction, we collected mRNA and performed qPCR on Nurr1. AAV-Nurr1 induced Nurr1 mRNA ~1000 fold higher than AAV-mCherry empty control (**Fig. 8B**) ($N=4/\text{group}$; $***P < 0.001$). Additionally, to visualize Nurr1 protein expression, we performed IF with anti-mCherry (red) and anti-Nurr1 (green) after 1-week of transduction. The AAV-Nurr1 cultures noticeably expressed Nurr1 in the nucleus compared to less in AAV-empty (representation of 3 individual experiments) (**Fig 8C**). However, one issue that persisted was the lack of native mCherry expression with AAV-Nurr1 (*data not shown*). This required using anti-mCherry to visualize AAV transduced astrocytes and is a potential concern for future studies.

A pilot *in vivo* test was also performed to confirm AAV-Nurr1 efficacy in protecting DA neurons from MPTP-induced neurotoxicity. To specifically target the SN in adult mice, we tested stereotaxic injections using known coordinates (Oh *et al.*, 2015). As depicted in **Figure 9A** we specifically targeted the left hemisphere with either AAV-Nurr1 or AAV-mCherry empty control. After 5 days of recovery, the adult mice were challenged with an MPTP dosing regimen as previously described in chapter 2 with the absence of probenecid treatment (**Fig 9B**). Brain tissue was then collected for stereological assessment of TH⁺ neurons in both treatment groups. **Figure 9C** depicts localization of AAV-mCherry (red) in the left hemisphere surrounding TH⁺ neurons (blue). The SN was quantitated for total TH⁺ neurons using similar methods previously described in chapter 2. Based on the preliminary results, there appears to be a neuroprotective trend with AAV-

Nurr1 over AAV-mcherry empty control (**Fig 9D**). However, these data are only an $N=2$ and require a larger cohort of mice to fully validate statistical power of this finding.

In summary, these studies are ongoing and require additional experimentation to confirm efficacy of AAV-Nurr1 to slow neurodegeneration in mouse models of PD. Additionally, we are in the process of testing another vector without the inclusion of a T2A skipping sequence, due to the lack of native mCherry signal that is expressed in the vector described in **Figure 8A**. This will create a fusion protein of mCherry-Nurr1, which is currently being tested *in vivo*. Overall, using AAV technology to overexpress a desirable gene candidate could be a promising approach to controlling neuroinflammation regulated by astrocytes and perhaps a highly translatable treatment development for PD patients.

5.6 FIGURES

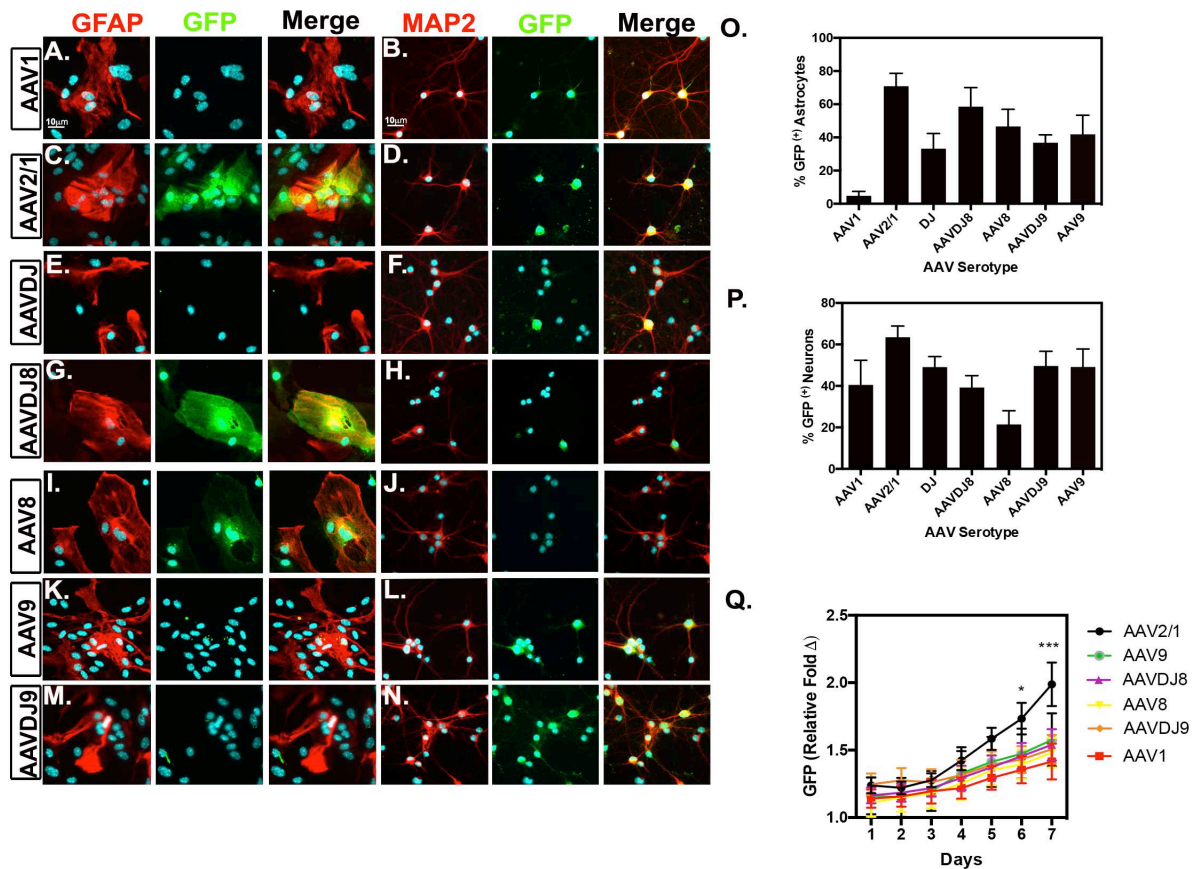


Fig 5.6.1 AAV2/1 is most efficient in primary neuron and astrocyte cultures. Primary neuron and astrocyte cultures transduced with multiple AAV serotypes for comparison by immunofluorescent analysis with astrocyte marker, GFAP (red; left) and neuronal marker MAP2 (red; right), GFP (green) and DAPI (cyan). Representative images of virally transduced GFP reporter are depicted in 20X objective images of (A-B) AAV1, (C-D) AAV2/1, (E-F) AAVDJ, (G-H) AAVDJ8, (I-J) AAV8, (K-L) AAV9, (M-N) and AAVDJ9. Percent of GFP⁺ astrocytes (O) and (P) neurons were quantitated by co-localization with specific cell marker. (Q) Live cell fluorescence was measured in primary neuronal cultures by native GFP detection each day for 7 DIV ($n=3-7$ /serotype; fixed astrocytes, $n=6-10$ /serotype; fixed neurons, $n=6$ /serotype; live cell; representation of three separate experiments; * $p<0.05$, *** $p<0.001$).

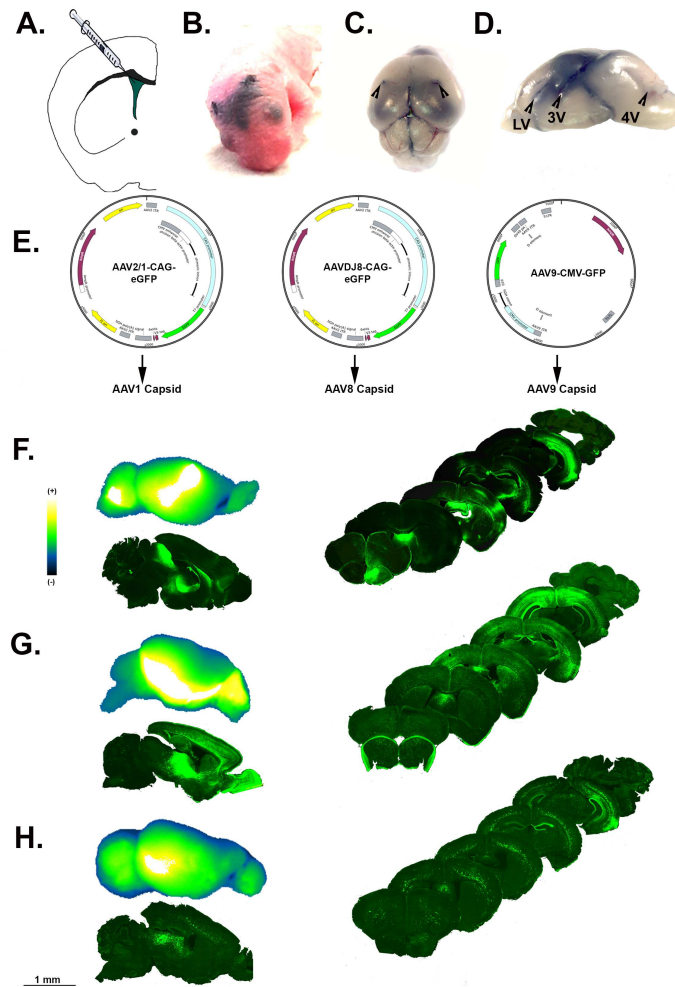


Fig 5.6.2 Intracerebroventricular injection of multiple AAV serotypes in neonatal P0 mice. (A) P0 neonatal mice were injected directly into the lateral ventricles for widespread viral solution as illustrated in cartoon schematic. (B) Mock injection of trypan blue/PBS solution was used to test successful target location at 2/5 from bregma suture and eye landmark. (C) Black arrows identify injection sites on dissected whole brain and (D) lateral ventricles (LV), 3rd ventricle (3V) and 4th ventricle (4V) on gross incised sagittal brain. (E) Plasmid AAV (pAAV) vector maps identify specific promoter/reporter elements of selected serotypes AAV2/1, AAVDJ8 and AAV9. Lateral plane view pseudo-colored whole brain native GFP fluorescence of (top), medial view of 10X objective montage images for sagittal cross sections (bottom) and rostral-caudal coronal cross sections (right) of (F) AAV2/1, (G) AAVDJ8, and (H) AAV9 injected brains at 3-weeks post injection (pseudocoloring scale of fluorescence: white=highest, black=lowest; all images are representation of 3-4 animals/serotype).

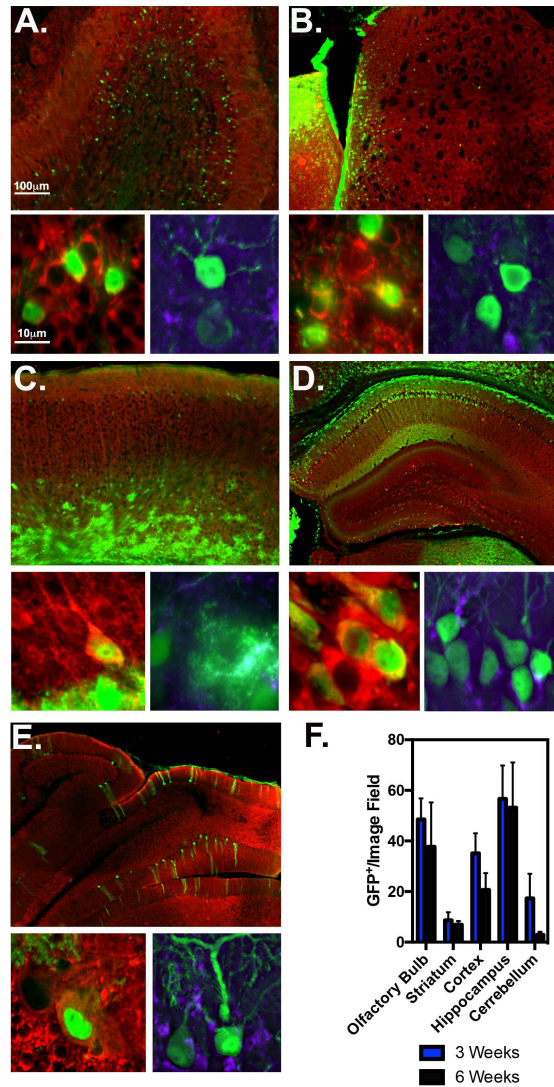


Fig 5.6.3 Tropism of AAV2/1 in multiple brain regions at 3 and 6 weeks post injection. AAV2/1 6-week injected tissue of multiple brain regions were immunostained for total neuronal marker MAP2 (red), astrocyte marker S100 β (purple) and GFP (green) as depicted in representative 10X montage (top) and 100X high magnification images (bottom) of the olfactory bulb (A), striatum (B), motor cortex (C), hippocampus (D) and cerebellum (E). Notice; red/green co-localize to yellow, green/purple co-localize to cyan. (F) Each region was quantitated for GFP⁺/per 20X objective image field at 3 and 6-weeks post AAV2/1 injection ($n=3-4$ /serotype/time point).

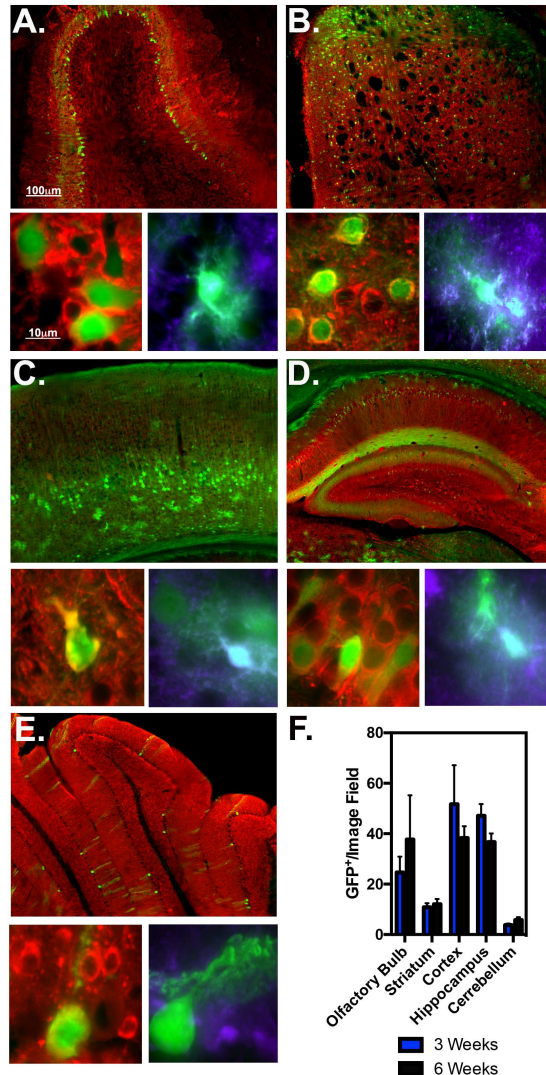


Fig 5.6.4 Tropism of AAVDJ8 in multiple brain regions at 3 and 6 weeks post injection. AAVDJ8 6-week injected tissue of multiple brain regions were immunostained for total neuronal marker MAP2 (red), astrocyte marker S100β (purple) and GFP (green) as depicted in representative 10X montage (top) and 100X high magnification images (bottom) of the olfactory bulb (A), striatum (B), motor cortex (C), hippocampus (D) and cerebellum (E). Notice; red/green co-localize to yellow, green/purple co-localize to cyan. (F) Each region was quantitated for GFP⁺/per 20X objective image field at 3 and 6-weeks post AAVDJ8 injection ($n=3$ /serotype/time point).

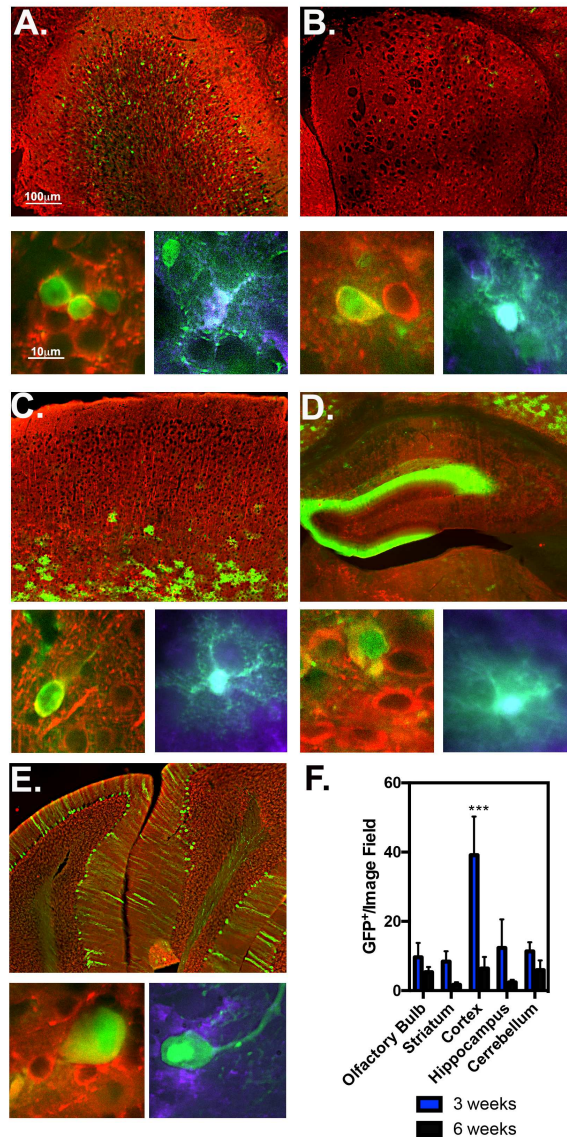


Fig 5.6.5 Tropism of AAV9 in multiple brain regions at 3 and 6 weeks post injection.

AAV9 6-week injected tissue of multiple brain regions were immunostained for total neuronal marker MAP2 (red), astrocyte marker S100 β (purple) and GFP (green) as depicted in representative 10X montage (top) and 100X high magnification images (bottom) of the olfactory bulb (**A**), striatum (**B**), motor cortex (**C**), hippocampus (**D**) and cerebellum (**E**). Notice; red/green co-localize to yellow, green/purple co-localize to cyan. (**F**) Each region was quantitated for GFP⁺/per 20X objective image field at 3 and 6-weeks post AAV9 injection ($n=3$ /serotype/time point; * $p<0.05$).

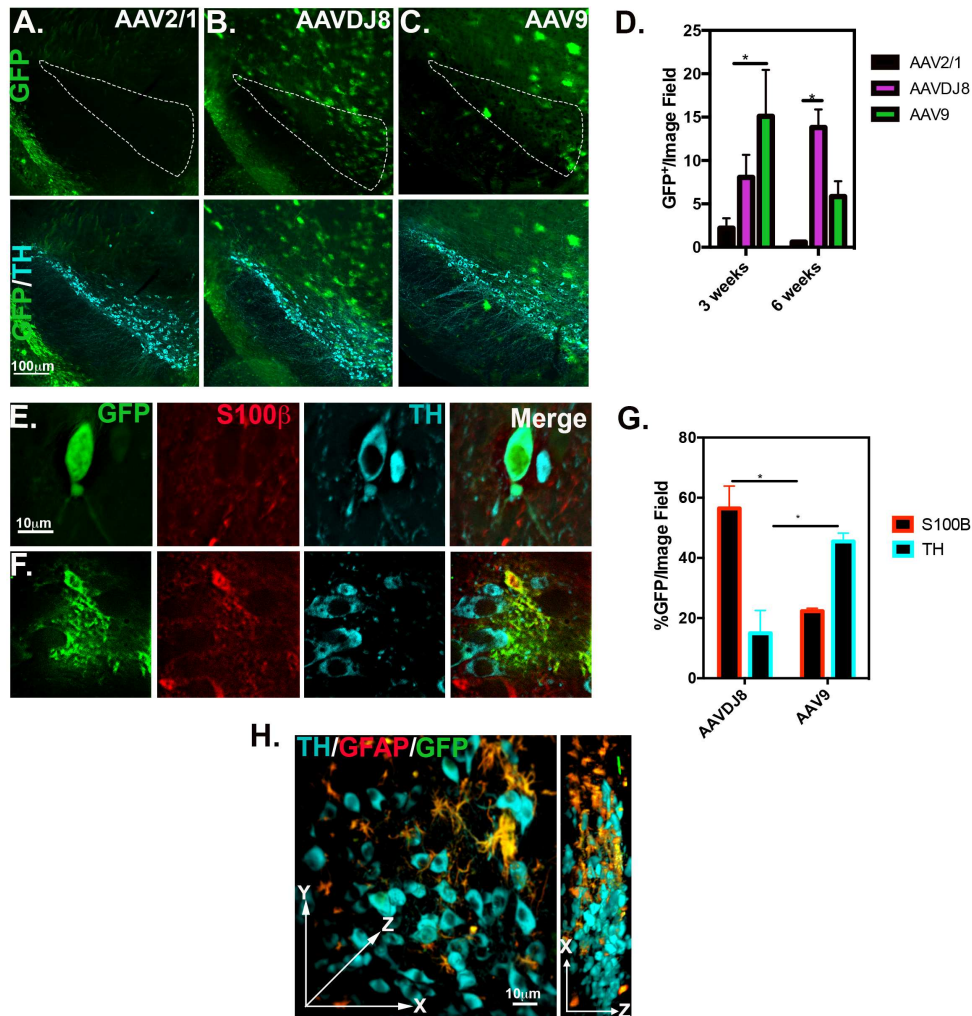


Fig 5.6.6 AAV9 and AAVDJ8 transduce DA neurons and astrocytes of the substantia nigra 10X objective representative images of SN from 6-week tissue immunostained for TH (cyan) to visualize viral GFP expression (native) in the SN pars compacta (white outline) and SN pars reticulata for AAV2/1 (A), AAVDJ8 (B), and AAV9 (C) injected brains. (D) Total GFP⁺ cells/ 20X objective image field were quantitated for both 3 and 6-weeks post injection within the SN region ($n=3$ /serotype; $*p<0.05$). (E) AAV9 and (F) AAVDJ8 100X objective representative images immunostained for TH and S100 β (red) within the SNpc. at 6-weeks post ICV. (G) % S100 β -GFP⁺ and TH-GFP⁺ cells in the SNpc were quantitated/per 40X objective image field ($n=3$ /serotype; $p<0.05$). (H) Representative, three dimensional (3D) 40X objective montage image of clarified SN tissue from a AAVDJ8-GFP infected brain, immunostained for TH (cyan), GFAP (red) and GFP (green) in XYZ and XZ volumetric planes. Video of 3D projection can be found in **S1 video**.

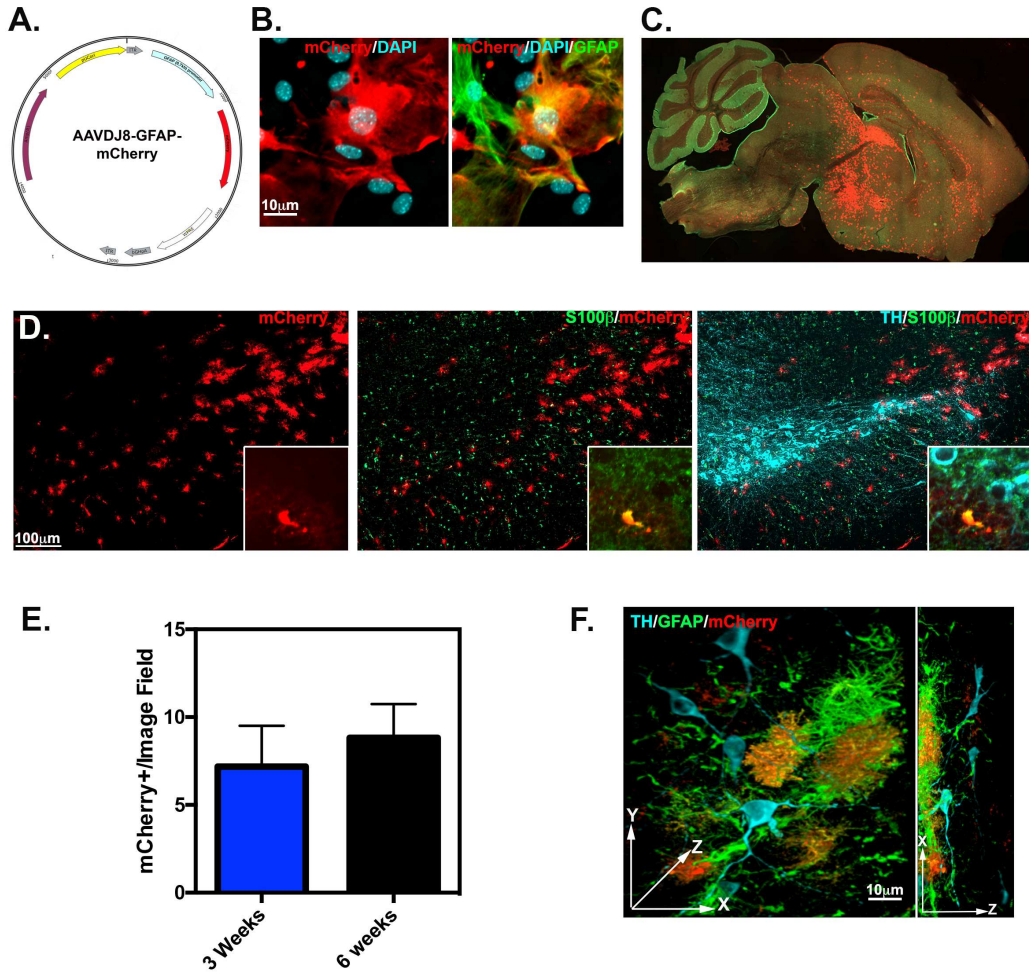


Figure 5.6.7 AAVDJ8-GFAP-mCherry targets exclusively astrocytes in the Substantia Nigra. (A) Astrocyte-specific promoter, GFAP, was incorporated into suitable serotype AAVDJ8 to drive expression of fluorescent reporter, mCherry for targeting astrocytes, as depicted in plasmid AAV vector map. (B) Primary astrocyte cultures were transduced with AAVDJ8-GFAP-mCherry to confirm astrocyte transduction efficiency *in vitro* as depicted in representative 100X objective images of immunostaining for mCherry (red) and GFAP (green), 83.2%±6.5 GFAP⁺/mCherry⁺ quantitated. (C) mCherry (red) and S100β (green) immunofluorescence is visualized in 10X objective montage image of sagittal cross section from AAVDJ8-GFAP-mCherry 3-week infected brain. (D) AAVDJ8-GFAP-mCherry expression in 10X objective image of SN region immunostained for mCherry (red), S100β (green), and TH (cyan) from 3 week infected brain, 100X objective inset images represent colocalization of S100β⁺/mCherry⁺ cells. (E) AAVDJ8-GFAP-mCherry expression levels were quantitated for mCherry⁺ cells/20X objective image field at 3 and 6 weeks post-ICV ($n=3$ /serotype, groups were not significant). (F) 3D volumetric view in XYZ and XY planes for CLARITY immunofluorescent image stained for TH (cyan), GFAP (green) and mCherry (red) within the SNpc. AAVDJ8-GFAP-mCherry infected astrocytes are exclusively co-localizing with GFAP⁺ cells within the vicinity of dopaminergic neurons. Video of 3D projection can be found in **Supplemental Video 2**.

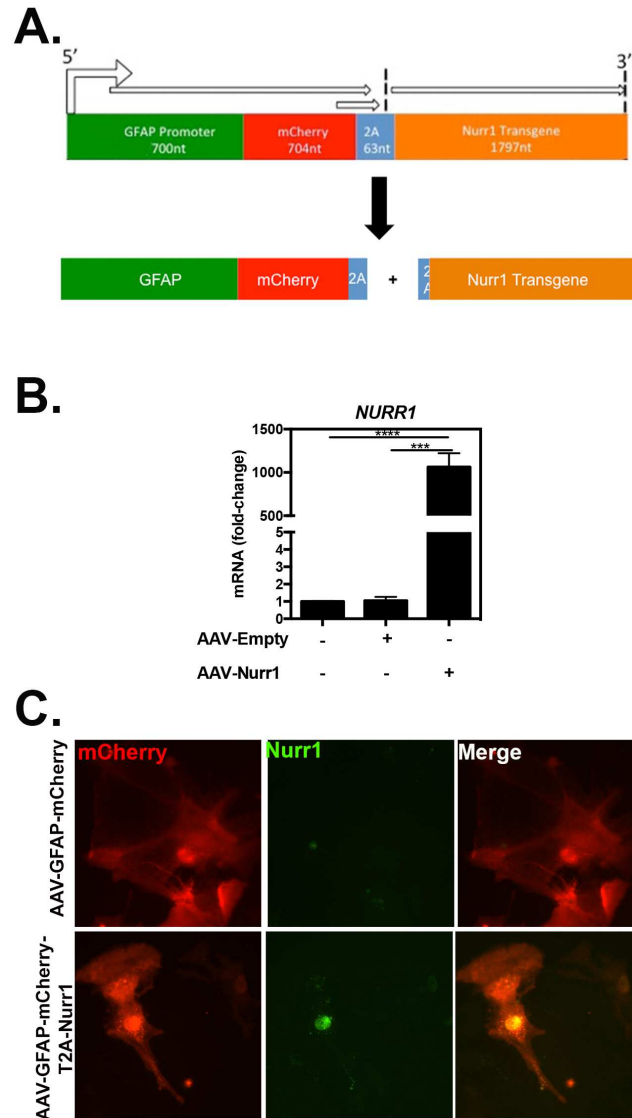


Figure 5.6.8 AAVDJ8-hGFAP-mCherry-T2A-Nurr1 vector design and transduction test *in vitro* (A) Using AAVDJ8-GFAP to transduce astrocytes we incorporated a ribosomal skipping T2A sequence downstream of mCherry reporter for a 1:1 ratio of reporter and coding sequence of the murine Nurr1 gene. (B) By qPCR analysis we detected ~1000 fold increase of Nurr1 mRNA expression in primary astrocytes cultures transduced with AAV-Nurr1 compared to AAV-mCherry empty control ($N=4/\text{group}$; $***P < 0.001$). (C) IF images of anti-mCherry (red) and anti-Nurr1 (green) expression in AAV-Nurr1 and AAV-empty control transduced cultures (images represent 3 individual experiments).

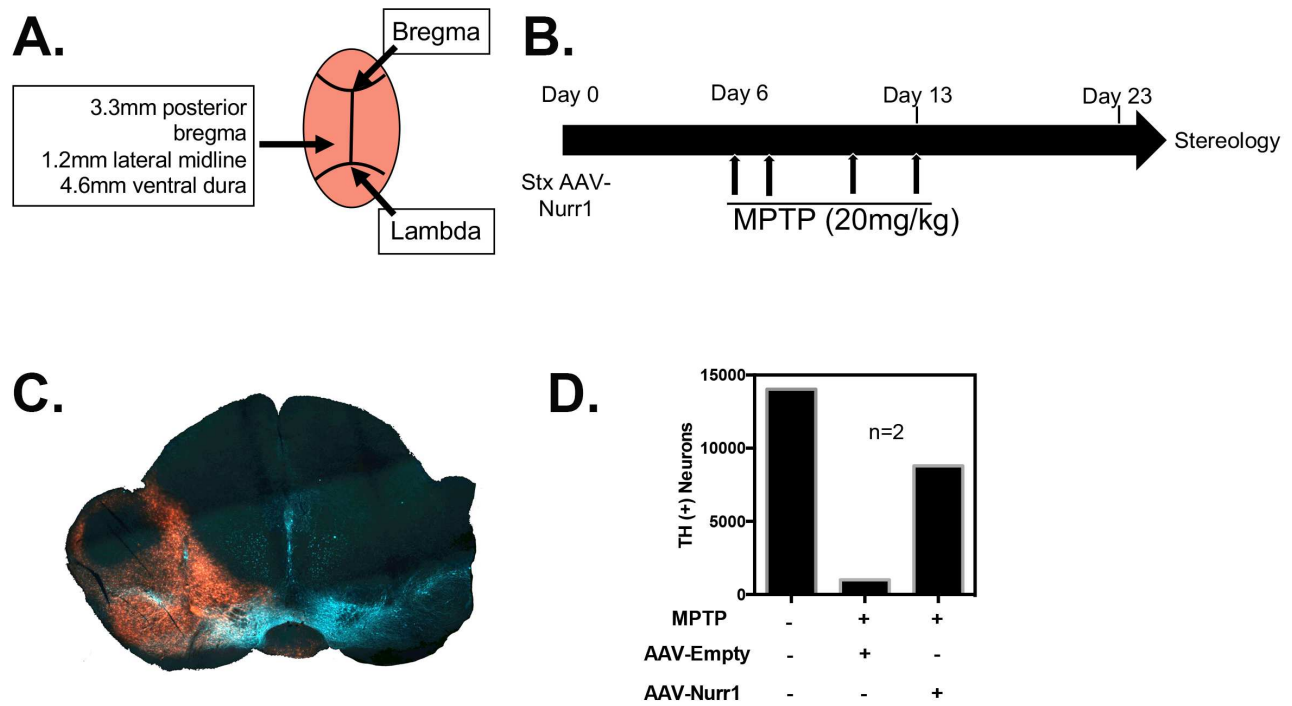


Figure 5.6.9. AAV-hGFAP-mCherry-T2A-Nurr1 injection test *in vivo* and challenge with MPTP (A) For adult stereotaxic injections, the left hemisphere was targeted for AAV administration into SN as depicted in coordinate map. (B) After stx. Injections mice were allowed to recover for 5 days following MPTP administration as depicted in treatment schematic. (C) 10x-objective montage image of injected shows anti-mCherry (red) expressed in vicinity of TH⁺ neurons (blue) of left hemisphere. (D) Preliminary stereological DA cell counts depict a neuroprotective trend with AAV-Nurr1 compared to AAV-empty (N=2).

CHAPTER 6

DISCUSSION AND FINAL CONCLUSIONS

Since current PD treatments only ameliorate symptoms, a new approach to halt irreversible damage to neurons is necessary for patient improvement. Many PD studies solely focus on function of the neuron during disease progression and perhaps limits discovery for treatment. As described in the dissertation, non-neuronal cells, astrocytes and microglia mediate a highly complex network of cellular communication, that should not be ignored. This process of communication by glia cells, known as neuroinflammation, can result in neurodegeneration, irrespective to the preceding state of the neuron. Thus, the studies described in Chapter 2-5, reflect cell-specific strategies for PD treatment by modifying only the astrocyte with a transgenic mouse model (Chapter 2), modifying solely the neuron *in vitro* (Chapter 3), targeting all cells *in vivo* (Chapter 4) or specifically targeting the astrocyte with a viral vector (Chapter 5). For a summation of each strategy, the following will detail each in reference to corresponding figures.

Chapter 2 described a novel astrocyte-specific NF- κ B knock-out mouse that revealed a highly neuroprotective mechanism which improved the neurological and pathological outcome of animals treated with both MPTPp and MnCl₂ (**Figure 1**). Inhibition of NF- κ B in astrocytes resulted in decreased reactivity of both glial cell types and astrocyte expression of complement protein C3, demonstrating suppression of a crucial innate immune response pathway. This resulted in a 92% protection of DA neurons against toxicity and apoptosis. The experimental approach in **Figure 1**. for

neuroinflammatory intervention is interesting, yet only demonstrative in a transgenic mouse model, not a translatable approach for PD. Additionally, concerns exist because keratinocytes also express GFAP which resulted in an off-target lesioning effect that occurred in ~30% of the KO animals, previously described by Kirkley et al 2017 as squamous cell carcinoma (Kirkley et al 2017). Therefore, another approach is necessary for solely modifying cells of the CNS which can be easily administered to humans.

The second strategy for disease modification was detailed in chapters 3 and 4. Using the small molecular compound, C-DIM12, we demonstrated activation of the molecular target, Nurr1 to protect DA neurons *in vitro* and *in vivo*. **Figure 2.** depicts C-DIM12 targeting all cells in the CNS that express Nurr1. *In vivo*, we showed that during co-current lesioning with MPTP, oral administration of C-DIM12 suppressed gliosis by counter-regulating NF- κ B. Additionally, the effects of C-DIM12 in neurons can induce Nurr1 regulated DA'ergic genes, TH, VMAT2 and DAT. These effects on multiple cell types resulted in ~64% protection of DA neurons. Although, as previously mentioned, the expression of NF- κ B in neurons has been proven beneficial for proper neuronal development and synaptogenesis (red text; **Figure 2**). This raises concern if synaptic health is compromised by counter-regulating neuronal NF- κ B which remains to be tested in future studies.

Lastly, the final strategy for modulating neuroinflammation during the progression of PD could be a viral-mediated gene therapeutic approach. As described in chapter 5, AAVs have powerful capacity to deliver transgenes to both neurons and astrocytes. The future directions section of this chapter also discussed preliminary data using a recombinant AAV to overexpress Nurr1 specifically into astrocytes of the SN. As depicted

in **Figure 3**, the ongoing studies show that Nurr1 expression is increased in astrocytes and NF- κ B activity is suppressed (*data not shown*). However, whether full suppression of glial activation and protection of DA neurons from degeneration with AAV-Nurr1 is still not known. Astrocyte-specific inhibition of NF- κ B in the transgenic mouse model (**Figure 1**) provided more neuroprotection than the global suppression of NF- κ B with C-DIM12 (**Figure 2**). Potentially, a combinatorial effect with Nurr1 activating drugs, such as C-DIM12, and AAV-Nurr1 could convey enhanced neuroprotection to DA neurons, rather than one monotherapy.

In summation, the many intricacies that cause DA neuronal loss impel the tantalizing difficulties in experimental drug discovery. As neurodegeneration requires synergism from multiple causing factors as well as multiple cell types and pathways. Combinatorial effects of several drugs may be necessary to alleviate all possible contributors to PD pathology. Thus, the more innovative approaches we have for disease modification, the closer we will be to overcoming this debilitating disorder.

6.1 FIGURES

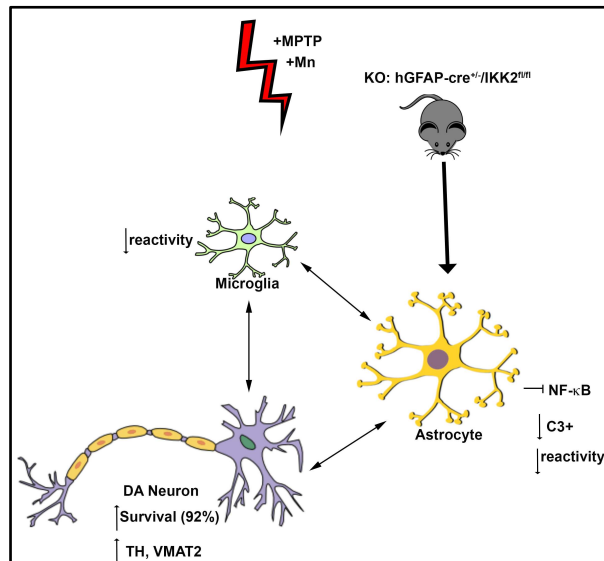


Figure 6.1.1 Astrocyte-specific modulation with transgenic mouse model (detailed in chapter 2).

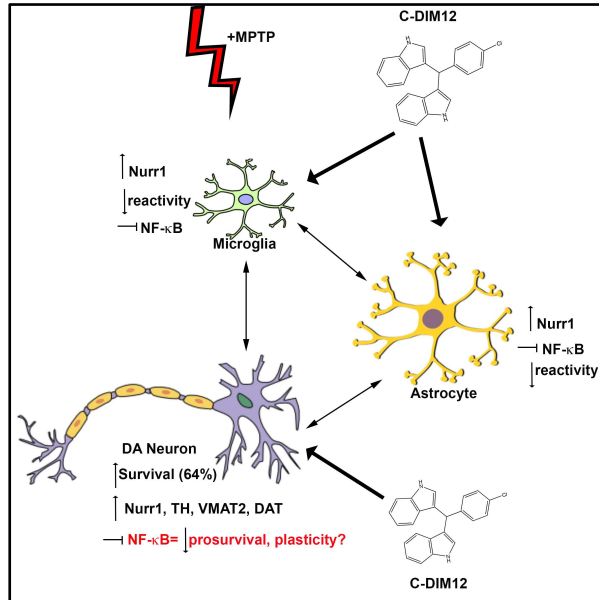


Figure 6.1.2 Global strategy for neuroinflammatory modulation (detailed in chapters 3-4)

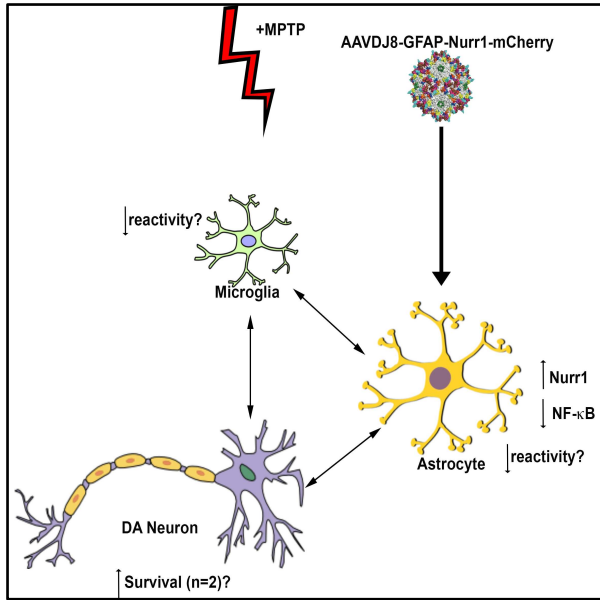


Figure 6.1.3 Astrocyte-specific modulation with AAV-Nurr1 (detailed in chapter 5; AAV image provided by Kotterman et al. 2014)

REFERENCES

- Akache B, Grimm D, Pandey K, Yant SR, Xu H, and Kay MA (2006) The 37/67-Kilodalton Laminin Receptor Is a Receptor for Adeno-Associated Virus Serotypes 8, 2, 3, and 9. *Journal of Virology* **80**:9831–9836.
- Aschauer DF, Kreuz S, and Rumpel S (2013a) Analysis of Transduction Efficiency, Tropism and Axonal Transport of AAV Serotypes 1, 2, 5, 6, 8 and 9 in the Mouse Brain. *PLoS ONE* **8**:e76310–16.
- Aschauer DF, Kreuz S, and Rumpel S (2013b) Analysis of Transduction Efficiency, Tropism and Axonal Transport of AAV Serotypes 1, 2, 5, 6, 8 and 9 in the Mouse Brain. *PLoS ONE* **8**:e76310–16.
- Baltimore D (2009) Discovering NF-kappaB. *Cold Spring Harbor Perspectives in Biology* **1**:a000026–a000026, Cold Spring Harbor Lab.
- Bartus RT, Baumann TL, Siffert J, Herzog CD, Alterman R, Boulis N, Turner DA, Stacy M, Lang AE, Lozano AM, and Olanow CW (2013) Safety/feasibility of targeting the substantia nigra with AAV2-neurturin in Parkinson patients. *Neurology* **80**:1698–1701, Lippincott Williams & Wilkins.
- Beaudin SA, Strupp BJ, Strawderman M, and Smith DR (2016) Early Postnatal Manganese Exposure Causes Lasting Impairment of Selective and Focused Attention and Arousal Regulation in Adult Rats. *Environ Health Perspect* **1**–36.
- Boakye CHA, Doddapaneni R, Shah PP, Patel AR, Godugu C, Safe S, Katiyar SK, and Singh M (2013) Chemoprevention of Skin Cancer with 1,1-Bis (3'-Indolyl)-1-(Aromatic) Methane Analog through Induction of the Orphan Nuclear Receptor, NR4A2 (Nurr1). *PLoS ONE* **8**:e69519–10.
- Braak H, Ghebremedhin E, Rüb U, Bratzke H, and Del Tredici K (2004) Stages in the development of Parkinson's disease-related pathology. *Cell Tissue Res* **318**:121–134, Springer-Verlag.
- Breidert T, Callebert J, Heneka MT, Landreth G, Launay JM, and Hirsch EC (2002) Protective action of the peroxisome proliferator-activated receptor-gamma agonist pioglitazone in a mouse model of Parkinson's disease. *J Neurochem* **82**:615–624.
- Burger C, Gorbatyuk OS, Velardo MJ, Peden CS, Williams P, Zolotukhin S, Reier PJ, Mandel RJ, and Muzyczka N (2004) Recombinant AAV Viral Vectors Pseudotyped with Viral Capsids from Serotypes 1, 2, and 5 Display Differential Efficiency and Cell Tropism after Delivery to Different Regions of the Central Nervous System. *YMTHE* **10**:302–317, The American Society of Gene Therapy.

- Burton NC, Schneider JS, Syversen T, and Guilarte TR (2009) Effects of Chronic Manganese Exposure on Glutamatergic and GABAergic Neurotransmitter Markers in the Nonhuman Primate Brain. *Toxicological Sciences* **111**:131–139.
- Carbone DL, Popichak KA, Moreno JA, Safe S, and Tjalkens RB (2008) Suppression of 1-Methyl-4-phenyl-1,2,3,6-tetrahydropyridine-Induced Nitric-Oxide Synthase 2 Expression in Astrocytes by a Novel Diindolylmethane Analog Protects Striatal Neurons against Apoptosis. *Molecular Pharmacology* **75**:35–43.
- Chakrabarty P, Rosario A, Cruz P, Siemienski Z, Ceballos-Diaz C, Crosby K, Jansen K, Borchelt DR, Kim J-Y, Jankowsky JL, Golde TE, and Levites Y (2013) Capsid Serotype and Timing of Injection Determines AAV Transduction in the Neonatal Mice Brain. *PLoS ONE* **8**:e67680–9.
- Chevalier G, Suberbielle E, Monnet C, Duplan V, Martin-Blondel G, Farrugia F, Le Masson G, Liblau R, and Gonzalez-Dunia D (2011) Neurons are MHC Class I-Dependent Targets for CD8 T Cells upon Neurotropic Viral Infection. *PLoS Pathog* **7**:e1002393–14.
- Choi VW, McCarty DM, and Samulski RJ (2005) AAV hybrid serotypes: improved vectors for gene delivery. *Curr Gene Ther* **5**:299–310.
- Connor B, Sun Y, Hieber von D, Tang SK, Jones KS, and Maucksch C (2016) AAV1/2-mediated BDNF gene therapy in a transgenic rat model of Huntington's disease. *Gene Ther* **23**:283–295.
- Cooper AA, Gitler AD, Cashikar A, Haynes CM, Hill KJ, Bhullar B, Liu K, Xu K, Strathearn KE, Liu F, Cao S, Caldwell KA, Caldwell GA, Marsischky G, Kolodner RD, Labaer J, Rochet J-C, Bonini NM, and Lindquist S (2006) Alpha-synuclein blocks ER-Golgi traffic and Rab1 rescues neuron loss in Parkinson's models. *Science* **313**:324–328, American Association for the Advancement of Science.
- Cooper O, Astradsson A, Hallett P, Robertson H, Mendez I, and Isacson O (2009) Lack of functional relevance of isolated cell damage in transplants of Parkinson's disease patients. *J Neurol* **256 Suppl 3**:310–316.
- Couper, J (1837) The effects of manganese dioxide. *Journal of Medicinal Chemistry, Pharmacy and Toxicology*. **3**:223-225.
- Daya S, and Berns KI (2008) Gene therapy using adeno-associated virus vectors. *Clinical Microbiology Reviews* **21**:583–593, American Society for Microbiology.
- de Felipe P (2004) Genetic Vaccines and Therapy. *Genet Vaccines Ther* **2**:13–6.
- De Miranda BR, Miller JA, Hansen RJ, Lunghofer PJ, Safe S, Gustafson DL, Colagiovanni D, and Tjalkens RB (2013) Neuroprotective efficacy and pharmacokinetic behavior of novel anti-inflammatory para-phenyl substituted diindolylmethanes in a mouse model of Parkinson's disease. *J Pharmacol Exp Ther* **345**:125–138.

- De Miranda BR, Popichak KA, Hammond SL, Jorgensen BA, Phillips AT, Safe S, and Tjalkens RB (2015) The Nurr1 Activator 1,1-Bis(3'-Indolyl)-1-(p-Chlorophenyl)Methane Blocks Inflammatory Gene Expression in BV-2 Microglial Cells by Inhibiting Nuclear Factor κ B. *Molecular Pharmacology* **87**:1021–1034.
- De Miranda BR, Popichak KA, Hammond SL, Miller JA, Safe S, and Tjalkens RB (2015) Novel Para-Phenyl Substituted Diindolylmethanes Protect Against MPTP Neurotoxicity and Suppress Glial Activation in a Mouse Model of Parkinson's Disease. *Toxicological Sciences* **143**:360–373.
- Decressac M, Kadkhodaei B, Mattsson B, Laguna A, Perlmann T, and Bjorklund A (2012) α -Synuclein-Induced Down-Regulation of Nurr1 Disrupts GDNF Signaling in Nigral Dopamine Neurons. *Science Translational Medicine* **4**:163ra156–163ra156.
- Dodiya HB, Björklund T, Stansell J III, Mandel RJ, Kirik D, and Kordower JH (2009) Differential Transduction Following Basal Ganglia Administration of Distinct Pseudotyped AAV Capsid Serotypes in Nonhuman Primates. *YMTHE* **18**:579–587, The American Society of Gene & Cell Therapy.
- Dong C-M, Wang X-L, Wang G-M, Zhang W-J, Zhu L, Gao S, Yang D-J, Qin Y, Liang Q-J, Chen Y-L, Deng H-T, Ning K, Liang A-B, Gao Z-L, and Xu J (2014) A stress-induced cellular aging model with postnatal neural stem cells. *Cell Death Dis* **5**:e1116.
- Dringen R, Pfeiffer B, and Hamprecht B (1999) Synthesis of the antioxidant glutathione in neurons: supply by astrocytes of CysGly as precursor for neuronal glutathione. *Journal of Neuroscience* **19**:562–569.
- Drinkut A, Tereshchenko Y, Schulz JB, Bähr M, and Kügler S (2012) Efficient gene therapy for Parkinson's disease using astrocytes as hosts for localized neurotrophic factor delivery. *Mol Ther* **20**:534–543.
- Erikson KM, and Aschner M (2003) Manganese neurotoxicity and glutamate-GABA interaction. *Neurochemistry International* **43**:475–480.
- Foust KD, Nurre E, Montgomery CL, Hernandez A, Chan CM, and Kaspar BK (2008) Intravascular AAV9 preferentially targets neonatal neurons and adult astrocytes. *Nat Biotechnol* **27**:59–65.
- Freed CR, Zhou W, and Breeze RE (2011) Dopamine cell transplantation for Parkinson's disease: the importance of controlled clinical trials. *Neurotherapeutics* **8**:549–561.
- García-Yagüe ÁJ, Rada P, Rojo AI, Lastres-Becker I, and Cuadrado A (2013) Nuclear import and export signals control the subcellular localization of Nurr1 protein in response to oxidative stress. *Journal of Biological Chemistry* **288**:5506–5517, American Society for Biochemistry and Molecular Biology.

- George S, van den Buuse M, San Mok S, Masters CL, Li Q-X, and Culvenor JG (2008) Alpha-synuclein transgenic mice exhibit reduced anxiety-like behaviour. *Experimental Neurology* **210**:788–792.
- Giasson BI, Duda JE, Quinn SM, Zhang B, Trojanowski JQ, and Lee VM-Y (2002) Neuronal alpha-synucleinopathy with severe movement disorder in mice expressing A53T human alpha-synuclein. *Neuron* **34**:521–533, American Society for Biochemistry and Molecular Biology.
- Giovanni A, Sieber BA, Heikkila RE, and Sonsalla PK (1994) Studies on species sensitivity to the dopaminergic neurotoxin 1-methyl-4-phenyl-1,2,3,6-tetrahydropyridine. Part 1: Systemic administration. *J Pharmacol Exp Ther* **270**:1000–1007.
- Glass CK, Saijo K, Winner B, Marchetto MC, and Gage FH (2010) Mechanisms Underlying Inflammation in Neurodegeneration. *Cell* **140**:918–934, Elsevier Inc.
- Goldberg NRS, Hampton T, McCue S, Kale A, and Meshul CK (2011) Profiling changes in gait dynamics resulting from progressive 1-methyl-4-phenyl-1,2,3,6-tetrahydropyridine-induced nigrostriatal lesioning. *J Neurosci Res* **89**:1698–1706, Wiley Subscription Services, Inc., A Wiley Company.
- Gordon PH, Moore DH, Miller RG, Florence JM, Verheijde JL, Doorish C, Hilton JF, Spitalny GM, MacArthur RB, Mitsumoto H, Neville HE, Boylan K, Mozaffar T, Belsh JM, Ravits J, Bedlack RS, Graves MC, McCluskey LF, Barohn RJ, Tandan R, Western ALS Study Group (2007) Efficacy of minocycline in patients with amyotrophic lateral sclerosis: a phase III randomised trial. *The Lancet Neurology* **6**:1045–1053.
- Gorman, C and C Bullock. 2000. "Site-Specific Gene Targeting for Gene Expression in Eukaryotes.." *Current opinion in biotechnology* 11(5):455–60.
- Gray SJ, Matagne V, Bachaboina L, Yadav S, Ojeda SR, and Samulski RJ (2011) Preclinical differences of intravascular AAV9 delivery to neurons and glia: a comparative study of adult mice and nonhuman primates. *Mol Ther* **19**:1058–1069.
- Guengerich FP (2011) Mechanisms of drug toxicity and relevance to pharmaceutical development. *Drug Metab Pharmacokinet* **26**:3–14.
- Guilarte TR, McGlothlan JL, Degaonkar M, Chen M-K, Barker PB, Syversen T, and Schneider JS (2006) Evidence for cortical dysfunction and widespread manganese accumulation in the nonhuman primate brain following chronic manganese exposure: a 1H-MRS and MRI study. *Toxicological Sciences* **94**:351–358, Oxford University Press.
- Gwiazda RH, Lee D, Sheridan J, and Smith DR (2002) Low cumulative manganese exposure affects striatal GABA but not dopamine. *Neurotoxicology* **23**:69–76.

- Hacein-Bey-Abina S, Kalle Von C, Schmidt M, McCormack MP, Wulffraat N, Leboulch P, Lim A, Osborne CS, Pawliuk R, Morillon E, Sorensen R, Forster A, Fraser P, Cohen JI, de Saint Basile G, Alexander I, Wintergerst U, Frebourg T, Aurias A, Stoppa-Lyonnet D, Romana S, Radford-Weiss I, Gross F, Valensi F, Delabesse E, Macintyre E, Sigaux F, Soulier J, Leiva LE, Wissler M, Prinz C, Rabbitts TH, Le Deist F, Fischer A, and Cavazzana-Calvo M (2003) LMO2-associated clonal T cell proliferation in two patients after gene therapy for SCID-X1. *Science* **302**:415–419, American Association for the Advancement of Science.
- Hammond, S L, Leek, A N, Richman, E H, & Tjalkens, R B (2017). Cellular selectivity of AAV serotypes for gene delivery in neurons and astrocytes by neonatal intracerebroventricular injection. *PLoS ONE*, *12*(12), e0188830. <http://doi.org/10.1371/journal.pone.0188830>
- Hammond, S L, Popichak, K P, Hunt, Li, X, Hunt, L G, Richman, Richman, E H, Damale, P, Chong, E, Backos, D S, Safe, S, Tjalkens, R B (2018) The Nurr1 ligand, 1,1-bis(3'-indolyl)-1-(p-chlorophenyl)methane modulates glial reactivity and is neuroprotective in the MPTP model of Parkinson's disease (*under review*)
- Hammond SL, Safe S, and Tjalkens RB (2015) A novel synthetic activator of Nurr1 induces dopaminergic gene expression and protects against 6-hydroxydopamine neurotoxicity in vitro. *Neuroscience Letters* **607**:83–89.
- He P, Liu H, Zhang, Q (1994) Effects of high-level-manganese sewage irrigation on children's neurobehavior. *Zhonghua Yu Fhang Yi Xue Za Zhi* **28**: 216-218.
- Heinonen A-M, Rahman M, Dogbevia G, Jakobi H, Wöfl S, Sprengel R, and Schwaninger M (2014) Neuroprotection by rAAV-mediated gene transfer of bone morphogenic protein 7. *BMC Neurosci* **15**:38, BioMed Central Ltd.
- Hemphill DD, McIlwraith CW, Samulski RJ, and Goodrich LR (2014) Adeno-Associated Viral Vectors Show Serotype Specific Transduction of Equine Joint Tissue Explants and Cultured Monolayers. *Sci Rep* **4**:1–7.
- Hirsch EC, and Hunot S (2010) Editorial. *J Neural Transm* **117**:897–898.
- Hirsch EC, and Hunot SP (2009) Neuroinflammation in Parkinson's disease: a target for neuroprotection? *The Lancet Neurology* **8**:382–397, Elsevier Ltd.
- Hirsch EC, Jenner P, and Przedborski S (2012) Pathogenesis of Parkinson's disease. *Mov Disord* **28**:24–30.
- Holehonnur R, Luong JA, Chaturvedi D, Ho A, Lella SK, Hosek MP, and Ploski JE (2014) Adeno-associated viral serotypes produce differing titers and differentially transduce neurons within the rat basal and lateral amygdala. *BMC Neurosci* **15**:28.

- Howard DB, Powers K, Wang Y, and Harvey BK (2008) Tropism and toxicity of adeno-associated viral vector serotypes 1, 2, 5, 6, 7, 8, and 9 in rat neurons and glia in vitro. *Virology* **372**:24–34.
- Hsiao H-Y, Chen Y-C, Chen H-M, Tu P-H, and Chern Y (2013) A critical role of astrocyte-mediated nuclear factor- κ B-dependent inflammation in Huntington's disease. *Human Molecular Genetics* **22**:1826–1842.
- Huang D, Wang Z, Tong J, Wang M, Wang J, Xu J, Bai X, Li H, Huang Y, Wu Y, Ma Y, Yu M, and Huang F (2018) Long-term Changes in the Nigrostriatal Pathway in the MPTP Mouse Model of Parkinson's Disease. *Neuroscience* **369**:303–313.
- Hui KY, Fernandez-Hernandez H, Hu J, Schaffner A, Pankratz N, Hsu N-Y, Chuang L-S, Carmi S, Villaverde N, Li X, Rivas M, Levine AP, Bao X, Labrias PR, Haritunians T, Ruane D, Gettler K, Chen E, Li D, Schiff ER, Pontikos N, Barzilai N, Brant SR, Bressman S, Cheifetz AS, Clark LN, Daly MJ, Desnick RJ, Duerr RH, Katz S, Lencz T, Myers RH, Ostrer H, Ozelius L, Payami H, Peter Y, Rioux JD, Segal AW, Scott WK, Silverberg MS, Vance JM, Ubarretxena-Belandia I, Foroud T, Atzmon G, Pe'er I, Ioannou Y, McGovern DPB, Yue Z, Schadt EE, Cho JH, and Peter I (2018) Functional variants in the LRRK2 gene confer shared effects on risk for Crohn's disease and Parkinson's disease. *Science Translational Medicine* **10**:eaai7795, American Association for the Advancement of Science.
- Impellizzeri D, Campolo M, Bruschetta G, Crupi R, Cordaro M, Paterniti I, Cuzzocrea S, and Esposito E (2016) Traumatic Brain Injury Leads to Development of Parkinson's Disease Related Pathology in Mice. *Front Neurosci* **10**:458.
- Inamoto T, Papineni S, Chintharlapalli S, Cho SD, Safe S, and Kamat AM (2008) 1,1-Bis(3'-indolyl)-1-(p-chlorophenyl)methane activates the orphan nuclear receptor Nurr1 and inhibits bladder cancer growth. *Molecular Cancer Therapeutics* **7**:3825–3833.
- Jackson-Lewis V, and Przedborski S (2007) Protocol for the MPTP mouse model of Parkinson's disease. *Nat Protoc* **2**:141–151.
- Jankovic J, Chen S, and Le WD (2005) The role of Nurr1 in the development of dopaminergic neurons and Parkinson's disease. *Progress in Neurobiology* **77**:128–138.
- Johnson MM, Michelhaugh SK, Bouhamdan M, Schmidt CJ, and Bannon MJ (2011) The Transcription Factor NURR1 Exerts Concentration-Dependent Effects on Target Genes Mediating Distinct Biological Processes. *Front Neurosci* **5**:135.
- Jonquieres von G, Mersmann N, Klugmann CB, Harasta AE, Lutz B, Teahan O, Housley GD, Fröhlich D, Krämer-Albers E-M, and Klugmann M (2013) Glial promoter selectivity following AAV-delivery to the immature brain. *PLoS ONE* **8**:e65646.

- Kadkhodaei B, Alvarsson A, Schintu N, Ramsköld D, Volakakis N, Joodmardi E, Yoshitake T, Kehr J, Decressac M, Björklund A, Sandberg R, Svenningsson P, and Perlmann T (2013) Transcription factor Nurr1 maintains fiber integrity and nuclear-encoded mitochondrial gene expression in dopamine neurons. *Proc Natl Acad Sci USA* **110**:2360–2365, National Acad Sciences.
- Kadkhodaei B, Ito T, Joodmardi E, Mattsson B, Rouillard C, Carta M, Muramatsu S-I, Sumi-Ichinose C, Nomura T, Metzger D, Chambon P, Lindqvist E, Larsson N-G, Olson L, Björklund A, Ichinose H, and Perlmann T (2009) Nurr1 is required for maintenance of maturing and adult midbrain dopamine neurons. *Journal of Neuroscience* **29**:15923–15932.
- Kaltschmidt B, Ndiaye D, Korte M, Pothion S, Arbibe L, Prüllage M, Pfeiffer J, Lindecke A, Staiger V, Israël A, Kaltschmidt C, and Mémet S (2006) NF-kappaB regulates spatial memory formation and synaptic plasticity through protein kinase A/CREB signaling. *Mol Cell Biol* **26**:2936–2946.
- Kaltschmidt B, Uherek M, Volk B, Baeuerle PA, and Kaltschmidt C (1997) Transcription factor NF-kappaB is activated in primary neurons by amyloid beta peptides and in neurons surrounding early plaques from patients with Alzheimer disease. *PNAS* **94**:2642–2647.
- Kassed CA, Willing AE, Garbuzova-Davis S, Sanberg PR, and Pennypacker KR (2002) Lack of NF-kappaB p50 exacerbates degeneration of hippocampal neurons after chemical exposure and impairs learning. *Experimental Neurology* **176**:277–288.
- Kim J-Y, Ash RT, Ceballos-Diaz C, Levites Y, Golde TE, Smirnakis SM, and Jankowsky JL (2013) Viral transduction of the neonatal brain delivers controllable genetic mosaicism for visualising and manipulating neuronal circuits in vivo. *European Journal of Neuroscience* **37**:1203–1220.
- Kim J-Y, Grunke SD, Levites Y, Golde TE, and Jankowsky JL (2014) Intracerebroventricular viral injection of the neonatal mouse brain for persistent and widespread neuronal transduction. *J Vis Exp* 51863.
- Kim TE, Seo JS, Yang JW, Kim MW, Kausar R, Joe E, Kim BY, and Lee MA (2013) Nurr1 Represses Tyrosine Hydroxylase Expression via SIRT1 in Human Neural Stem Cells. *PLoS ONE* **8**:e71469.
- Kirik D, Rosenblad C, Bjorklund A, and Mandel RJ (2000) Long-term rAAV-mediated gene transfer of GDNF in the rat Parkinson's model: intrastriatal but not intranigral transduction promotes functional regeneration in the lesioned nigrostriatal system. *Journal of Neuroscience* **20**:4686–4700.
- Kirkley KS, Walton KD, Duncan C, Tjalkens, RB (2017) Spontaneous development of cutaneous squamous cell carcinoma in mice with cell-specific deletion of inhibitor of κ B kinase 2. *Comparative Medicine* **67**:407-415.

- Kirkley KS, Popichak KP, Hammond SL, Davies C, Hunt, L, Tjalkens, RB (2018) Genetic Suppression of Astrocyte-IKK2/NF- κ B reduces neuroinflammation and neuronal loss in Parkinson's disease. (*under review*)
- Kirkley KS, Popichak KA, Afzali MF, Legare ME, and Tjalkens RB (2017) Microglia amplify inflammatory activation of astrocytes in manganese neurotoxicity. 1–18, *Journal of Neuroinflammation*.
- Kiyota T, Ingraham KL, Swan RJ, Jacobsen MT, Andrews SJ, and Ikezu T (2012) AAV serotype 2/1-mediated gene delivery of anti-inflammatory interleukin-10 enhances neurogenesis and cognitive function in APP+PS1 mice. *Gene Ther* **19**:724–733.
- Klein C, and Westenberger A (2012) Genetics of Parkinson's disease. *Cold Spring Harb Perspect Med* **2**:a008888.
- Klein RL, Meyer EM, Peel AL, Zolotukhin S, Meyers C, Muzyczka N, and King MA (1998) Neuron-specific transduction in the rat septohippocampal or nigrostriatal pathway by recombinant adeno-associated virus vectors. *Experimental Neurology* **150**:183–194.
- Kotterman MA, and Schaffer DV (2014) Engineering adeno-associated viruses for clinical gene therapy. *Nat Rev Genet* 1–7, Nature Publishing Group.
- Kuhn DM, Francescutti-Verbeem DM, and Thomas DM (2006) Dopamine quinones activate microglia and induce a neurotoxic gene expression profile: relationship to methamphetamine-induced nerve ending damage. *Ann N Y Acad Sci* **1074**:31–41.
- Kurkowska-Jastrzebska I, Wrońska A, Kohutnicka M, Członkowski A, and Członkowska A (1999) MHC class II positive microglia and lymphocytic infiltration are present in the substantia nigra and striatum in mouse model of Parkinson's disease. *Acta Neurobiol Exp (Wars)* **59**:1–8.
- Lai JC, Leung TK, Lim, L (1984) Differences in the neurotoxic effects of manganese during development and aging: some observations on brain regional neurotransmitter and non-neurotransmitter metabolism in a developmental rat model of chronic manganese encephalopathy. *Neurotoxicology* **5** (1): 37-47.
- Lan AP, Chen J, Chai ZF, and Hu Y (2016) The neurotoxicity of iron, copper and cobalt in Parkinson's disease through ROS-mediated mechanisms. *Biometals* **29**:665–678, Springer Netherlands.
- Langston JW, Ballard P, Tetrud JW, and Irwin I (1983) Chronic Parkinsonism in humans due to a product of meperidine-analog synthesis. *Science* **219**:979–980.
- Lawlor PA, Bland RJ, Mouravlev A, Young D, and During MJ (2009) Efficient gene delivery and selective transduction of glial cells in the mammalian brain by AAV serotypes isolated from nonhuman primates. *Mol Ther* **17**:1692–1702.

- Le W, Conneely OM, He Y, Jankovic J, and Appel SH (1999) Reduced Nurr1 expression increases the vulnerability of mesencephalic dopamine neurons to MPTP-induced injury. *J Neurochem* **73**:2218–2221.
- Lee S-O, Li X, Hedrick E, Jin U-H, Tjalkens RB, Backos DS, Li L, Zhang Y, Wu Q, and Safe S (2014) Diindolylmethane Analogs Bind NR4A1 and Are NR4A1 Antagonists in Colon Cancer Cells. *Molecular Endocrinology* **28**:1729–1739.
- Lee Y, Messing A, Su M, and Brenner M (2008) GFAP promoter elements required for region-specific and astrocyte-specific expression. *Glia* **56**:481–493.
- Lesch KP, Bengel D, Heils A, Sabol SZ, Greenberg BD, Petri S, Benjamin J, Müller CR, Hamer DH, and Murphy DL (1996) Association of anxiety-related traits with a polymorphism in the serotonin transporter gene regulatory region. *Science* **274**:1527–1531.
- Li K, Nicaise C, Sannie D, Hala TJ, Javed E, Parker JL, Putatunda R, Regan KA, Suain V, Brion J-P, Rhoderick F, Wright MC, Poulsen DJ, and Lepore AC (2014) Overexpression of the astrocyte glutamate transporter GLT1 exacerbates phrenic motor neuron degeneration, diaphragm compromise, and forelimb motor dysfunction following cervical contusion spinal cord injury. *J Neurosci* **34**:7622–7638.
- Li W, Liu J, Hammond SL, Tjalkens RB, Saifudeen Z, and Feng Y (2015) Angiotensin II regulates brain (pro)renin receptor expression through activation of cAMP response element-binding protein. *Am J Physiol Regul Integr Comp Physiol* ajpgu.00319.2014.
- Li X, Lee S-O, and Safe S (2012) Structure-dependent activation of NR4A2 (Nurr1) by 1,1-bis(3'-indolyl)-1-(aromatic)methane analogs in pancreatic cancer cells. *Biochemical Pharmacology* **83**:1445–1455.
- Lian H, Litvinchuk A, Chiang ACA, Aithmitti N, Jankowsky JL, and Zheng H (2016) Astrocyte-Microglia Cross Talk through Complement Activation Modulates Amyloid Pathology in Mouse Models of Alzheimer's Disease. *Journal of Neuroscience* **36**:577–589.
- Lian H, Yang L, Cole A, Sun L, Chiang ACA, Fowler SW, Shim DJ, Rodriguez-Rivera J, Tagliabatella G, Jankowsky JL, Lu H-C, and Zheng H (2015) NF- κ B-Activated Astroglial Release of Complement C3 Compromises Neuronal Morphology and Function Associated with Alzheimer's Disease. *Neuron* **85**:101–115, Elsevier Inc.
- Liddel SA, and Ben A Barres (2017) Reactive Astrocytes: Production, Function, and Therapeutic Potential. 1–11, Elsevier Inc.
- Liddel SA, Guttenplan KA, Clarke LE, Bennett FC, Bohlen CJ, Schirmer L, Bennett ML, Münch AE, Chung W-S, Peterson TC, Wilton DK, Frouin A, Napier BA, Panicker N, Kumar M, Buckwalter MS, Rowitch DH, Dawson VL, Dawson TM, Stevens B, and

- Barres BA (2017) Neurotoxic reactive astrocytes are induced by activated microglia. *Nature Publishing Group* **541**:481–487.
- Lipe GW, Duhart H, Newport GF, Slikker W, Ali SF, (1999) Effect of manganese on the concentration of amino acids in different regions of the rat brain. *Journal of Environmental Science and Health Biology* **34** (1):199-232.
- Liu H, Wei L, Tao Q, Deng H, Ming M, Xu P, and Le W (2012) Decreased NURR1 and PITX3 gene expression in Chinese patients with Parkinson's disease. *Eur J Neurol* **19**:870–875.
- Manfredsson F (2016) Gene Therapy for Neurological Disorders: Methods and Protocols. *Methods in Molecular Biology*, vol. 1382, DOI 10.1007/978-1-4939-3271-9_1.
- Manning-Bog AB, McCormack AL, Li J, Uversky VN, Fink AL, and Di Monte DA (2002) The herbicide paraquat causes up-regulation and aggregation of alpha-synuclein in mice: paraquat and alpha-synuclein. *J Biol Chem* **277**:1641–1644.
- Marks WJ, Bartus RT, Siffert J, Davis CS, Lozano A, Boulis N, Vitek J, Stacy M, Turner D, Verhagen L, Bakay R, Watts R, Guthrie B, Jankovic J, Simpson R, Tagliati M, Alterman R, Stern M, Baltuch G, Starr PA, Larson PS, Ostrem JL, Nutt J, Kieburtz K, Kordower JH, and Olanow CW (2010) Gene delivery of AAV2-neurturin for Parkinson's disease: a double-blind, randomised, controlled trial. *The Lancet Neurology* **9**:1164–1172.
- Marsden CD (1982) [Functions of the basal ganglia]. *Rinsho Shinkeigaku* **22**:1093–1094.
- McCown TJ, Xiao X, Li J, Breese GR, and Samulski RJ (1996) Differential and persistent expression patterns of CNS gene transfer by an adeno-associated virus (AAV) vector. *Brain Research* **713**:99–107.
- McElroy PB, Liang L-P, Day BJ, and Patel M (2017) Scavenging reactive oxygen species inhibits status epilepticus-induced neuroinflammation. *Experimental Neurology* **298**:13–22, Elsevier.
- McFarland NR, Dimant H, Kibuuka L, Ebrahimi-Fakhari D, Desjardins CA, Danzer KM, Danzer M, Fan Z, Schwarzschild MA, Hirst W, and McLean PJ (2014) Chronic Treatment with Novel Small Molecule Hsp90 Inhibitors Rescues Striatal Dopamine Levels but Not α -Synuclein-Induced Neuronal Cell Loss. *PLoS ONE* **9**:e86048–8.
- McFarland NR, Lee J-S, Hyman BT, and McLean PJ (2009) Comparison of transduction efficiency of recombinant AAV serotypes 1, 2, 5, and 8 in the rat nigrostriatal system. *J Neurochem* **109**:838–845, Blackwell Publishing Ltd.
- McGeer PL, and McGeer EG (2008) Glial reactions in Parkinson's disease. *Mov Disord* **23**:474–483.

- McLean JR, Smith GA, Rocha EM, Hayes MA, Beagan JA, Hallett PJ, and Isacson O (2014) Widespread neuron-specific transgene expression in brain and spinal cord following synapsin promoter-driven AAV9 neonatal intracerebroventricular injection. *Neuroscience Letters* **576**:73–78.
- Meng X, Yang F, Ouyang T, Liu B, Wu C, and Jiang W (2015) Specific gene expression in mouse cortical astrocytes is mediated by a 1740bp-GFAP promoter-driven combined adeno-associated virus2/5/7/8/9. 1–6, Elsevier Ireland Ltd.
- Mergler D, and Baldwin M (1997) Early manifestations of manganese neurotoxicity in humans: an update. *Environ Res* **73**:92–100.
- Merienne N, Le Douce J, Faivre E, Déglon N, and Bonvento G (2013) Efficient gene delivery and selective transduction of astrocytes in the mammalian brain using viral vectors. *Front Cell Neurosci* **7**:106.
- Mettang M, Reichel SN, Lattke M, Palmer A, Abaei A, Rasche V, Huber-Lang M, Baumann B, and Wirth T (2017) IKK2/NF- κ B signaling protects neurons after traumatic brain injury. *FASEB J* fj.201700826R.
- Miller JA, Runkle SA, Tjalkens RB, and Philbert MA (2011) 1,3-Dinitrobenzene-induced metabolic impairment through selective inactivation of the pyruvate dehydrogenase complex. *Toxicol Sci* **122**:502–511, Oxford University Press.
- Mittermeyer G, Christine CW, Rosenbluth KH, Baker SL, Starr P, Larson P, Kaplan PL, Forsayeth J, Aminoff MJ, and Bankiewicz KS (2012) Long-term evaluation of a phase 1 study of AADC gene therapy for Parkinson's disease. *Human Gene Therapy* **23**:377–381.
- Montarolo F, Perga S, Martire S, Navone DN, Marchet A, Leotta D, and Bertolotto A (2016) Altered NR4A Subfamily Gene Expression Level in Peripheral Blood of Parkinson's and Alzheimer's Disease Patients. *Neurotox Res* **30**:338–344, Springer US.
- Moreno JA, Streifel KM, Sullivan KA, Hanneman WH, and Tjalkens RB (2011) Manganese-induced NF- κ B activation and nitrosative stress is decreased by estrogen in juvenile mice. *Toxicol Sci* **122**:121–133, Oxford University Press.
- Moreno JA, Streifel KM, Sullivan KA, Legare ME, and Tjalkens RB (2009) Developmental exposure to manganese increases adult susceptibility to inflammatory activation of glia and neuronal protein nitration. *Toxicol Sci* **112**:405–415.
- Moreno JA, Yeomans EC, Streifel KM, Brattin BL, Taylor RJ, and Tjalkens RB (2009) Age-Dependent Susceptibility to Manganese-Induced Neurological Dysfunction. *Toxicological Sciences* **112**:394–404.

- Morrison HW, and Filosa JA (2013) A quantitative spatiotemporal analysis of microglia morphology during ischemic stroke and reperfusion. *Journal of Neuroinflammation* **10**:1–1, Journal of Neuroinflammation.
- Nitkiewicz J, Borjabad A, Morgello S, Murray J, Chao W, Emdad L, Fisher PB, Potash MJ, and Volsky DJ (2017) HIV induces expression of complement component C3 in astrocytes by NF- κ B-dependent activation of interleukin-6 synthesis. *Journal of Neuroinflammation* **14**:23, BioMed Central.
- Oeckl P, Lattke M, Wirth T, Baumann B, and Ferger B (2012) Astrocyte-specific IKK2 activation in mice is sufficient to induce neuroinflammation but does not increase susceptibility to MPTP. *Neurobiology of Disease* **48**:481–487.
- Oh S-M, Chang M-Y, Song J-J, Rhee Y-H, Joe E-H, Lee H-S, Yi S-H, and Lee S-H (2015) Combined Nurr1 and Foxa2 roles in the therapy of Parkinson's disease. *EMBO Molecular Medicine* **7**:510–525.
- Ordentlich P (2003) Identification of the Antineoplastic Agent 6-Mercaptopurine as an Activator of the Orphan Nuclear Hormone Receptor Nurr1. *Journal of Biological Chemistry* **278**:24791–24799.
- Pacelli C, Giguère N, Bourque M-J, Lévesque M, Slack RS, and Trudeau L-E (2015) Elevated Mitochondrial Bioenergetics and Axonal Arborization Size Are Key Contributors to the Vulnerability of Dopamine Neurons. *Curr Biol* **25**:2349–2360.
- Pardridge WM (2012) Drug transport across the blood-brain barrier. *J Cereb Blood Flow Metab* **32**:1959–1972.
- Parillaud VR, Lornet G, Monnet Y, Privat A-L, Haddad AT, Brochard V, Bekaert A, de Chanville CB, Hirsch EC, Combadière C, Hunot S, and Lobsiger CS (2017) Analysis of monocyte infiltration in MPTP mice reveals that microglial CX3CR1 protects against neurotoxic over-induction of monocyte-attracting CCL2 by astrocytes. *Journal of Neuroinflammation* **14**:60, BioMed Central.
- Parkinson, J (1817) An Essay on the Shaking Palsy. *Whittingham and Rowland*.
- Passini MA, and Wolfe JH (2001) Widespread gene delivery and structure-specific patterns of expression in the brain after intraventricular injections of neonatal mice with an adeno-associated virus vector. *Journal of Virology* **75**:12382–12392.
- Passini MA, Watson DJ, Vite CH, Landsburg DJ, Feigenbaum AL, and Wolfe JH (2003) Intraventricular Brain Injection of Adeno-Associated Virus Type 1 (AAV1) in Neonatal Mice Results in Complementary Patterns of Neuronal Transduction to AAV2 and Total Long-Term Correction of Storage Lesions in the Brains of α -Glucuronidase-Deficient Mice. *Journal of Virology* **77**:7034–7040.
- Patel M (2016) Targeting Oxidative Stress in Central Nervous System Disorders. *Trends Pharmacol Sci* **37**:768–778.

- Peres TV, Schettinger MRC, Chen P, Carvalho F, Avila DS, Bowman AB, and Aschner M (2016) "Manganese-induced neurotoxicity: a review of its behavioral consequences and neuroprotective strategies." *BMC Pharmacology and Toxicology* 1–20, BMC Pharmacology and Toxicology.
- Pillay S, Meyer NL, Puschnik AS, Davulcu O, Diep J, Ishikawa Y, Jae LT, Wosen JE, Nagamine CM, Chapman MS, and Carette JE (2016) An essential receptor for adeno-associated virus infection. *Nature Publishing Group* **530**:108–112.
- Polunas M, Halladay A, Tjalkens RB, Philbert MA, Lowndes H, and Reuhl K (2011) Role of oxidative stress and the mitochondrial permeability transition in methylmercury cytotoxicity. *Neurotoxicology* **32**:526–534.
- Price A, Manzoni C, Cookson MR, and Lewis PA (2018) The LRRK2 signalling system. *Cell Tissue Res* **72**:58–12, Springer Berlin Heidelberg.
- Racette BA, Searles Nielsen S, Criswell SR, Sheppard L, Seixas N, Warden MN, and Checkoway H (2017) Dose-dependent progression of parkinsonism in manganese-exposed welders. *Neurology* **88**:344–351.
- Ramsay RR, Krueger MJ, Youngster SK, and Singer TP (1991) Evidence that the inhibition sites of the neurotoxic amine 1-methyl-4-phenylpyridinium (MPP+) and of the respiratory chain inhibitor piericidin A are the same. *Biochem J* **273(Pt 2)**:481–484, Portland Press Ltd.
- Ramsey CP, and Tansey MG (2014) A survey from 2012 of evidence for the role of neuroinflammation in neurotoxin animal models of Parkinson's disease and potential molecular targets. *Experimental Neurology* **256**:126–132.
- Ricklin D, Reis ES, Mastellos DC, Gros P, and Lambris JD (2016) Complement component C3 - The "Swiss Army Knife" of innate immunity and host defense. *Immunol Rev* **274**:33–58.
- RODIER J (1955) Manganese poisoning in Moroccan miners. *Br J Ind Med* **12**:21–35, BMJ Publishing Group.
- Romano G, Suon S, Jin H, Donaldson AE, and Iacovitti L (2005) Characterization of five evolutionary conserved regions of the human tyrosine hydroxylase (TH) promoter: implications for the engineering of a human TH minimal promoter assembled in a self-inactivating lentiviral vector system. *J Cell Physiol* **204**:666–677.
- Royo NC, Vandenberghe LH, Ma J-Y, Hauspurg A, Yu L, Maronski M, Johnston J, Dichter MA, Wilson JM, and Watson DJ (2008) Specific AAV serotypes stably transduce primary hippocampal and cortical cultures with high efficiency and low toxicity. *Brain Research* **1190**:15–22.
- Rugless F, Bhattacharya A, Succop P, Dietrich KN, Cox C, Alden J, Kuhnell P, Barnas M, Wright R, Parsons PJ, Praamsma ML, Palmer CD, Beidler C, Wittberg R, and

- Haynes EN (2014) Childhood exposure to manganese and postural instability in children living near a ferromanganese refinery in Southeastern Ohio. *Neurotoxicol Teratol* **41**:71–79.
- Sacchetti P, Brownschidle LA, Granneman JG, and Bannon MJ (1999) Characterization of the 5'-flanking region of the human dopamine transporter gene. *Brain Res Mol Brain Res* **74**:167–174.
- Sadasivan S, Sharp B, Schultz-Cherry S, and Smeyne RJ (2017) Synergistic effects of influenza and 1-methyl-4-phenyl-1,2,3,6-tetrahydropyridine (MPTP) can be eliminated by the use of influenza therapeutics: experimental evidence for the multi-hit hypothesis. *npj Parkinson's Disease* 1–2, Springer US.
- Safe S, Jin U-H, Morpurgo B, Abudayyeh A, Singh M, and Tjalkens RB (2015) Nuclear receptor 4A (NR4A) family - orphans no more. *J Steroid Biochem Mol Biol*, doi: 10.1016/j.jsbmb.2015.04.016.
- Safe S, Papineni S, and Chintharlapalli S (2008) Cancer chemotherapy with indole-3-carbinol, bis(3'-indolyl)methane and synthetic analogs. *Cancer Lett* **269**:326–338.
- Saijo K, Winner B, Carson CT, Collier JG, Boyer L, Rosenfeld MG, Gage FH, and Glass CK (2009) A Nurr1/CoREST pathway in microglia and astrocytes protects dopaminergic neurons from inflammation-induced death. *Cell* **137**:47–59.
- Sakurada K, Ohshima-Sakurada M, Palmer TD, and Gage FH (1999) Nurr1, an orphan nuclear receptor, is a transcriptional activator of endogenous tyrosine hydroxylase in neural progenitor cells derived from the adult brain. *Development* **126**:4017–4026.
- Samulski RJ, Berns KI, Tan M, and Muzyczka N (1982) Cloning of adeno-associated virus into pBR322: rescue of intact virus from the recombinant plasmid in human cells. *PNAS* **79**:2077–2081, National Academy of Sciences.
- Saucedo-Cardenas O, Quintana-Hau JD, Le WD, Smidt MP, Cox JJ, De Mayo F, Burbach JP, and Conneely OM (1998) Nurr1 is essential for the induction of the dopaminergic phenotype and the survival of ventral mesencephalic late dopaminergic precursor neurons. *PNAS* **95**:4013–4018, National Acad Sciences.
- Schartz ND, Wyatt-Johnson SK, Price LR, Colin SA, and Brewster AL (2018a) Status epilepticus triggers long-lasting activation of complement C1q-C3 signaling in the hippocampus that correlates with seizure frequency in experimental epilepsy. *Neurobiology of Disease* **109**:163–173, Elsevier.
- Schartz ND, Wyatt-Johnson SK, Price LR, Colin SA, and Brewster AL (2018b) Status epilepticus triggers long-lasting activation of complement C1q-C3 signaling in the hippocampus that correlates with seizure frequency in experimental epilepsy. *Neurobiology of Disease* **109**:163–173.

- Schneider CA, Rasband WS, and Eliceiri KW (2012) NIH Image to ImageJ: 25 years of image analysis. *Nat Methods* **9**:671–675.
- Shastri BS (2001) Parkinson disease: etiology, pathogenesis and future of gene therapy. *Neurosci Res* **41**:5–12.
- Sherer TB, Kim J-H, Betarbet R, and Greenamyre JT (2003) Subcutaneous rotenone exposure causes highly selective dopaminergic degeneration and alpha-synuclein aggregation. *Experimental Neurology* **179**:9–16.
- Sidoryk-Wegrzynowicz M, and Aschner M (2013) Role of astrocytes in manganese mediated neurotoxicity. *BMC Pharmacology and Toxicology* **14**:23, BioMed Central.
- Simon P, Dupuis R, and Costentin J (1994) Thigmotaxis as an index of anxiety in mice. Influence of dopaminergic transmissions. *Behavioural Brain Research* **61**:59–64.
- Smith GA, Rocha EM, Rooney T, Barneoud P, McLean JR, Beagan J, Osborn T, Coimbra M, Luo Y, Hallett PJ, and Isacson O (2015) A Nurr1 Agonist Causes Neuroprotection in a Parkinson's Disease Lesion Model Primed with the Toll-Like Receptor 3 dsRNA Inflammatory Stimulant Poly(I:C). *PLoS ONE* **10**:e0121072.
- Smits SM, Ponnio T, Conneely OM, Burbach JPH, and Smidt MP (2003) Involvement of Nurr1 in specifying the neurotransmitter identity of ventral midbrain dopaminergic neurons. *European Journal of Neuroscience* **18**:1731–1738, Blackwell Science, Ltd.
- Surmeier DJ, Halliday GM, and Simuni T (2017) Calcium, mitochondrial dysfunction and slowing the progression of Parkinson's disease. *Experimental Neurology* **298**:202–209.
- Takser L, Mergler D, Hellier G, Sahuquillo J, and Huel G (2003) Manganese, monoamine metabolite levels at birth, and child psychomotor development. *Neurotoxicology* **24**:667–674.
- Tjalkens RB, Liu X, Mohl B, Wright T, Moreno JA, Carbone DL, and Safe S (2008) The peroxisome proliferator-activated receptor-gamma agonist 1,1-bis(3'-indolyl)-1-(p-trifluoromethylphenyl)methane suppresses manganese-induced production of nitric oxide in astrocytes and inhibits apoptosis in cocultured PC12 cells. *J Neurosci Res* **86**:618–629.
- Tomer R, Ye L, Hsueh B, and Deisseroth K (2014) Advanced CLARITY for rapid and high-resolution imaging of intact tissues. *Nat Protoc* **9**:1682–1697.
- Uversky VN, Li J, and Fink AL (2001) Pesticides directly accelerate the rate of alpha-synuclein fibril formation: a possible factor in Parkinson's disease. *FEBS Letters* **500**:105–108.

- Vagner T, Dvorzhak A, Wójtowicz AM, Harms C, and Grantyn R (2016) Systemic application of AAV vectors targeting GFAP-expressing astrocytes in Z-Q175-K1 Huntington's disease mice. *Mol Cell Neurosci* **77**:76–86.
- van Loo G, De Lorenzi R, Schmidt H, Huth M, Mildner A, Schmidt-Supprian M, Lassmann H, Prinz MR, and Pasparakis M (2006) Inhibition of transcription factor NF-kappaB in the central nervous system ameliorates autoimmune encephalomyelitis in mice. *Nat Immunol* **7**:954–961.
- Volakakis N, Malewicz M, Kadkhodai B, Perlmann T, and Benoit G (2006) Characterization of the Nurr1 ligand-binding domain co-activator interaction surface. *Journal of Molecular Endocrinology* **37**:317–326.
- Wang JD, Huang CC, Hwang YH, Chiang JR, Lin JM, and Chen JS (1989) Manganese induced parkinsonism: an outbreak due to an unrepaired ventilation control system in a ferromanganese smelter. *Br J Ind Med* **46**:856–859, BMJ Publishing Group.
- Wang XH, Lu G, Hu X, Tsang KS, Kwong WH, Wu FX, Meng HW, Jiang S, Liu SW, Ng HK, and Poon WS (2012) Quantitative assessment of gait and neurochemical correlation in a classical murine model of Parkinson's disease. *BMC Neurosci* **13**:142.
- Wang Z, Benoit G, Liu J, Prasad S, Aarnisalo P, Liu X, Xu H, Walker NPC, and Perlmann T (2003) Structure and function of Nurr1 identifies a class of ligand-independent nuclear receptors. *Nature* **423**:555–560.
- Wanner IB, Anderson MA, Song B, Levine J, Fernandez A, Gray-Thompson Z, Ao Y, and Sofroniew MV (2013) Glial scar borders are formed by newly proliferated, elongated astrocytes that interact to corral inflammatory and fibrotic cells via STAT3-dependent mechanisms after spinal cord injury. *J Neurosci* **33**:12870–12886, Society for Neuroscience.
- Witholt R, Gwiazda RH, and Smith DR (2000) The neurobehavioral effects of subchronic manganese exposure in the presence and absence of pre-parkinsonism. *Neurotoxicol Teratol* **22**:851–861.
- Wu D-C, Teismann P, Tieu K, Vila M, Jackson-Lewis V, Ischiropoulos H, and Przedborski S (2003) NADPH oxidase mediates oxidative stress in the 1-methyl-4-phenyl-1,2,3,6-tetrahydropyridine model of Parkinson's disease. *PNAS* **100**:6145–6150, National Acad Sciences.
- Zetterström RH, Solomin L, Jansson L, Hoffer BJ, Olson L, and Perlmann T (1997) Dopamine neuron agenesis in Nurr1-deficient mice. *Science* **276**:248–250.
- Zetterström RH, Williams R, Perlmann T, and Olson L (1996) Cellular expression of the immediate early transcription factors Nurr1 and NGFI-B suggests a gene regulatory role in several brain regions including the nigrostriatal dopamine system. *Molecular Brain Research* **41**:111–120.

- Zhan X, Stamova B, Jin L-W, DeCarli C, Phinney B, and Sharp FR (2016) Gram-negative bacterial molecules associate with Alzheimer disease pathology. *Neurology* **87**:2324–2332.
- Zhou W, Bercury K, Cumiskey J, Luong N, Lebin J, and Freed CR (2011) Phenylbutyrate up-regulates the DJ-1 protein and protects neurons in cell culture and in animal models of Parkinson disease. *Journal of Biological Chemistry* **286**:14941–14951.
- Zhou W, Milder JB, and Freed CR (2008) Transgenic mice overexpressing tyrosine-to-cysteine mutant human alpha-synuclein: a progressive neurodegenerative model of diffuse Lewy body disease. *J Biol Chem* **283**:9863–9870.
- Zhu W, Xie W, Pan T, Xu P, Fridkin M, Zheng H, Jankovic J, Youdim MBH, and Le W (2007) Prevention and restoration of lactacystin-induced nigrostriatal dopamine neuron degeneration by novel brain-permeable iron chelators. *FASEB J* **21**:3835–3844, Federation of American Societies for Experimental Biology.
- Zidenburg-Cherr S, Keen CL, Lonnerdal B, Hurley LS (1983) Superoxide dismutase and lipid peroxidation in the rat: developmental correlations affected by manganese deficiency. *Journal of Nutrition* **113** (2): 2498-2502.